Study of Novel Techniques for Verification Imaging and Patient Dose Reconstruction in External Beam Radiation Therapy

Geneviève Jarry

Doctor of Philosophy

Department of Physics

McGill University

Montreal, Quebec

2007-03-29

A thesis submitted to the faculty of graduate studies and research in partial fulfillment of the requirements of the degree of Doctor of Philosophy

Your file Votre référence
ISBN: 978-0-494-32300-7
Our file Notre référence
ISBN: 978-0-494-32300-7

DEDICATION

To the people I love: Suzel, Aldé, Marjolaine and David

ACKNOWLEDGEMENTS

As I reread my thesis for the thousandth time I ponder on all of you who have guided and helped me in the last four years.

First I wish to thank my supervisor, Dr. Frank Verhaegen, for his guidance. While supervising me, he gave me the freedom to work independently and to explore my own research interests. He gave me the opportunity to participate to various international meetings and in the process I had the chance to expand my horizons, both professionally and culturally. I would also like to thank him for thoroughly reviewing this thesis; his comments and suggestions greatly improved the quality of my work.

My appreciation goes to Dr. Jan Seuntjens who played the role of my supervisor for the first three months of my Ph.D. From that time forward, he was always there to listen to me, to discuss my project and to help me.

During my thesis I had the chance to collaborate with a team of researchers at the Princess Margaret Hospital in Toronto. I would like to thank Dr. David Jaffray for giving me this opportunity, Dr. Douglas Moseley for making me feel welcome and helping me with measurements, Dr. Jeffrey Siewerdsen for always being the first to answer my e-mails and for sharing his expertise on CBCT with me, and Sean Graham for helping me with the measurements.

I also have to thank the medical physicists working at the MGH who have taught me about clinical work. I would like to thank Dr. Slobodan Devic for answering my many questions on electron beam treatments and portal imagers, William Parker for

introducing me to Cadplan, Michael Evans for helping me with electron beam measurements, Russel Ruo for helping me with Corvus and IMRT treatment planning and Dr. Wamied Abdel-Rahman for maintaining the computer cluster. I would like to acknowledge the engineering team: Pierre Leger who helped me with understanding better the portal imager and Joe Larkins who helped me with my computer more than once. I would like to acknowledge the amazing work of the technologists working at the CL21A and CL21B who have helped me throughout my different projects. My appreciation goes to Dr. Ervin Pogdorsak for maintaining the excellence of the Medical Physics program at McGill University.

I would like to thank all of the students that have gone through the program in the last four years and with whom I have shared my joys and frustrations. More particularly I would like to thank Gabriella, Danielle, Clarisse, Claude, Vicky, Matthieu, Caroline, Sara, Rumtin, Andrew, Magdalena, Charmaine, Kristin, and Arman for being not only colleagues but friends. I would like to thank Lalith who introduced me to the portal imager, Vicky who helped me with the electron beam modeling, Danielle who helped me with IMRT measurements, Matthieu who helped me with the kV unit modeling and Emily H. who spent a lot of time making sure the MC cluster worked. A special mention goes to Gabriella who had the patience to listen to me when my research was not going as well as I would have wished. She was always happy to help me with measurements with the CT scanner or with debugging a program.

I would like to thank my mom and my dad who have always believed in me. I would like to thank my mom for making me believe that I can do anything I set my

mind to, for spending hours helping me with my homeworks when I was growing up and, in the process, transferring her love for learning and teaching onto me. I would like to thank my dad for supporting me in doing what I like and showing me the importance of being professional in all aspects of my life. Thank you to my little sister Marjolaine, who is also my best friend, for being my biggest fan and making me laugh when everything was going wrong. I have to thank David not only for his love, his understanding and his patience but also for his concrete contribution to my work. I have to thank him for the time he took to read my papers, to listen to my presentations and to help me with computer and programming problems. I don't believe my work would have been the same without him in my life.

Finally I acknowledge the different sources of funding I have received throughout my Ph.D. studies. The Ministère de la Santé et des Services Sociaux du Québec for the Bourse en Physique Médicale. The Fonds de la Recherche en Santé du Québec for a doctoral training award. McGill University for two Alma Matter travel grants and the National Cancer Institute of Canada for a travel grant.

ABSTRACT

Treatment delivery verification is an essential step of radiotherapy. The purpose of this thesis is to develop new methods to improve the verification of photon and electron beam radiotherapy treatments. This is achieved through developing and testing (1) a way to acquire portal images during electron beam treatments, (2) a method to reconstruct the dose delivered to patients during photon beam treatments and (3) a technique to improve image quality in kilovoltage (kV) cone beam computed tomography (CBCT) by correcting for scattered radiation. The portal images were acquired using the Varian CL21EX linac and the Varian aS500 electronic portal imaging device (EPID). The EGSnrc code was used to model fully the CL21EX, the aS500 and the kV CBCT system.

We demonstrate that portal images of electron beam treatments with adequate contrast and resolution can be produced using the bremsstrahlung photons portion of the electron beam. Monte Carlo (MC) calculations were used to characterize the bremsstrahlung photons and to obtain predicted images of various phantoms. The technique was applied on a head and neck patient.

An algorithm to reconstruct the dose given to patients during photon beam radiotherapy was developed and validated. The algorithm uses portal images and MC simulations. The primary fluence at the detector is back-projected through the patient CT geometry to obtain a reconstructed phase space file. The reconstructed phase space file is used to calculate the reconstructed dose to the patient using MC simulations. The reconstruction method was validated in homogeneous and

heterogeneous phantoms for conventional and IMRT fields.

The scattered radiation present in kV CBCT images was evaluated using MC simulations. Simulated predictions of the scatter distribution were subtracted from CBCT projection images prior to the reconstruction to improve the reconstructed image quality. Reducing the scattered radiation was found to improve contrast and reduce shading artifacts.

MC simulations, in combination with experimental techniques, have been shown to be valuable tools in the development of treatment verification methods. The three novel methods presented in this thesis contribute to the improvement of radiotherapy treatment verification. They can potentially improve treatment outcome by ensuring a better target coverage.

ABRÉGÉ

Dans cette étude, trois nouvelles façons d'améliorer la vérification des traitements de radiothérapie sont développées et testées: (1) l'acquisition d'images portales durant les traitements utilisant des faisceaux d'électrons, (2) la reconstruction de la dose administrée aux patients durant les traitements utilisant des faisceaux de photons et (3) l'amélioriation de la qualité des images du système kilovolt de tomographie à faisceau conique (kVTFC). Les images portales sont obtenues en utilisant l'accélérateur linéaire CL21EX et l'imageur portal aS500 de Varian. Les simulations de Monte Carlo (MC) sont faites à l'aide du code EGSnrc.

Nous démontrons que des images portales avec un contraste satisfaisant peuvent être obtenues durant les traitements avec faisceaux d'électrons en employant les photons de rayonnement par freinage. Des calculs de MC sont employés pour caractériser les photons de rayonnement par freinage et pour obtenir des images de divers fantômes.

Une image portale est utilisée pour déterminer la dose reçue par les patients. La distribution des particules primaires au niveau du détecteur est utilisée pour transporter les particules à travers le modèle CT du patient et pour obtenir un fichier de phase reconstruit. Ce ficher est utilisé pour calculer la dose reçue par le patient à l'aide d'un code de MC. Le programme est validé en utilisant différents fantômes pour des champs conventionnels et d'intensité modulée.

La qualité des images kVTFC est améliorée en réduisant le rayonnement diffusé. Le rayonnement diffusé dans des images projetées du système kVTFC est évalué et

soustrait des images mesurées en employant des simulations de MC. Suite à la correction, une réduction des artéfacts et une amélioration du contraste sont observées.

L'utilisation des simulations de MC et de méthodes expérimentales s'est avérée utile dans le développement des techniques de vérification de traitements. Les nouvelles méthodes présentées dans cette thèse contribuent à améliorer la qualité des traitements de radiothérapie en assurant une distribution de dose conforme au plan.

TABLE OF CONTENTS

LIST OF TABLES

LIST OF FIGURES

STATEMENT OF ORIGINALITY

To the best of my knowledge the new methods and results presented in this thesis have not been previously published by other research teams. The thesis covers three aspects of treatment verification of external radiotherapy treatment. Monte Carlo (MC) simulations are used throughout the thesis to improve and validate the verification techniques, or to understand better the physical concepts behind them. Treatment verification has been a topic of interest in the last few years and many investigators have put efforts in developing and improving the verification of radiotherapy treatments. MC simulations have also been the subject of many papers. However using MC simulations to improve treatment verification is a relatively new idea.

Very little research has been done to implement treatment verification in electron beam radiotherapy. The idea of using the bremsstrahlung part of electron beam to produce portal images had already been mentioned in the literature but had not been tested thoroughly. We are the first to use MC simulations to understand better the image formation from bremsstrahlung contamination photons and to obtain predicted portal images of electron beam treatments. No previous study quantified the image quality obtained when using portal imaging with electron beams.

Investigators have used various techniques to reconstruct the dose from portal images; however, most of these techniques are based on treatment planning dose

calculation algorithms and work best on homogeneous phantoms. No previously published studies have used MC simulations to obtain the primary fluence at the detector or to reconstruct the dose to patients from portal images acquired during beam delivery. In addition, to our knowledge, we are the first to combine comparison of original and reconstructed portal images and in-vivo dosimetry in the same dose verification algorithm.

Scatter correction in cone beam computed tomography and in projection radiography has been the subject of many studies. We have examined in great detail the scatter spatial distribution for different parameters using MC simulations for different geometry. This is something that few investigators have done. Moreover we have developed a new method to correct for scattered radiation in CBCT images and have shown that this method can be applied clinically by making use of techniques to speed up the calculations.

CONTRIBUTION OF AUTHORS

In this manuscript, we present four papers which describe various techniques to improve treatment verification of external beam radiotherapy. I was responsible for the writing of the four papers.

The first paper deals with introducing portal imaging for electron beam treatments. The idea of using the bremsstrahlung part of the electron beam to produce portal images had already been introduced in the literature but had not been tested thoroughly. In this study, I acquired the measured portal images and performed the image quality tests. The image analysis was performed using various matlab programs that I wrote. I was responsible for developing and validating the Monte Carlo (MC) models of the linac and the portal imager. I coded the modifications to the DOSXYZnrc program to obtain a phase space file after a voxelized geometry. I analyzed the MC simulations to characterize the bremsstrahlung production in the linac head. Dr. Verhaegen supervised the work; he gave useful advices on how to improve the MC simulations and he suggested some characteristics of the bremsstrahlung production that should be studied. He thoroughly reviewed the manuscript which greatly improved the paper.

The second paper describes and validates a dose reconstruction algorithm. The idea of using MC simulations to reconstruct the dose to the patient from the portal image came from a series of discussion between Dr. Verhaegen and me. I developed

the dose reconstruction algorithm and coded the program in the C language. I built and validated the MC models (linac, phantoms, EPID) involved in this study. I investigated different ways of doing the particle transport, the back projection, and the dose scoring. I elaborated the method to obtain primary fluence from the portal image using MC simulations. I introduced the idea of using a comparison of reconstructed and original portal image to verify patient and organ motion. I developed and performed various tests involving MC simulations and measurements to validate the reconstruction algorithm. Dr. Verhaegen offered his expertise for some aspects of the dose reconstruction such as the particle transport and the dose scoring. He proposed to use an analytical program to replace the full MC model of the portal imager. He also suggested tests to validate the algorithm. His insightful comments and suggestions on the manuscript greatly improved the quality of the paper.

The third and fourth papers were written in collaboration with a team at the Princess Margaret Hospital. The original idea of using MC simulations to correct for scattered radiation was born from a discussion between Dr. Verhaegen and Dr. Jaffray. The third paper was mostly concerned about characterizing the scattered radiation and developing the scatter correction technique. I developed and validated the MC model for the cone beam computed tomography (CBCT) bench top. I ran and analyzed all the simulations that were used to characterize the scatter. I also elaborated the technique for the correction of scattered radiation and tested it on different phantoms to establish its effect on contrast and artifacts. Sean Graham and Dr. Moseley helped me in acquiring images with the CBCT bench top. Dr.

Moseley wrote the back projection algorithm to obtain 3D images from the CBCT projections. The CBCT bench top was developed by Dr. Jaffray and Dr. Siewerdsen. Dr. Siewerdsen is an expert in scattered radiation for diagnostic x-rays and offered his expertise to understand better the data that was obtained with the MC simulations. Dr. Verhaegen gave useful advice on how to model an x-ray unit. He suggested using an analytical program to produce the detector image to reduce the simulation time. Dr. Verhaegen, Dr. Jaffray and Dr. Siewerdsen read the manuscript thoroughly and gave many suggestions that greatly improved the paper.

The fourth paper describes techniques that were implemented to render the MC simulations usable in a clinical set-up. I developed the different simplifications and introduced them in the MC models to make the simulations run faster. I tested the different techniques and evaluated them. Dr. Moseley and Sean Graham helped with the measurements. Dr. Jaffray provided the CBCT bench top and his expertise on CBCT. Dr. Verhaegen supervised the work and gave useful advices on the MC simulations. He thoroughly reviewed the paper.

CHAPTER 1
Introduction

1.1 Radiotherapy and its Challenges

According to the National Cancer Institute of Canada, approximately 150 thousand Canadians are diagnosed with cancer every year [1]. Half of those patients will receive radiotherapy [2], which will be used as the only treatment procedure or in conjunction with chemotherapy and/or surgery. Radiotherapy can be applied in the form of external radiotherapy where the dose is delivered by an external source of radiation or in the form of brachytherapy where the radiation source is inserted inside the patient. In the case of external radiotherapy different types of particles are used: photons in the kilovoltage (kV) or megavoltage (MV) energy ranges, electrons, neutrons, protons, or other ions. For most tumor types, the radiation dose is designed to conform to the three-dimensional (3D) shape of the tumor to minimize radiation exposure to surrounding healthy tissues. In external photon therapy, this is achieved using techniques involving complex fields and dose shaping. One of these techniques is intensity modulated radiation therapy (IMRT) in which a multi-leaf collimator (MLC) is used to vary the shape and the intensity of the radiation beam to allow a perfect mapping of the dose to the tumor [3–6].

The recent improvements in dose delivery have rendered it possible to paint the dose exactly to the tumor volume [3, 7]. Improvements in computation techniques, such as Monte Carlo (MC) simulations, have made it possible to compute accurately

the dose given to the tumor and the surrounding organs. Treatment planning software based on MC simulation transport particles through a voxelized representation of the patient and compute the dose in each voxel by recording the energy that is locally deposited by the electrons. MC calculations are widely accepted as being the most accurate way to predict the dose delivered to a patient [8, 9].

The limitations of radiotherapy are now in determining the exact tumor volume and in verifying that the dose has been delivered correctly. The conformity of the treatments makes dose verification essential as improper dose delivery can potentially compromise clinical results by insufficient dose coverage of the target volume and/or over dosage to healthy tissues [10–12]. Experimental and clinical evidence shows that changes in dose of 7% to 15% can either reduce local tumor control significantly or increase the rate of normal tissue complication [13]. Recommendations by the International Commission on Radiation Units and Measurements (ICRU) state that the accuracy in dose delivery be within 5%. Such an accuracy can be achieved only if field placement is precise during the entire course of the radiation treatment [14, 15].

Patient treatment verification consists of two parts; it includes patient positioning verification and dose delivery verification. Patient positioning verification is essential as patient movement is one of the main contributors to discrepancies between the planned and delivered treatment dose. Patient movement can happen between treatment fractions (interfraction) and during the actual treatment delivery (intrafraction). The interfraction movement can be caused, for example, by an improper alignment of the patient, change in bladder and rectal filling or weight gain or loss. The intrafraction motion is mostly due to patient breathing, cardiac

motion and digestion. Intrafraction and interfraction motion can be minimized by using strict protocols regarding bladder and rectal filling or by using gated breathing techniques [12]. However, patient movement is unavoidable.

Dose verification is also necessary as errors can be introduced at the treatment delivery stage by entering improper treatment machine settings or by wrongly setting-up the beam modifiers. Other factors may contribute to dose discrepancies in the case of a complex treatment modality such as IMRT. During IMRT treatment, there is a potential for systematic errors in the transfer of MLC leaf sequence files from the treatment planning computer to the record and verify system, and in the mechanical accuracy of the MLC leaf movements during the beam delivery [16–18].

1.2 Patient Positioning Verification of External Radiotherapy

Presently treatment verification mostly focuses on ensuring proper patient positioning. An imaging system for guidance has several requirements. Jaffray and Siewerdsen [19] list some of these requirements: it must 1) provide good soft tissue contrast, 2) have high spatial resolution and low geometric distortion for precise localization of soft tissue boundaries, 3) be able to operate within the environment of a radiation treatment machine, 4) have a large field-of-view (FOV), 5) have a short image acquisition time, and 6) impose negligible harm to the patient.

The conventional patient positioning verification technique is to use portal film or an electronic portal imaging device (EPID). An MV x-ray image of the patient is acquired on a weekly basis and this image is compared to a digitally reconstructed radiograph obtained from the treatment planning computed tomography (CT) scan.

Bony anatomy or implanted markers are used as control points to verify field alignment. Figure 1–1 shows the typical set-up for a portal image acquisition and a typical portal image. Portal images are usually acquired using a double exposure technique where an open field is acquired followed by the collimated field (in figure 1–1(b), the collimated field is delineated). The portal images are usually acquired for a total of 4 monitor units (MU) in the case of electronic portal imaging and 12 MU in the case of film [20]. An MU corresponds to the delivery of 1 cGy in the center of a (10×10) cm^2 field at the isocenter at the depth of maximum dose. Portal imaging is fast and does not contribute significantly to the patient dose. The total dose delivered over the whole treatment can vary from 17 cGy to 46 cGy depending on the imaged site [21]. MV imaging exhibits poor image quality which is due to poor contrast because of the predominance of Compton scatter over photoelectric interactions at MV energies, to scattered electrons, and to lack of details because of the large focal-spot size and poor detection efficiency of the detector [22].

Recently a lot of interest has been raised in the domain of patient positioning and treatment verification; many new techniques to verify patient positioning have been investigated. Ultrasound scans offer better soft tissue contrast than MV x-rays and have no significant biological effect on the patient. An ultrasound scan is taken before each treatment and is compared to the planning CT scan or to an ultrasound taken during the planning CT scan [23, 24]. The comparison indicates if motion has occurred and the patient can be repositioned accordingly. Currently, ultrasound images cannot be used directly for treatment planning; it needs to be matched with the CT or MRI planning data.

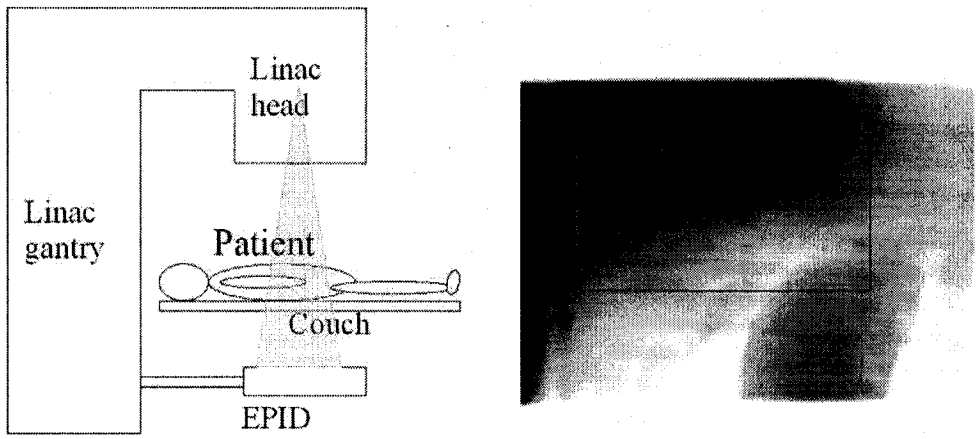

(a) (b)

Figure 1–1: (a) Schematic of a typical set-up for portal image acquisition using an EPID, and (b) open field portal image of a clavicle with delineated collimated field.

A research group in the Netherlands [25] is investigating the possibility of incorporating a magnetic resonance imaging (MRI) scanner in the linear accelerator (linac) room. MRI scans produce good soft tissue contrast but integrating such a scanner into a linac room poses many technical problems due to the strong magnetic field they generate.

CT scanners have also been integrated into linac rooms [26]. A CT scan of the patient can be taken before the treatment and can then be compared to the planning CT. This has many advantages as CT offers good soft tissue contrast and comparing images obtained with the same modality may be simpler. However, CT scanners are bulky.

One promising new technology is the cone beam CT (CBCT) scanner in which 2-dimensional (2D) projections are used to reconstruct a 3D image of the patient. CBCT scanners can either use the linac beam and the portal imager [27, 28] or a

kV x-ray unit and a dedicated kV x-ray detector [19] that are attached to the linac gantry to produce the projection images (figure 1–2). CBCT reconstructions can be compared to the planning CT or eventually be used to do treatment planning. An additional advantage is that they allow radiographic/fluoroscopic imaging throughout the treatment, an aspect that may be valuable for sites in which the potential for intrafraction motion is significant.

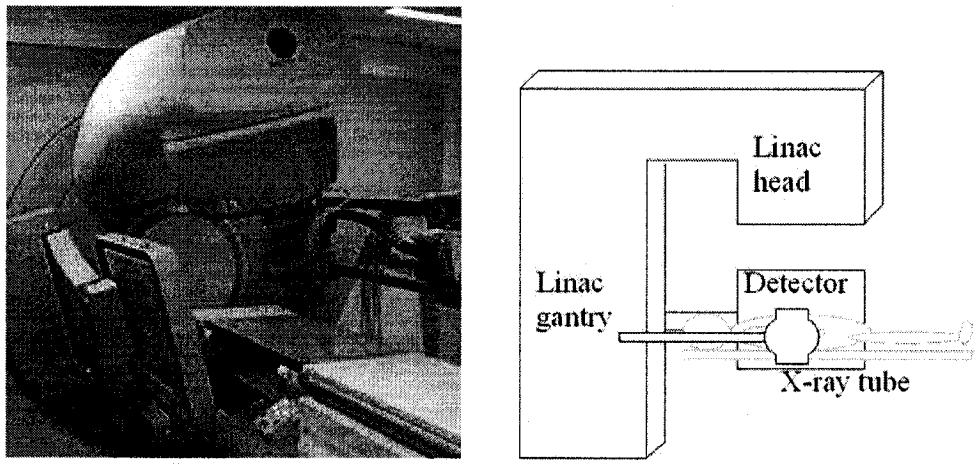

(a) (b)

Figure 1–2: (a) Picture of a commercial Synergy, Elekta kV CBCT system, showing the detector at the left and part of the x-ray tube at the right, and (b) schematic of a typical kV CBCT set-up.

1.3 Dosimetric Verification of External Radiotherapy

In order to ensure that the proper dose is delivered to the patients there is a sequence of pre-treatment verification procedures which includes dose calculation using treatment planning software, treatment machine calibration and patient set-up. Errors in each step contribute to the uncertainty in the absorbed dose delivered to the patient. The ultimate check of the actual dose delivered to a patient must

be performed at the patient level during the actual treatment delivery. Dosimetric treatment verification is not a routine procedure for most treatment types although it is recommended by various national and international organizations (AAPM [29], ICRU [30], NACP [31]). When patient dose verification is performed traditional techniques include exit or entrance patient dose measurements with thermoluminescent dosimeters (TLDs), diodes, or MOSFETs. The absorbed dose measurements involved are labor intensive, require extensive calibration and yield a minimum of information. The dose is in most cases limited to a single point [32].

In the last few years, EPIDs have been considered as good candidates for dosimetric verification. An extensive literature review of the research conducted on that topic will be presented in chapter 2.

1.4 Proposed Work

Although a lot of effort has been put into dose delivery and positioning verification for external photon beam treatments there is still a considerable amount of work to be done. Advancements in technology such as photon IMRT and electron modulated radiotherapy allow very conformal doses to the tumor and can improve the treatment outcome. However, day-to-day dose verification becomes even more important not only because small patient/organ movements can now have a significant impact on the dose distribution but also because mechanical failures are more likely to occur. Day-to-day verification of external photon radiotherapy is not yet the norm and is non existent in the case of electron beam radiotherapy. A considerable amount of work needs to be done to develop daily dose verification tools and to improve the quality of the verification images.

In this thesis, we will explore different aspects of treatment verification in external beam radiation therapy. Two treatment verification modalities are considered the amorphous silicon (aSi) EPID and the kV CBCT. MC tools are used throughout the thesis for the development and the validation of new techniques for treatment verification and for image quality improvements.

The thesis consists of four manuscripts that have been either published or submitted to journals. Chapter 2 presents a comprehensive review of the literature including portal imaging dosimetry for external photon and electron beams, CBCT technology and MC modeling. Chapters 3 and 4, respectively, provide additional information on the MC models that were developed for this thesis and on the dosimetric properties of the EPID we used. This information was not included in the manuscripts due to their concise nature.

In chapter 5 we present a paper published in *Physics in Medicine and Biology.* It describes a method to acquire portal images during electron beam treatments by using the photon contamination part of the electron beam. It is shown that the image quality obtained with electron beam portal imaging is comparable that obtained with photon beam portal imaging. A method based on MC simulations was also developed to simulate the whole treatment unit including the linac head, voxelized patients and portal imager. This model of the treatment unit can be used to predict portal images which can be used as reference images and compared to images taken during the treatment. The last section of the chapter shows a clinical example of portal images acquired during the electron beam delivery of a head and neck patient.

Chapter 6 consists of a paper submitted to *Physics in Medicine and Biology.* A new technique that uses the accuracy of MC calculations to reconstruct patient dose from an aSi portal image for a 6 MV photon beam is presented. The technique is patient specific and allows a verification of the radiation dose delivered for every treatment fraction. The method also includes a reconstructed and measured portal image comparison which can be used to estimate the accuracy of the dose reconstruction process and detect important patient or organ movement. The dose reconstruction method is validated on phantoms for both conventional and IMRT fields. The last section of the chapter presents a clinical case where the reconstructed dose to a patient is compared to the MC calculated dose.

Finally in chapter 7, we discuss how the image quality of kV CBCT can be improved by correcting for scattered radiation. A full MC model of the kV CBCT bench top is used to investigate the scattered particles distribution under various imaging conditions. A method to correct for scattered radiation is developed and tested. This work was published in part in *Medical Physics* and in part in *SPIE: Medical Imaging Proceedings.*

References

[1] Canadian Cancer Society/National Cancer Institute of Canada (NCIC), 2005.

[2] American Cancer Society (ACS), 2006.

[3] Webb S. *The physics of three dimensional radiation therapy conformal radiotherapy, radiosurgery and treatment planning.* Institute of Physics Publishing, Bristol, UK, 1993.

[4] Webb S. *Intensity modulated radiation therapy.* Institute of Physics Publishing, Bristol, UK, 2000.

[5] Webb S. *Contemporary IMRT-Developing physics and clinical implementation.* Institute of Physics Publishing, Bristol, UK, 2004.

[6] Palta J R and Mackie T R. *Intensity modulated radiation therapy - the state of the art.* Medical Physics Publishing, madison, WI, 2004.

[7] Bentzen S M. Theragnostic imaging for radiation oncology: dose painting by numbers. *Lancet Oncol.*, 6:112–117, 2005.

[8] Andreo P. Monte Carlo techniques in medical radiation physics. *Phys. Med. Biol.*, 36:861–920, 1991.

[9] Rogers D W O, Faddegon B A, Ding G X, Ma C M, Wei J, and Mackie T R. BEAM: A Monte Carlo code to simulate radiotherapy treatment units. *Med. Phys.*, 22:503–524, 1995.

[10] Brahme A. Dosimetric precision requirements in radiation therapy. *Acta Radiol. Oncol.*, 23:379–91, 1984.

[11] Brahme A. Optimized radiation therapy based in radiobiological objectives. *Semin. Radiat. Oncol.*, 9:35–47, 1999.

[12] Langen K M and Jones D T L. Organ motion and its management. *Int. J. Radiat. Oncol. Biol. Phys.*, 50:265–278, 2001.

[13] Dutreix A. When and how can we improve precision in radiotherapy. *Radiother. Oncol.*, 2:271–292, 1984.

[14] van Herk M. Error and margins in radiotherapy. *Semin. Radiat. Oncol.*, 14:52–64, 2004.

[15] Bortfeld T, Jiang S B, and Rietzel E. Effect of motion on the total dose distribution. *Semin. Radiat. Oncol.*, 14:41–51, 2004.

[16] Budgell G J, Mott J H L, Williams P C, and Brown K J. Requirements for leaf position accuracy for dynamic multileaf collimation. *Phys. Med. Biol.*, 45:1211–1227, 2000.

[17] Chui C S, Spirou S, , and LoSasso T. Testing of dynamic multileaf collimation. *Med. Phys.*, 23:635–641, 1996.

[18] LoSasso T, Chui C S, and Ling C C. Physical and dosimetric aspects of a multileaf collimation system used in the dynamic mode for implementing intensity modulated radiotherapy. *Med. Phys.*, 25:1919–1927, 1998.

[19] Jaffray D A and Siewerdsen J H. Cone-beam computed tomography with a flat-panel imager: Initital performance characterization. *Med. Phys.*, 27:1311–1323, 2000.

[20] Waddington S P and McKenzie A L. Assessment of effective dose from concomitant exposures required in verification of the target volume in radiotherapy. *Br. J. Radiol.*, 77:557–561, 2004.

[21] Kudchadker R J, Chang E L, Bryan F, Maor M H, and Famighetti R. An evaluation of radiation exposure from portal films taken during definitive course of pediatric radiotherapy. *Int. J. Radiat. Oncol. Biol. Phys.*, 59:1229–1235, 2004.

[22] Groh B A, Siewerdsen J H, Drake D G, Wong J W, and Jaffray D A. A performance comparison of flat-panel imager-based MV and kV cone-beam CT. *Med. Phys.*, 29:967–975, 2002.

[23] Morr J, DiPetrillo T, Tsai J.-S, Engler M, and Wazer D E. Implementation and utility of a daily ultrasound-based localization system with intensity-modulated radiotherapy for prostate cancer. *Int. J. Radiat. Oncol. Biol. Phys.*, 53:1124–1129, 2002.

[24] Langen K M, Poulliot J, Anezinos C, Aubin M, Gottschalk A R, Hsu I C, Lowther D, Liu Y M, Shinohara K, Verhey L J, Weinberg V, and Roach M 3rd. Evaluation of ultrasound-based prostate localization for image-guided radiotherapy. *Int. J. Radiat. Oncol. Biol. Phys.*, 57:635–644, 2003.

[25] Raaymakers B W, Raaijmakers A J E, Kotte A N T J, Jette D, and Lagendijk J W L. Integrating a MRI scanner with a 6 MV radiotherapy accelerator: dose deposition in a transverse magnetic field. *Phys. Med. Biol.*, 49:4109–4118, 2004.

[26] Uematsu M, Shioda A, Suda A, Tahara K, Kojima T, Hama Y, Kono M, Wong J R, Fukui T, and Kusano S. Intrafractional tumor position stability during computed tomography (CT)-guided frameless stereotactic radiation therapy for lung or liver cancers with a fusion of CT and linear accelerator (FOCAL) unit. *Int. J. Radiat. Oncol. Biol. Phys.*, 48:443–448, 2000.

[27] Midgley S, Millar R M, and Dudson J. A feasibility study for megavoltage cone beam CT using a commercial EPID. *Phys. Med. Biol.*, 43:155–169, 1998.

[28] Mosleh-Shirazi M A, Evans P M, Swindell W, Webb S, and Partridge M. A cone-beam megavoltage CT scanner for treatment verification in conformal radiotherapy. *Radiother. Oncol.*, 48:319–328, 1998.

[29] Kutcher G J, Coia L, Gillin M, Hanson W F, Leibel S, Morton R J, Palta J R, Purdy J A, Reinstein L E, Sventson G F, Weller M, and Wingfield L. Comprehensive QA for radiation oncology: Report of AAPM radiation therapy committee task group 40. *Med. Phys.*, 21:581–618, 1994.

[30] Cunningham J R, Cohen M, Dutreix A, and Walstam R. Determination of absorbed dose in a patient irradiated by beams of X or gamma rays in radiotherapy procedures. Technical Report 24, ICRU, September 1976.

[31] Procedures in external radiation therapy dosimetry with electron and photons beams with maximum energy between 1-50 MeV. Technical report, Nordic Association of Clinical Physicists (NACP), 1980.

[32] Essers M and Mijnheer B. In vivo dosimetry during external photon beam radiotherapy treatments. *Int. J. Radiat. Oncol. Biol. Phys.*, 43:245–259, 1999.

CHAPTER 2
Background Information and Literature Review

This chapter reviews some essential background information. The properties of the electronic portal imaging device (EPID), the cone beam computed tomography (CBCT) scanner, and the Monte Carlo (MC) code used in this study will be discussed. A thorough literature review of the work done in portal imaging dosimetry and in cone-beam scatter correction is also included.

2.1 Electronic Portal Imaging Device

Originally portal imaging was performed using radiotherapy films. Although film is a compact and lightweight technology which provides useful image information, it suffers from major drawbacks. Amongst them, the fact that one must wait several minutes before obtaining an image can limit the number of portal films taken. Moreover film systems offer a limited range of exposure over which the image is neither under- nor over-exposed. EPIDs reduce these limitations by offering real-time digital readout [1]. In this section, the advantages and limitations of the different types of portal imager will be discussed. The amorphous silicon (aSi) EPID will be shown to be the most advantageous portal imaging system for dosimetry. Its applications in external beam dosimetry will be discussed.

2.1.1 EPID Types

There are three main types of electronic portal imagers used clinically today: the camera-mirror-lens based system, the scanning matrix ionization chamber system,

and the active matrix flat panel imager. Table 2–1 gives a summary of the imaging characteristics [1] of the different types of EPID.

Table 2–1: Summary of the imaging characteristics of the three main types of EPID.

Characteristic	Camera-mirror-lens	Scanning matrix ionization chamber	Amorphous silicon
Minimum MU	1 MU	8 MU	1 MU
Acquisition time	0.03 s	1.3 s	0.02 s
Typical FOV	variable	(25×25) cm^2	(30×40) cm^2
Resolution (lp/mm)	0.305	0.258	3.0

The camera-mirror-lens based EPID system consists of an x-ray converter optically coupled to a camera by mean of a mirror and a lens. The converter consists of a metal plate and a phosphor screen. The metal plate converts the primary x-rays into high energy electrons, while the phosphor converts the high energy electrons into visible light. The camera and the lens capture part of the visible light and transform it into a video signal. The mirror is used to fold the beam and ensure that the camera is not in the radiation path. This system is bulky, has low efficiency and suffers from glare [2]. Glare happens when light is reflected within the system and hence signal seems to originate from one part of the screen while in fact it originated from another part.

The scanning matrix ionization chamber system consists of two planes of electrodes, consisting in 256 parallel wires, separated by a gap filled with a fluid. A high voltage is applied to each of the electrodes in succession. The high energy photons

ionize the fluid and the electrons are collected by the electrodes, producing a measurable signal. Although this detector is compact, a relatively high dose is required to form the image and the sampling frequency is lower than for the other EPIDs [1].

The active matrix flat-panel imager, or the aSi EPID, is currently the most promising for dosimetric purposes; it will be discussed in more detail in the next sections.

2.2 The Amorphous Silicon EPID

The aSi EPID consists of a copper plate, a gadolinium oxysulfide phosphor screen, an amorphous silicon flat-panel light sensor, and the associated readout electronics. The copper layer is used as a buildup layer; this ensures electronic equilibrium at the sensitive layer. In fact, investigators have shown that the amount of buildup required depends on the manufacturer. For the Varian aS500, Greer *et al* [3] have shown that for a 6 MV photon beam, 1 mm of copper provides sufficient buildup while for the Elekta IGVIEW EPID 2.4 mm of copper is necessary [4]. The photons will interact in the copper plate where Compton scattering predominantly occurs. The resulting electrons migrate down from the plate into the scintillation screen and deposit energy in it. This causes the screen to phosphoresce, emitting optical photons. Phosphorescence occurs when the incoming photons excite electrons in the crystal lattice so that the electrons become trapped in potential wells. As the electrons fall back to their original energy levels they release their excess energy as optical photons. Each pixel in the flat-panel light sensor consists of a photodiode, which detect the light emitted by the phosphor screen, and two thin film transistors (TFT), which act like switches to control the readout of the recorded signal. The

photodiodes capture the visible light and convert it into an electrical discharge which is proportional to the amount of light reaching the diode. During the readout, the TFT is made conducting to allow current to flow between the photodiode and an external amplifier [5].

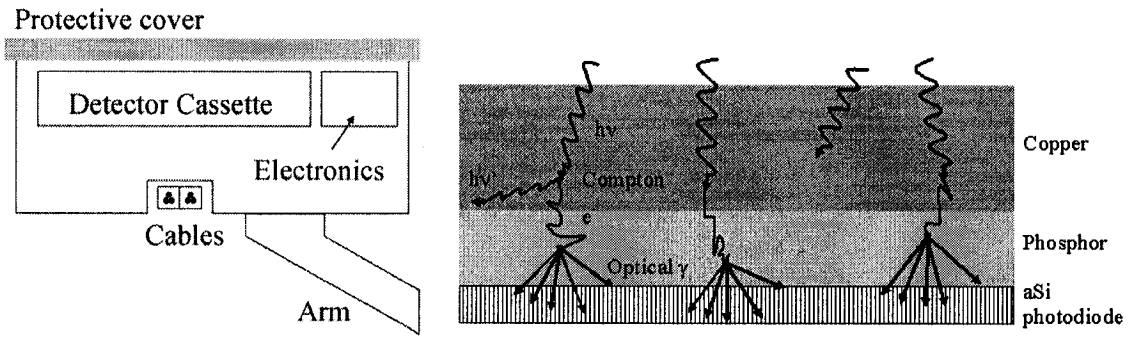

Figure 2–1: (a) Cross section view of an aSi EPID in the couch-gantry direction, and (b) schematic of the detector cassette and the image formation process.

Different flat-panel imager manufacturers have different image acquisition processes. For the Varian aS500 EPID, an image frame is scanned row by row, with a fixed number of rows scanned per beam pulse. Each individual image frame is acquired for ~0.16 s, this time varies slightly with the dose rate setting. The portal imager can be operated under different modes, the most useful mode for IMRT imaging is the *continuous frame averaging mode.* In this mode, a single image consisting of the average of many frames is acquired during radiation delivery. The EPID will average successively acquired frames up to a limit of 9999 frames. The EPID system suffers from a dead time in frame acquisition which occurs every 64 frames, when the content of the frame buffer must be moved to the dynamic random access memory of the CPU. This transfer takes 0.16 s, plus 0.28 s to acquire a reset frame. This dead

time corresponds to the loss of about three images. Greer *et al* [3] showed how the dead time can affect IMRT delivery verification. Recently a patch to the software was released which eliminates the dead time problem as suggested by Manser *et al* [6].

One of the most important advantages of the flat panel light sensor technology for portal imaging is the high quality of the images. The aSi EPID is capable of using around 50% of the light emitted by the scintillator given the following conditions: (1) the array photodiodes are in close proximity to the scintillator, (2) a large fraction of the pixel area is occupied by the photodiode, (3) the efficiency of conversion of light entering the photodiodes into electron-hole pairs is high, and (4) the efficiency of readout of the signal from the pixels is also high.

2.2.1 The aSi EPID Dosimetric Characteristics

The aSi EPID also has appealing properties as a dosimeter; these have been thoroughly studied by various research groups. Some of its main advantages are its linear dose and dose rate response and its long and short term reproducibility [3, 5, 7–9]. Kirby and Sloboda [10] observed a linear trend of dose versus energy for energies higher than 1 MeV, however the dose response deviates significantly from this trend for energies lower than 1 MeV. A sharp dose increase is observed at low energy due to the sharp increase in mass energy absorption coefficient of the gadolinium oxysulfide. This effect is important as it may have repercussions on the dose calibration curve at low energies. However, by adding buildup material it is possible to reduce the non-linear response at low energies [10]. Glare, due to optical dispersion within the phosphor layer, may also be a limitation for this type of portal imager. McCurdy *et al* [7] found that glare contributes significantly to the signal. However, Munro and

Bouius [5] concluded that glare was negligible for this type of EPIDs; other studies came to that same conclusion [11–13].

The aSi EPID is especially interesting in the case of IMRT dosimetry due to its short acquisition time and to its good response to rapid changes in dose rate [3]. In acquiring images of rapidly changing fields it is important to have a negligible ghosting effect. Ghosting effects can be divided in image lag and change in sensitivity or gain of the pixels. Image lag is a signal delay, so charge generated in one image frame is read out in subsequent frames, adding an offset to the signal. In aSi detectors, the dominant source of image lag is the trapping and releasing of charges in the sensor elements. A second source of image lag is phosphor afterglow. Another type of ghosting, while also related to charge trapping, has been associated with change in gain. During exposure, the charge stored in deep trapping states alters the electric field strength within the photodiode bulk and interface layer. This will change the sensitivity of the aSi layer [14]. Different studies have observed different amounts of ghosting. Greer *et al* [3] reports ghosting of the order of 0.2%, while Winkler *et al* [15] observed ghosting effect up to 3% for short time interval between exposure.

2.2.2 The aSi EPID Calibration

In order to use portal images for dosimetric purposes it is important to develop a calibration technique to go from EPID signal to dose. Two main approaches have been developed for the calibration of the aSi portal imager. Grein *et al* [16] obtained a relationship between absorbed dose and aSi EPID pixel value by comparing EPID central average value and ion chamber readings taken with 1.5 cm of solid water

for buildup. They found a linear relationship which holds for different detector distances and field sizes. Siebers *et al* [11] chose a MC approach in which measured and simulated flood fields are used to obtain a pixel-by-pixel calibration matrix. This calibration can be used to transform EPID signal to dose to the phosphor.

2.2.3 The aSi EPID Dosimetric Applications in Photon Beam Radiotherapy

The aSi EPID abilities as a patient positioning tool and as a dosimeter for conformal photon treatments and for IMRT have already been discussed in various studies [3, 8, 11]. There are two accepted approaches to portal imaging dosimetric verification: (i) comparison of a predicted fluence or dose at the detector with a portal image acquired during the treatment [7, 9, 17, 18], and (ii) reconstruction of the dose in the patient from the portal image [19–24]. The first technique has been mostly used in pre-treatment verification. The portal image is predicted using a modified treatment planning software [9] or using MC simulations [17]. The comparison of the predicted and actual portal images indicates if the field sequence was delivered correctly. It does not calculate the actual dose delivered to the patient. Different approaches have been explored for dose reconstruction. McNutt *et al* [19] proposed to use an iterative convolution/superposition algorithm to reconstruct the dose distribution in patient. The iterative method begins by assuming that the primary energy fluence at the portal imager plane is equal to the portal image. The primary energy fluence is back-projected through the phantom and convolved with a dose deposition kernel. The convolution/superposition method re-computes the dose throughout an extended phantom which includes the portal imager. This new portal image is used and the iterative process is repeated until convergence is observed. The method was

compared against treatment planning system dose prediction and agreement within 3% was obtained. Wendling *et al* [24] adapted a technique previously developed by Boellaard *et al* [21] and Louwe *et al* [25] for IMRT deliveries. The technique uses back-projection of primary fluence and pre-calculated scatter dose in phantom to obtain in-vivo dose. The technique was shown to work for IMRT fields in homogeneous phantoms. Another approach based on back-projection is to ray-trace the primary fluence at the detector through a CT of the patient; an inverse attenuation correction is used to obtained an input fluence between the patient and the linear accelerator (linac) [22, 23]. The primary fluence at the detector is obtained by correcting for scattered radiation using pre-calculated kernels. The back-projected input fluence is then used to calculate the patient dose using a convolution/superposition method [22] or a treatment planning system [23]. Most dose reconstruction techniques are limited when non-homogeneous phantoms are used since they rely on pre-calculated kernels in homogeneous water. Van Elmpt *et al* [26] applied MC simulations to a back-projection technique. They developed an IMRT pre-treatment verification tool where the dose is calculated in a phantom using MC simulations. Their method requires an image acquired before the treatment without the patient or phantom in the beam. They can extract the primary fluence directly from this portal image; however, it is impossible to detect errors that occur during the delivery such as leaf position errors since only a pre-treatment image is acquired.

2.2.4 Treatment Verification of Electron Beam Radiotherapy

In the case of electron beam radiotherapy, portal imaging is not used clinically. Various electron beam delivery techniques such as the combination of high energy

electrons in conjunction with photons, the use of abutting fields or electron modulated radiotherapy may benefit from portal imaging. Keller [27] first suggested using the bremsstrahlung contamination in high energy electron beams to obtain electron beam radiographs. Gur *et al* [28] acquired both conventional films and storage phosphor images from 22 patients during their daily high energy electron beam treatments. They showed that the verification images obtained during the electron treatments are true projection images of the treatment field by comparison of images obtained with a photon beam. Baus and Vetterli [29] were among the first to suggest the use of the aSi EPID for electron beam verification. Aubin *et al* [30, 31] suggested that it is possible to use the aSi EPID for routine clinical on-line electron beam verification. They obtained images of an anthropomorphic phantom, and showed that electron multi-leaf collimator shapes can be verified. More recently, Hansen [32] suggested using the aSi EPID in head and neck cases where electron fields are used to match photon fields.

2.3 Cone Beam Computed Tomography

CBCT is a new technology which allows the acquisition of three-dimensional (3D) images from two-dimensional (2D) projections. Swindell *et al* [33] first proposed to use the treatment beam to perform MV computed tomography of the patient in the treatment position. The cone-beam implementation of that idea was first investigated by Mosleh-Shirazi *et al* [34]. Although utilization of the MV source is practical since the same source is used to treat and image, it faces important challenges posed by the poor detection efficiency of x-ray detectors in the MV energy range. The low efficiency can result in poor signal-to-noise ratio performance for clinically acceptable

dose. Integrating a kV x-ray source and a large area flat-panel detector on a medical linac is another alternative which is referred to as kV CBCT. In the next sections, the kV CBCT technology will be discussed in more details. The limitations in image quality will be explained and some of the innovative applications will be described.

2.3.1 Image Acquisition and Reconstruction

A kV CBCT system operates on the same principles as conventional CT, except that it allows a volumetric CT image to be reconstructed from data collected during a single rotation of the gantry. Large cone and fan angles are used to encompass the whole field of view and a flat-panel imager is used to obtain 2D projections (figure 2–2). Most reconstruction algorithms are based on the method developed by Feldkamp *et al* [35]. In Feldkamp type algorithms each horizontal row of detector values is ramp-filtered just as if they were projections of a 2D object. The filtered projection data is then back projected along the original rays.

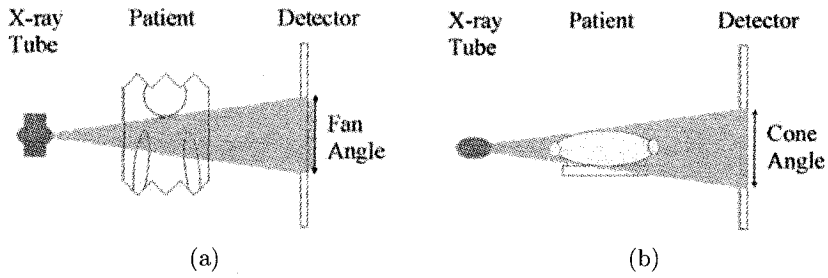

Figure 2–2: (a) Top view and (b) side view schematic of the kV CBCT geometry.

2.3.2 Image Characteristics

Jaffray and Siewerdsen [36] showed that kV CBCT images demonstrate reasonable volumetric uniformity, noise, and spatial resolution characteristics. Measurement of image noise versus exposure demonstrated that CBCT systems perform comparably to conventional CT scanners, following the inverse square root exposure dependence predicted by theory. Investigators have shown that the flat-panel detector has some potential advantages: compactness, absence of geometric distortion and veiling glare, high resolution, high detective quantum efficiency (DQE), high frame rate, high dynamic range, and excellent linearity (1%) [37]. Some limitations of the system are in the detector performance, the image lag, and the x-ray scatter. Image lag can result in subtle artifacts in regions of high-contrast objects at high exposures [38, 39]. However such effects can be largely eliminated through simple procedural and/or algorithmic methods.

X-ray scatter remains the main limitation in kV CBCT. Investigations of x-ray scatter in conventional CT have demonstrated experimentally and analytically that scatter results in artifacts and inaccuracies in reconstructed CT numbers [40–42]. X-ray scatter is more important in CBCT than in fan-beam CT due to the larger cone angle employed and to the lack of post-patient collimation in the 2D detectors used to acquire the images. This scatter contribution degrades the image quality by degrading the contrast, by increasing the noise and by introducing artifacts [43]. Techniques to reduce the scatter contribution include increasing the air gap between the object and the detector and using anti-scatter grids [44, 45]. Other correction techniques

are based on analytical prediction of scatter [46] and empirical methods [45, 47, 48], such as beam stop array techniques.

The magnitude and effects of x-ray scatter in CBCT kV imaging has been studied using empirical techniques such as beam stop arrays [37] and blocks [43, 49]. Analytical models have also been used to study the scatter contribution in diagnostic radiology [40, 50]. However, these models are limited when complex geometries or heterogeneous media are involved. MC simulations have previously been used to study the scattered radiation distribution in diagnostic radiology and they were shown to be the most successful method for the investigation of the production of scattered particles in a medium. Section 2.4.2 will give more details on MC simulations of scattered radiation.

2.3.3 Applications

In the last few years an impressive amount of new CBCT imaging applications has emerged. The compact nature of the panel allows CBCT imagers to be used in situations that would never be considered feasible for a conventional CT scanner. One of these applications is 3D breast imaging, which can potentially result in more accurate diagnosis of structures and patterns of lesions while eliminating the hard compression of breasts [51, 52]. Applications in angiography [37, 53] and in craniofacial imaging [54] have also been investigated. In the radiotherapy field, it is its applications in image guided radiation therapy (IGRT) that are very promising. CBCT produces volumetric images of patients in the treatment position and provides soft-tissue contrast essential for IGRT. These images can be used to realign patients. For such an application, high soft tissue contrast is necessary as positioning based on

bony structures can lead to errors in the soft tissue alignment. The CBCT images can also be used to re-calculate the treatment plan on a day-to-day basis. In that case it is essential to have accurate CT numbers to assign the exact material and density to the voxels in the treatment planning voxelized geometry.

2.4 Monte Carlo Simulations

The MC technique has been used extensively in medical physics applications; many reviews can be found in the literature [55–57]. Andreo [55] describes the MC technique and discusses some of its applications in medical physics. Verhaegen and Seuntjens [56] review the modeling of external radiotherapy photon beams while Ma and Jiang [57] do the same for electron beams. This section will describe the fundamentals of MC simulations. It includes a short overview of the physics behind MC simulations, a description of the EGSnrc MC code, as well as some of its applications in radiation therapy.

2.4.1 Monte Carlo Technique for Radiotherapy

The MC method encompasses any technique of statistical sampling employed to approximate solutions to quantitative problems. In radiotherapy MC simulations are used to provide solutions to the radiation transport equation by modeling individual interactions between particles. MC uses probability distribution functions and a pseudo-random number generator to sample interaction properties such as angles and energy losses. Average values of macroscopic quantities such as particle fluence, energy spectrum and absorbed dose distribution can be calculated by simulating a large number of particle histories. A history consists of a complete account of one particle transport including the transport of its secondary particles. It is widely

accepted that MC simulation of radiation transport is one of the most accurate methods for predicting absorbed dose distribution in radiotherapy.

Photon Transport. In the radiotherapy energy range, four types of photon interactions are dominant: Compton interactions, photoelectric interactions, pair production in the nuclear field, and Rayleigh interactions. The particle path length in a medium, l, is evaluated using the equation

$$l = -\lambda \ln(1 - R) \tag{2.1}$$

where λ is the mean free path as a function of medium and particle energy, and R is a random number. The mean free path is defined as the inverse of the attenuation coefficient μ.

Once l is calculated, the photon is transported to the interaction point. The type of interaction is sampled from the appropriate relative probability obtained from the ratio of the cross sections. The particle's resultant energy, position and direction can then be calculated by sampling these quantities from the appropriate differential probability distribution functions. Different techniques exist to sample the probability distributions describing photon interactions. Each particle history is terminated when the particle leaves the region of interest or when the energy of the particle falls below an energy cutoff specified by the user.

Absorbed Dose Calculation for Photon Beams. The absorbed dose is defined as the expectation value of the energy imparted to matter per unit mass at a point. In MC simulations the absorbed dose is typically calculated by summing the energy deposited by the secondary electrons in a given user defined region and

dividing by the mass of that region. This dose scoring technique requires transport of the secondary electrons and can be time consuming due to the small number of interactions producing secondary electrons. Another technique to obtain the absorbed dose is based on the fact that absorbed dose is equal to collision kerma when charged particle equilibrium is achieved. The collision kerma is the expectation value of the net energy transferred to charged particles per unit mass at the point of interest, excluding both the radiative energy loss and the energy passed from one charged particle to another. For monoenergetic photons, the collision kerma is equal to the energy fluence times the mass energy absorption coefficient. The photon fluence ϕ can be obtained using a track-length estimate. The particle flux Φ is obtained by

$$\Phi = \nu N \tag{2.2}$$

where ν is the particle velocity and N is the particle density. The particle fluence can be obtained by integrating the particle flux over time t, or equivalently by integrating over distance s by using the relation $\mathrm{d}s = \nu \mathrm{d}t$. The integral is given by

$$\phi = \int_V \int_t \Phi \mathrm{d}t \frac{\mathrm{d}V}{V} = \int_V \int_s \frac{N}{V} \mathrm{d}s \mathrm{d}V \tag{2.3}$$

MC algorithms estimate this integral by summing it over all particle tracks in a given region. It is generally quite reliable because there are many tracks in a region compared to the number of collisions.

Electron Transport. The transport of electrons is considerably more complicated than that of photons. In the process of slowing down, a typical fast electron undergoes on the order of 10^5-10^6 collisions with the surrounding matter. Electrons can

undergo Møller scattering, Bhabha scattering, atomic excitation, bremsstrahlung, elastic scattering from atoms (mostly nuclei), and positron annihilation. The very large number of interactions that take place during electron transport makes it unrealistic to simulate all the physical interactions. Instead, condensed history techniques [58], where large numbers of transport and collision processes are condensed into a single electron step, have been developed. This approach is motivated by the fact that single collisions with the atoms cause in most cases only minor changes in the particle's energy and direction of travel.

Variance Reduction Techniques. The small number of interactions taking place when photons traverse matter has motivated the development of variance reduction techniques to decrease the statistical uncertainties. Forced interactions, Russian roulette, particle splitting, and range rejection are a few of these techniques [59]. A useful quantity for assessing the effect of a certain variance reduction technique is the efficiency ϵ,

$$\epsilon = \frac{1}{\sigma_{\text{rel}}^2 T} \tag{2.4}$$

where T is the total simulation time and σ_{rel} is the relative error.

The Monte Carlo Codes. The four principal components of a MC code are: (1) the cross section data for the processes to be simulated, (2) the algorithms for particle transport, (3) the methods for geometry specification (usually defined by the user), and (4) the tools for data analysis. Another essential component of a MC code is a random number generator which is used for sampling the quantities of interest from a probability distribution function. Some of the well known MC codes are

EGS [60], MCNP [61], PENELOPE [62] and GEANT [63]. One of the most popular MC codes in radiotherapy and the one used in this thesis is EGSnrc (Electron-Gamma-Shower) [60, 64, 65]. The EGSnrc code is a general purpose package for the MC simulation of the coupled transport of electrons and photons in an arbitrary geometry for particles with energies above a few keV up to several GeV. It can simulate the following physical processes:

1. photoelectric effect with atomic relaxations after creation of a vacancy, including creation of Auger and Coster-Kronig electrons and emission of fluorescent photons from K, L, M shells;
2. Rayleigh scattering;
3. Compton scattering;
4. pair and triplet(not explicitly simulated) production;
5. positron annihilation in flight and at rest;
6. Bremsstrahlung production with EGS4 or NIST cross-sections;
7. multiple-scattering with relativistic spin effect or screened Rutherford elastic scattering and single elastic scattering for short step sizes; and
8. Møller and Bhabha treatment of inelastic scattering for electrons and positrons.

The electron transport for the EGSnrc system was shown to produce an accurate implementation of the condensed history technique for the most stringent tests of ion chamber simulations and backscattering scenarios [66].

The cross-section data can be created using PEGS4. The cross-sections for photons interactions are based on the data of Storm and Israel [67], updated to

XCOM, while the stopping powers are imported from the NIST database developed by Berger and Seltzer [68].

The ESGnrc package encompasses BEAMnrc, DOSXYZnrc and other user codes which are coded in mortran. The BEAM/EGSnrc [69] user interface allows easy modeling of radiotherapy linacs, Cobalt units and kV x-ray units using component modules (CM). Each CM is a simple geometric shape that varies from a simple slab to the complicated structure of multi-leaf collimators. Each CM is independent of each other and can be stacked up in series to build a complete linac. The BEAM code produces a phase space output of the beam after any specified CM. This phase space file includes information about the particles position, direction, energy, weight, and charge. The phase space file can also include information such as in which CM the particle was created. The EGSnrc code also includes user codes for dose calculation such as DOSXYZnrc and DOSRZnrc [70]. These programs calculate the dose deposited in a 3D voxel cartesian or cylindrical geometry.

2.4.2 Modeling

Linear Accelerator. In the photon beam configuration, an electron beam hits a high Z material target. The production of bremsstrahlung photons is simulated. Various parameters of the electron beam can be tuned such as the initial electron beam spectrum or energy, its spatial distribution, and its angular distribution. Previous studies [71, 72] have shown that changes in primary electron energy of a few percent or changes in the radial intensity distribution have a significant impact on the photon beam produced. However, the simulations were found to be insensitive to the energy spread of the initial electron beam. Photons that are created

in the target go through the primary collimators, the flattening filter, the monitor ion chamber, the mirror, the upper and lower jaws, and the multi-leaf collimator. Patau *et al* [73] were the first to simulate a complete linac. Since then, several studies have looked at modeling linacs for various purposes such as characterizing the head scatter [74], designing flattening filters [75], or improving treatment planning [76]. Verhaegen and Seuntjens [56] give a full literature review of MC modeling of external radiotherapy photon beams. Studies have also looked at simplifying the modeling of certain linac components; especially in the case of the MLC where full simulations can be time consuming due to the complex geometry. Siebers *et al* [77] developed an algorithm to simplify the MLC modeling. Their model divides the MLC into simple geometric regions and transport photons considering only Compton interactions. They demonstrate that their model reproduces measurements within 1% or 1 mm.

A typical electron configuration model can include a monitor ion chamber, shielding, jaws, a reticule, applicators, and cut-outs. Udale-Smith [78–80] was the first to fully model a linac in electron beam configuration; various investigators followed her steps [69, 81, 82]. Recently many groups have looked into obtaining better agreement between measurements and simulations. Schreiber and Faddegon [83] showed that variation of 5% in the initial energy of the electron beam can produce changes of up to 4% in the shoulder of large field profiles. Huang *et al* [84] also showed the importance of modeling adequately the spatial distribution of the incident beam especially when simulating large electron fields.

Kilovoltage Units. Contrary to the modeling of MV linacs where an impressive amount of effort has been put, kV units have been somewhat neglected.

However MC simulations of kV units can be very useful in assessing and optimizing the image quality of a system or in computing the radiation dose given to patients. Different approaches are possible when simulating an x-ray unit. The x-ray unit can be simulated completely, including the primary electron hitting the target, or a pre-calculated spectrum can be used. Similarly the filtration can be simulated by modeling exactly the filter or it can be included in the spectrum calculation. The other components of the kV unit such as the collimation are usually fully modeled. Verhaegen *et al* [85] used the EGS4/BEAM and MCNP MC codes to build realistic models of two complete x-ray units used for radiotherapy treatment. Various studies have used MC simulations to model CT scanners to develop radiation dose calculation tools [86–89] or to investigate artifact production and correction [90] . Other investigators have used general-purpose codes or developed their own code to investigate the scattered radiation components in diagnostic radiology [50, 91–93].

Patients and Phantoms. Several research groups have reported on the implementation of the MC method for clinical radiotherapy dose calculations [94–102]. For general dose calculation and linac model validation a water phantom or an anthropomorphic phantom, consisting in a typical male and/or female geometry where each organ is represented by a geometrical shape, can be modeled. However MC treatment planning requires patient specific models. MC models are based on voxelized geometries where voxels are filled by different material according to the CT patient data. The assignment of materials to the voxels is prone to error which can introduce dose calculation errors. A recent study by Verhaegen and Devic [103] showed that mis-assignment of media and/or mass-density can lead to significant

dose errors up to 10% in certain regions for MV photon beams and more than 30% for high energy electron beams.

EPIDs and Detectors

MC simulations have been used to model detectors dedicated to portal imaging and to diagnostic imaging. The role of MC simulations can be divided in two categories: (1) calculation of detector signal for dosimetric purposes and (2) characterization and optimization of detectors.

In order to use the portal imager as a dosimeter, a method to predict portal dose is needed. For this purpose, an accurate representation of the radiation field impinging on the detector together with a dosimetric characterization of the detector is required. Swindell and Evans [104] used MC simulations to investigate the scatter signal in the portal imager. Spezi and Lewis [17] developed a MC model of a scanning liquid ion chamber EPID. The MC simulation can be used to predict portal images which can be compared to the actual portal image to detect discrepancies in dose delivery. For similar purposes, Siebers *et al* [11] developed a MC model of the aS500 EPID. Their model was used for dosimetric purposes and to investigate the optimal backscatter amount [105].

MC simulations are also used to characterize and optimize detectors. At MV energies the optimization of the system is essential due to the intrinsic limitation in subject contrast. To this purpose, the stages of quantum propagation in various detector systems have been analyzed with the help of MC calculations. Kausch *et al* [12] investigated metal plate/phosphor screens and photodiode array readout techniques. Their MC simulations showed that there exists an optimal thickness of metal

plate to maximize the DQE. Similar improvements to imaging systems have been inferred from MC simulations by other investigators [106–109]. MC simulations have also been used in the design of digital x-ray detectors. Boone *et al* [110] studied the x-ray scattering and the x-ray fluorescence properties of seven different x-ray detector materials. Thacker *et al* [111] investigated optimal camera design parameters and imaging techniques. They used the Geant 3 MC code to model x-ray transport and absorption within the CsI scintillator, and the DETECT-II code to track optical photon spread within a columnar model of the CsI scintillator.

Another interesting area of research using MC simulations is the investigation of the production of scattered particles. MC simulations were used to study how the scatter fraction varies with different imaging parameters [91] and to study the angular, spectral and spatial distribution of the scattered particles [92] for monoenergetic point sources in the diagnostic energy range. Boone and Seibert [50] used MC techniques to evaluate the point spread function of scattered radiation in diagnostic radiology. Recently Malusek *et al* [93] used MC simulations to predict the scattered radiation in CBCT projection images. They used a simplified CT scanner geometry which consisted of a point source emitting mono-energetic photons or a spectrum of photons, different phantoms and a cylindrical detector array. Ay and Zaidi [89] used the MCNP4C code to model fan and cone beam systems. They studied the effect of bow-tie filters, phantom sizes and grid septa length on the scatter distribution.

A significant amount of work has been done in the field of treatment verification and MC modeling; however, there are still areas that can be improved. Building on the work of previous investigators, we developed novel techniques to improve

patient positioning verification and dosimetric verification. These new methods will be presented in the next chapters.

References

[1] Antonuk L E. Electronic portal imaging devices: a review and historical perspective of contemporary technologies and research. *Phys. Med. Biol.*, 47:R31–R65, 2002.

[2] Munro P. Megavoltage radiography for treatment verification. In *The Modern Technology of Radiation Oncology A Compendium for Medical Physicists and Radiation Oncologists*, editors, J van Dyk, chapter 13. Madison Medical Physics Publishing, Madison, 1999.

[3] Greer P B and Popescu C C. Dosimetric properties of an amorphous silicon electronic portal imaging device for verification of dynamic intensity modulated radiation therapy. *Med. Phys.*, 30:1618–1627, 2003.

[4] McDermott L N, Louwe J W, Sonke J J, van Herk M B, and Mijnheer B J. Dose-response and ghosting effects of an amorphous silicon electronic portal imaging device. *Med. Phys.*, 31:285–295, 2004.

[5] Munro P and Bouius D C. X-ray quantum limited portal imaging using amorphous silicon flat-panel arrays. *Med. Phys.*, 25:689–702, 1998.

[6] Manser P, Treier R, Riem H, Fix M K, Vetterli D, Mini R, and Ruegsegger P. Dose response of an A-Si:H EPID on static and dynamic photon beams (abstract). *Med. Phys.*, 29:1269, 2002.

[7] McCurdy B M C, Luchka K, and Pistorius S. Dosimetric investigation and portal dose image prediction using an amorphous silicon electronic portal imaging device. *Med. Phys.*, 28:911–924, 2001.

[8] El-Mohri Y, Antonuk L E, Yorkston J, Jee K W, Maolinbay M, Lam K L, and Siewerdsen J H. Relative dosimetry using active matrix flat-panel imager (AMFPI) technology. *Med. Phys.*, 26:1530–1541, 1999.

[9] van Esch A, Depuydt T, and Huyskens D P. The use of an aSi-based EPID for routine absolute dosimetric pre-treatment verification of dynamic IMRT fields. *Radiother. Oncol.*, 71:223–234, 2004.

[10] Kirby C and Sloboda R. Consequences of the spectral response of an a-Si EPID and its implications for dosimetric calibration. *Med. Phys.*, 32:2649–2658, 2005.

[11] Siebers J V, Kim J O, Ko L, Keall P J, and Mohan R. Monte Carlo computation of dosimetric amorphous silicon electronic portal images. *Med. Phys.*, 31:2135–2146, 2004.

[12] Kausch C, Schreiber B, Kreuder F, Schmidt R, and Dossel O. Monte Carlo simulations of the imaging performance of metal plate/phosphor screens used in radiotherapy. *Med. Phys.*, 26:2113–2124, 1999.

[13] Schach von Wittenau A E, Logan C M, Aufderheide 3rd M B, and Slone M. Blurring artifacts in megavoltage radiography with a flat-panel imaging system: comparison of Monte Carlo simulations with measurements. *Med. Phys.*, 29:2559–2570, 2002.

[14] Pang G, Lee D L, and Rowlands J A. Investigation of a direct conversion flat panel imager for portal imaging. *Med. Phys.*, 28:2121–2128, 2001.

[15] Winkler P, Hefner A, and Georg D. Dose-response characteristics of an amorphous silicon EPID. *Med. Phys.*, 32:3095–3105, 2005.

[16] Grein E E, Lee R, and Luchka K. An investigation of a new amorphous silicon electronic portal imaging device for transit dosimetry. *Med. Phys.*, 29:2262–2268, 2002.

[17] Spezi E and Lewis D G. Full forward Monte Carlo calculation of portal dose from MLC collimated treatment beams. *Phys. Med. Biol.*, 47:377–390, 2002.

[18] van Elmpt W J, Nijsten S M J J G, Mijnheer B J, and Minken A W H. Experimental verification of a portal dose prediction model. *Med. Phys.*, 32:2805–2818, 2005.

[19] McNutt T R, Mackie T R, Reckwerdt P, and Paliwal B R. Modeling dose distributions from portal dose images using the convolution/superposition method. *Med. Phys.*, 23:1381–1392, 1996.

[20] Hansen V N, Evans P M, and Swindell W. The application of transit dosimetry to precision radiotherapy. *Med. Phys.*, 23:713–721, 1996.

[21] Boellaard R, Essers M, van Herk M, and Mijnheer B J. New method to obtain the midplane dose using portal in vivo dosimetry. *Int. J. Radiat. Oncol. Biol. Phys.*, 41:465–474, 1998.

[22] Partridge M, Ebert M, and Hesse B-M. IMRT verification by three-dimensional dose reconstruction from portal beam measurements. *Med. Phys.*, 29:1847–1858, 2001.

[23] Steciw S, Warkentin B, Rathee S, and Fallone B G. Three-dimensional IMRT verification with a flat-panel EPID. *Med. Phys.*, 32:600–612, 2005.

[24] Wendling M, Louwe R J W, McDermott L N, Sonke J-J, van Herk M, and Mijnheer J. Accurate two-dimensional IMRT verification using a back-projection EPID dosimetry method. *Med. Phys.*, 33:259–273, 2006.

[25] Louwe R J W, Damen E M F, van Herk M, Minken A W H, Torzsok O, and Mijnheer B J. Three-dimensional dose reconstruction of breast cancer treatment using portal imaging. *Med. Phys.*, 30:2376–2389, 2003.

[26] van Elmpt W J, Nijsten S M J J G, Schiffeleers R F H, Dekker A L A J, Mijnheer B J, Lambin P, and Minken A W H. A Monte Carlo based three-dimensional dose reconstruction method derived from portal dose images. *Med. Phys.*, 33:2426–2434, 2006.

[27] Keller B E. Electron-beam radiographs. *Radiology*, 128:830–831, 1978.

[28] Gur D, Weiser J C, Deutsch M, Furhrman C R, Gennari R C, and Rosenthal M S. Verification of electron beam therapy with conventional and storage phosphor images: preliminary experience. *Int. J. Radiat. Oncol. Biol. Phys.*, 17:1337–1340, 1989.

[29] Baus W and Vetterli D. Electron beam verification using electronic portal imaging - test of a commercial a-Si based system. *Proceedings of the 6th International Workshop on Electronic Portal Imaging*, page 64, 2000.

[30] Aubin M, Faddegon B, and Pouliot J. Electron beam verification with an A-Si flat panel electronic portal imaging device. *Progress in Biomedical Optics and Imaging*, 3:549–557, 2002.

[31] Aubin M, Faddegon B, and Pouliot J. Clinical implementation of electron beam verification with an a-Si EPID (abstract). *Med. Phys.*, 29:1242, 2002.

[32] Hansen V N. Feasibility study of imaging head and neck electron fields using an ASi EPID. In *Proceedings of the 8th International Workshop on Electronic Portal Imaging*, Brighton,UK, June 2004.

[33] Swindell W, Simpson R G, Oleson J R, Chen C T, and Grubbs E A. Computed tomography with a linear accelerator with radiotherapy applications. *Med. Phys.*, 10:416–420, 1983.

[34] Mosleh-Shirazi M A, Evans P M, Swindell W, Webb S, and Partridge M. A cone-beam megavoltage CT scanner for treatment verification in conformal radiotherapy. *Radiother. Oncol.*, 48:319–328, 1998.

[35] Feldkamp L A, Davis L C, and Kress J W. Practical cone-beam algorithm. *J. Opt. Soc. Am. A.*, 1:612–619, 1984.

[36] Jaffray D A and Siewerdsen J H. Cone-beam computed tomography with a flat-panel imager: Initital performance characterization. *Med. Phys.*, 27:1311–1323, 2000.

[37] Ning R, Chen B, Yu R, Conover D, Tang X, and Nong Y. Flat panel detector-based cone-beam volume CT angiography imaging: system evaluation. *IEEE Transactions on Medical Imaging*, 19:949–963, 2000.

[38] Siewerdsen J H and Jaffray D A. A ghost story: Spatio-temporal response characteristics of an indirect-detection flat-panel imager. *Med. Phys.*, 26:1624–1641, 1999.

[39] Siewerdsen J H and Jaffray D A. Cone-beam computed tomography with a flat-panel imager: Effect of image lag. *Med. Phys.*, 26:2635–2647, 1999.

[40] Johns P C and Yaffe M. Scattered radiation in fan beam imaging systems. *Med. Phys.*, 9:231–239, 1982.

[41] Glover G H. Compton scatter effects in CT reconstructions. *Med. Phys.*, 9:860–867, 1982.

[42] Hsieh J. Image artifacts, causes, and corrections. In *Medical CT, Ultrasound: Current Technology, and Applications*, editors, L. W. Goldman and J. B. Fowlkes, pages 487–518. Advanced Medical, Madison,WI, 1995.

[43] Siewerdsen J H and Jaffray D A. Cone-beam computed tomography with a flat-panel imager: Magnitude and effects of x-ray scatter. *Med. Phys.*, 28:220–231, 2000.

[44] Siewerdsen J H and Jaffray D A. Optimization of x-ray imaging geometry with specific application to flat panel cone-beam computed tomography. *Med. Phys.*, 27:1903–1914, 2000.

[45] Ning R, Tang X, and Conover D. X-ray scatter correction algorithm for cone beam CT imaging. *Med. Phys.*, 31:1195–1202, 2004.

[46] Hopkins F, Du Y, Lasiuk B, Abraham A, and Basu S. Analytical corrections for beam-hardening and object scatter in volumetric computed tomography systems. In *16th world conference on nondestructive testing*, Montreal, Canada, 2004.

[47] Siewerdsen J H, Daly M J, Bakhtiar B, Moseley D J, Richard S, Keller H, and Jaffray D A. A simple, direct method for x-ray scatter estimation and correction in digital radiography and cone beam CT. *Med. Phys.*, 33:187–197, 2006.

[48] Liu X, Shaw C, Altunbas M, and Wang T. A scanning sampled measurement (SSM) technique for scatter measurement and correction in cone beam breast CT (abstract). *Med. Phys.*, 32:2093, 2005.

[49] Kwan A L C, Boone J M, and Shah N. Evaluation of x-ray scatter properties in a dedicated cone-beam breast CT scanner. *Med. Phys.*, 32:2967–2975, 2005.

[50] Boone J M and Seibert J A. Monte Carlo simulation of the scattered radiation distribution in diagnostic radiology. *Med. Phys.*, 15:713–720, 1988.

[51] Chen B and Ning R. Cone-beam volume CT breast imaging: Feasibility study. *Med. Phys.*, 29:755–770, 2002.

[52] Huang S, Yang K, Kwan A, and Boone J. Computational evaluation of breast geometry from breast CT. *Med. Phys.*, 33:2287, 2006.

[53] Fahrig R, Fox A J, and Haldsworth D W. Three-dimensional CT angiography from a clinical C-arm mounted. In *Proceedings RSNA 82nd Scientific Assembly.* RSNA, December 1996.

[54] Tsiklakis K, Syriopoulos K, and Stamatakis H C. Radiographic examination of the temporomandibular joint using cone beam computed tomography. *Dentomaxillofac. Radiol.*, 33:196–201, 2004.

[55] Andreo P. Monte Carlo techniques in medical radiation physics. *Phys. Med. Biol.*, 36:861–920, 1991.

[56] Verhaegen F and Seuntjens J. Monte Carlo modeling of external radiotherapy photon beam. *Phys. Med. Biol.*, 48:R107–R164, 2003.

[57] Ma C M and Jiang S B. Topical Review: Monte Carlo modeling of electron beams from medical accelerators. *Phys. Med. Biol.*, 44:R157–R189, 1999.

[58] Berger M J. Monte Carlo calculation of the penetration and diffusion of fast charged particles. *Methods in Comput. Phys*, 1:135, 1963.

[59] Bielajew A F and Rogers D W O. Variance reduction techniques. In *Monte Carlo Transport of Electrons and Photons*, editors, Jenkins T M and Nelson W R and Rindi A. Plenum, New York, 1988.

[60] Kawrakov I and Rogers D W O. The EGSnrc code system: Monte Carlo simulation of electron and photon transport. PIRS 701, NRCC, 2003.

[61] Briesmeister J F. MCNP - a general Monte Carlo N-particle transport code. Technical Report LA-12625-M, Los Alamos Natl. Lab., 1993.

[62] Salvat F, Fernandez-Varea J M, and Sempau J. *PENELOPE, a code system for Monte Carlo simulation of electron and photon transport.* OECD Nuclear Energy Agency, 2001.

[63] Agostinelli S *et al.* Geant4 - a simulation toolkit. *Nucl. Inst. and Meth. in Phys. Research, Section A*, 506:250–303, 2003.

[64] Kawrakow I. Accurate condensed history Monte Carlo simulation of electron transport I. EGSnrc, the new EGS4 version. *Med. Phys.*, 27:485–498, 2000.

[65] Kawrakov I and Rogers D W O. The EGSnrc system status report from advanced Monte Carlo for radiation physics, particle transport simulation and applications. In *proceedings of the Monte Carlo 2000 Conference*, Lisbon, October 2000. Springer.

[66] Kawrakow I. Accurate condensed history Monte Carlo simulation of electron transport II. application to ion chamber response simulation. *Med. Phys.*, 27:499–513, 2000.

[67] Storm E and Israel H. Photon cross-sections from 1 KeV to 100 MeV for elements Z=1 to Z=100. *At. Data Nucl. Data Tables 7*, pages 365–681, 1970.

[68] Berger M J, Coursey J S, and Zucker M A. ESTAR, ASTAR and PSTAR: Computer programs for calculating stopping power and range tables for electrons, protons and helium ions (version 1.21). Technical report, NIST, 1999.

[69] Rogers D W O, Faddegon B A, Ding G X, Ma C M, Wei J, and Mackie T R. BEAM: A Monte Carlo code to simulate radiotherapy treatment units. *Med. Phys.*, 22:503–524, 1995.

[70] Walters B, Kawrakow I, and Rogers D W O. DOSXYZnrc users manual. PIRS 794revB, NRCC, 2004.

[71] Sheikh-Bagheri D, Rogers D W O, Ross C K, and Seuntjens J P. Comparison of measured and Monte Carlo calculated dose distributions from the NRC linac. *Med. Phys.*, 27:2256–2266, 2000.

[72] Lin S-Y, Chu T-C, and Lin J-P. Monte Carlo simulation of a clinical linear accelerator. *Appl. Radiat. Isot.*, 55:759–765, 2001.

[73] Patau J P, Vernes C E, Terriccol M, and Malbert M. Calcul des characteristiques qualitatives (tel, f.q., equivalent de dose) d'un faisceau de photons de freinage a usage medical, par simulation de sa creation et de son transport. *Proc. the 6th Symposium on Microdosimetry*, pages 579–588, 1978.

[74] Chaney E L, Culip T J, and Gabriel T A. A Monte Carlo study of accelerator head scatter. *Med. Phys.*, 21:1383–1390, 1994.

[75] Faddegon B A, O'Brien P, and Mason D L D. The flatness of Siemens linear accelerator x-ray field. *Med. Phys.*, 26:220–228, 1999.

[76] Lovelock D M J, Chui C S, Kutcher J, and Mohan R. Analysis of the photon beam treatment planning data for a scanning beam machine. *Med. Phys.*, 21:1969–1977, 1994.

[77] Siebers J V, Keall P J, Kim J O, and Mohan R. A method for photon beam Monte Carlo multileaf collimator particle transport. *Phys. Med. Biol.*, 47:3225–3249, 2002.

[78] Udale M. A Monte Carlo investigation of surface doses for broad electron beams. *Phys. Med. Biol.*, 33:939–954, 1988.

[79] Udale-Smith M. *A Monte Carlo investigation of high energy electron beams used in radiotherapy.* PhD thesis, Leeds University, 1990.

[80] Udale M. Monte Carlo calculations of electron beam parameters for three phillips linear accelerators. *Phys. Med. Biol.*, 37:85–105, 1992.

[81] Ma C-M, Rogers D W O, Faddegon B A, Ding G X, Wei J S, Bielajew A F, and Mackie T R. Simplified models of electron beams from a 2100C accelerator (abstract). *Med. Phys.*, 20:1295, 1993.

[82] Ma C-M, Rogers D W O, Ding G X, and Mackie T R. Electron beam characterization: reconstruction models and dose distributions in a homogeneous phantom (abstract). *Med. Phys.*, 21:895, 1994.

[83] Schreiber E C and Faddegon B A. Sensitivity of large-field electron beams to variations in a Monte Carlo accelerator model. *Phys. Med. Biol.*, 50:769–778, 2005.

[84] Huang V W, Seuntjens J, Devic S, and Verhaegen F. Experimental determination of electron source parameters for accurate Monte Carlo calculations of large field electron therapy. *Phys. Med. Biol.*, 50:779–786, 2005.

[85] Verhaegen F, Nahum A E, Van de Putte S, and Namito Y. Monte Carlo modeling of radiotherapy kV x-ray units. *Phys. Med. Biol.*, 44:1767–1789, 1999.

[86] Caon M, Bibbo G, and Pattison J. A comparison of radiation dose measured in CT dosimetry phantom with calculations using EGS4 and voxel-based models. *Phys. Med. Biol.*, 42:219–229, 1997.

[87] Caon M, Bibbo G, and Pattison J. An EGS4-ready tomographic computational model of a 14-year-old female torso for calculating organ doses from CT examinations. *Phys. Med. Biol.*, 44:2213–2225, 1999.

[88] Jarry G, DeMarco J J, Beifuss U, Cagnon C H, and McNitt-Gray M F. A Monte Carlo-based method to estimate radiation dose from spiral CT: from phantom testing to patient-specific models. *Phys. Med. Biol.*, 48:2645–2663, 2003.

[89] Reza Ay M and Zaidi H. Development and validation of MCNP4C-based Monte Carlo simulator for fan- and cone-beam x-ray CT. *Phys. Med. Biol.*, 50:4863–4885, 2005.

[90] Bazalova M, Palefsky S, Beaulieu L, and Verhaegen F. Correction of streaking artifacts in CT images and its influence on Monte Carlo dose calculations. *Med. Phys.*, 33:2158, 2006.

[91] Kalender W. Monte Carlo calculations of x-ray scatter data for diagnostic radiology. *Phys. Med. Biol.*, 26:835–849, 1981.

[92] Chan H P and Doi K. Physical characteristics of scattered radiation in diagnostic radiology: Monte Carlo simulation studies. *Med. Phys.*, 12:152–165, 1984.

[93] Malusek A, Sandborg M, and Carlsson G A. Simulation of scatter in cone beam CT- effect on projection image quality. *Proc. SPIE*, 5030:740–751, 2003.

[94] Hartmann-Siantar C L, Bergstrom P M, and Chandler W P. Lawrence livermore national laboratory's PEREGRINE project. In *Proc. 12th ICCR*, Salt Lake City, Utah, 1997.

[95] DeMarco J J, Solberg T D, and Smathers J B. A CT-based Monte Carlo simulation tool for dosimetry planning and analysis. *Med. Phys.*, 25:1–11, 1998.

[96] Kapur A, Ma C-M, Mok E, Findley D, and Boyer A L. Monte Carlo calculations of clinical electron beam output factors. *Phys. Med. Biol.*, 43:3479–3494, 1998.

[97] Faddegon B A, Balogh J, Mackenzie R, and Scora D. Clinical considerations of Monte Carlo for electron radiotherapy treatment planning. *Radiat. Phys. Chem.*, 35:217–228, 1998.

[98] Wang L, Chui C, and Lovelock M. A patient-specific Monte Carlo dose-calculation method for photon beams. *Med. Phys.*, 25:867–978, 1998.

[99] Ma C-M, Mok E, Kapur A, Findley D, Brain S, Forster K, and Boyer A L. Clinical implementation of a Monte Carlo treatment planning system. *Med. Phys.*, 26:2133–2143, 1999.

[100] Ma C-M, Pawlicki T, Jiang S B, Mok E, Kapur A, Xing L, Ma L, and Boyer A L. Monte Carlo verification of IMRT dose distributions from a commercial treatment planning optimization system. *Phys. Med. Biol.*, 45:2483–2495, 2000.

[101] Kawrakow I, Fippel M, and Friedrich K. 3D electron dose calculation using a voxel based Monte Carlo algorithm. *Med. Phys.*, 23:445–457, 1996.

[102] Sempau J, Wilderman S J, and Bielajew A F. DPM, a fast, accurate Monte Carlo code optimized for photon and electron radiotherapy treatment planning dose calculations. *Phys. Med. Biol.*, 45:2263–91, 2000.

[103] Verhaegen F and Devic S. Sensitivity study for CT image use in Monte Carlo treatment planning. *Phys. Med. Biol.*, 50:937–946, 2005.

[104] Swindell W and Evans P M. Scattered radiation in portal images: a Monte Carlo simulation and a simple physical model. *Med. Phys.*, 23:63–73, 1996.

[105] Kim J O Ko L and Siebers J V. Investigation of the optimal backscatter for an aSi electronic portal imaging device. *Phys. Med. Biol.*, 49:1723–1738, 2004.

[106] Bissonnette J-P, Cunningham I A, Jaffray DA, Fenster A, and Munro P. A quantum accounting and detective quantum efficiency analysis for video-based portal imaging. *Med. Phys.*, 24:815–826, 1997.

[107] Bissonnette J-P, Cunningham I A, and Munro P. Optimal phosphor thickness for portal imaging. *Med. Phys.*, 24:803–814, 1997.

[108] Lachaine M, Fallone B G, and Falco T. Monte Carlo detective quantum efficiency and scatter studies of a metal/a-Se portal detector. *Med. Phys.*, 25:1186–1194, 1998.

[109] Kausch C, Cremers F, Albers D, Schmidt R, and Screibert B. Monte Carlo simulation of a prototype photodetector used in radiotherapy. *Nucl. Instr. Meth.*, 442:53–57, 2000.

[110] Boone J M, Seibert J A, Sabol J M, and Tecotzky M. A Monte Carlo study of x-ray fluorescence in x-ray detectors. *Med. Phys.*, 26:905–916, 1999.

[111] Thacker S C, Glick S J, and Badano A. Monte Carlo simulation of a CsI-based flat-panel imager for mammography. *Proc. SPIE*, 5368:411–419, 2004.

CHAPTER 3
Monte Carlo Models

3.1 Introduction

In radiation therapy Monte Carlo (MC) simulations are more and more frequently used to (re)calculate treatment plans in order to establish the absorbed dose received by the patients. Throughout this thesis MC simulations are used to develop and validate the new treatment verification methods presented. MC simulations are used to obtain predicted portal images, to obtain predicted cone beam computed tomography (CBCT) projections and to calculate the dose received by phantoms and patients using portal images.

Extensive work has been performed to validate MC models of linear accelerators (linacs) in both photon and electron mode (see section 2.4.2). In order to obtain accurate MC results, every linac type must be modeled according to its own specifications. Moreover, linacs of the same type may differ in nominal energy or in focal spot size. Therefore, every linac model must be carefully tuned to match measurements.

In this section, the MC model used for the Varian CL21EX linac at the Montreal General Hospital (MGH) is presented and validated for both the photon and electron configuration. This linac is equipped with an aSi EPID which was also modeled using MC simulations. An analytical program based on the detector dose response was developed to replace the full MC simulation of the detector and hence reduce

the simulation time. The MC model of the kV cone beam CT unit is not presented in this chapter since a detailed description can be found in chapter 7.

3.2 Materials and Methods

3.2.1 Linear Accelerator in Photon Configuration

EGSnrc Model. The BEAMnrc package, which is part of the EGSnrc MC code [1], was used to develop a model of the Varian CL21EX linac in the photon configuration mode for the 6 MV beam according to manufacturer's data. Figure 3–1(a) shows a detailed schematic of the different linac components that were modeled as well as the component modules that were used. This model includes the tungsten target, the primary collimator, the vacuum exit window, the flattening filter, a simplified model of the ion chamber, the mirror and the jaws. A parallel circular electron beam (radius of 0.1 cm) incident on the target with an energy of 6 MeV was chosen to match simulated depth dose and off-axis profiles with measured data. Photon and electron total energy cutoff, PCUT and ECUT, of 0.01 MeV and 0.700 MeV were used respectively. To improve the calculation efficiency, bremsstrahlung splitting [1] with a photon split factor of 20 was used in the target. Phase space files were scored right after the jaws, at a distance of 47 cm from the front face of the target. The number of incident particles was set to obtain a particle density of 2×10^5 particles/cm^2 in the phase space files.

The transport of the particles through the multileaf collimator (MLC) was implemented in two different ways: 1) using a full BEAMnrc MC model of the Varian Millennium 120 leaf collimator developed by Heath and Seuntjens [2] and (2) using the analytical program developed by Siebers *et al* [3] described in section 2.4.2. The

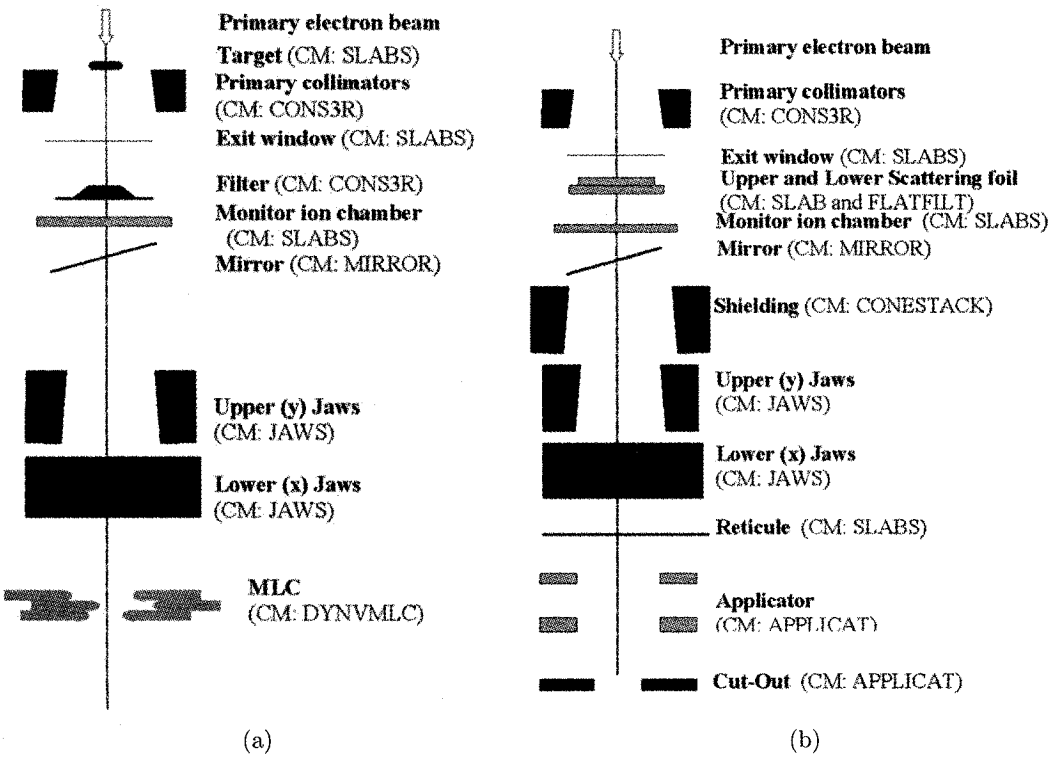

Figure 3–1: Schematic drawing of linac components (a) photon beam configuration and (b) electron beam configuration.

full MC model includes details such as the leaf driving screw hole, support railing groove and leaf tips. Further modifications also allow sampling of leaf sequence files to simulate the movement of the MLC leaves during an intensity modulated radiation therapy (IMRT) delivery. This modeling technique had already been implemented by Liu *et al* [4].

Model Validation. Simulated and measured in-air profiles for a (40×40) cm^2 field size as well as percent depth dose (PDD) and profiles in water for a (10×10) cm^2 open field were compared to validate the MC model. The in-air measurements were acquired with a Farmer type ionization chamber inserted in a 0.5 cm thick aluminum buildup cap. The water measurements were performed in a water tank with an IC10 (Scanditronix-Wellhofer) cylindrical ion chamber. The simulations were performed under the same conditions as the measurements using the DOSXYZnrc program [5] which is part of the EGSnrc package. The resolution of the simulated air voxels was set to $(0.5 \times 0.5 \times 0.5)$ cm^3 while the resolution of the simulated water voxels was set to $(0.25 \times 0.25 \times 0.4)$ cm^3. The particles were not recycled for the in-air simulations yielding a statistical uncertainty inferior to 1% of the dose maximum. For the in-water simulations, the particles were recycled 8 times to yield a statistical uncertainty inferior to 1% in the high dose region and inferior to 6% in the penumbra region. Measured output factors obtained using the IC10 ionization chamber were compared to simulations. The measurements were performed in solid water with 14 cm of backscatter material and 1.5 cm of buildup material. The simulations mimicked the measurements; however the ion chamber was not modeled.

The modeling of the MLC was evaluated using EDR2 film measurements of IMRT fields and comparing them against simulated dose distribution obtained using the two MLC modeling methods. Three IMRT fields are presented: (1) a pyramid IMRT field which consists in concentric squares of different intensity, (2) a clinical IMRT field for a colorectal treatment at gantry angle of 40 degree, and (3) at gantry angle of 180 degree. The three fields were delivered with a 6 MV beam. Kodak EDR2 films were used for the dose measurements; this type of film has been shown to be adequate for the dosimetry of IMRT fields [6]. For uniform fields, EDR2 films provide good accuracy at the center of the field [7] but overestimate the dose outside the field due to their over response to low energies [8, 9]. The films were inserted between two slabs of solid water providing 6 cm of buildup material and 11 cm of backscatter material. Films were developed with a Kodak RPX-Omat processor and digitized using an ArgusII AGFA scanner with 16 bit depth and 127 dpi resolution, resulting in 0.2 mm pixel size. The simulated dose in water was compared to the film measurements. The simulated voxel size was set to $(0.1 \times 0.1 \times 0.5)$ cm^3, this ensured a good resolution and minimized the noise. Before comparison of film and simulations the digitized film data was re-binned to obtain pixel sizes corresponding to the MC simulation. The measured and simulated doses were normalized to the dose maximum because the film doses were considered to be relative doses. A gamma index map was obtained to compare measurements and simulations. In this method, introduced by Low *et al* [10], the measure of acceptability is the multidimensional distance between the measured and simulated points in both the dose and the physical distance. Given that the measured and the simulated doses fall within a specified

distance and percent difference criteria then the gamma index is inferior to one, otherwise it is superior to one. This comparison method is particularly interesting in high dose gradient regions where a small difference in position can lead to a huge dose difference. To date, no uniform guidelines regarding the definition of tolerance criteria for quantitative evaluations in IMRT quality assurance can be found in the literature. Van Dyk *et al* [11] propose 4 mm, 3% for static photon fields. Low and Dempsey [12] suggest 5% and 3 mm for clinical IMRT fields, they also specify that the pixel spacing should be less that or equal to 1/3 of the distance criterion. For the film to MC dose comparison, the latter were chosen as distance and error criteria.

3.2.2 Linear Accelerator in Electron Configuration

The BEAMnrc MC code system [1] was used to build a linear accelerator model of the Varian CL21EX linac in electron mode according to the manufacturer's specifications. A schematic diagram of the accelerator model is shown in figure 3–1(b). The model includes the exit window, the scattering foils, the monitor chamber, the jaws, the applicator, and the cut-out. A (20 × 20) cm^2 and a (10 × 10) cm^2 electron applicators as well as a (20 × 20) cm^2, a (10 × 10) cm^2 and a (5 × 5) cm^2 cut-outs were modeled. Four electron beam energies (6, 9, 12 and 16 MeV) were modeled with corresponding scattering foils. The primary electron beam energy (figure 3–1(b)) was modeled as being a mono-energetic [13] divergent cone as suggested by Huang *et al* [14] who showed that the focal spot of electron beams in our Varian CL21 EX linac is elliptical and has a Gaussian spatial distribution. The electron creation and transport thresholds, AE and ECUT, were both set to 0.521 MeV. For bremsstrahlung creation and photon transport, the thresholds AP and PCUT were

set to 0.01 MeV. The electron transport algorithm PRESTA II was selected with its default parameters as well as EXACT boundary crossing. Phase space files were obtained just below the electron cut-out. The phase space file sizes varied from 125 000 particles/cm^2 for the 6 MeV beam to 350 000 particles/cm^2 for the 16 MeV beam.

Model Validation. In order to tune the primary electron beam energy, simulated and measured PDDs were compared. The PDDs were measured using a Scanditronix p-type Si diode field detector in a water tank. Particle transport in a ($20 \times 20 \times 30$) cm^3 water phantom with ($0.2 \times 1.0 \times 0.2$) cm^3 voxels was simulated using the DOSXYZnrc code [5]; particles were recycled twice. The simulated primary electron beam energy was varied until the difference between the measured and simulated R_{50} and R_p (electron practical range) were within 0.5 mm and 1 mm respectively. The statistical uncertainty on the simulation was less than 0.5% at R_{50}. Further validation of the model consisted in comparing measured and simulated off axis profiles in water; three depths were considered (R_{max}, R_{50} and R_p) for all energies.

3.2.3 Amorphous Silicon Portal Imager Model

EGSnrc Model. A complete MC model of the aS500 EPID was built according to the manufacturer's specifications using the DOSXYZnrc program. The model includes the protective cover, the copper buildup layer, the phosphor layer and sufficient backscattering material. The backscatter produced by the detector mounting was simulated by adding solid water behind the phosphor layer. The thickness of solid water was evaluated using the technique described by Siebers *et al* [15]. A schematic of the portal imager model can be found in figure 3–2. A detailed schematic is not

provided due to a non disclosure agreement with the manufacturer. Since the response of the light detector (aSi photodiode) can be approximated to be proportional to the energy deposition in the phosphor (gadolinium oxisulfide, Gd_2O_2S) [16, 17], simulated images can be obtained by scoring the dose in the gadolinium oxisulfide layer of the detector. The MC dose can be transformed to EPID signal by using the following pixel-by-pixel calibration method:

$$I_{\mathrm{MC}}(i,j) = D_{\mathrm{MC}}(i,j) \times \frac{FF(i,j)}{FF_{\mathrm{MC}}(i,j)} \tag{3.1}$$

where $I_{\mathrm{MC}}(i,j)$ is the MC EPID signal for pixel i,j, $D_{\mathrm{MC}}(i,j)$ is the MC dose scored in the active layer of the detector, $FF(i,j)$ is a measured flood field and $FF_{\mathrm{MC}}(i,j)$ is the MC dose scored in the active layer for the flood field set-up. Similarly, the EPID image can be transformed to dose by inverting equation 3.1.

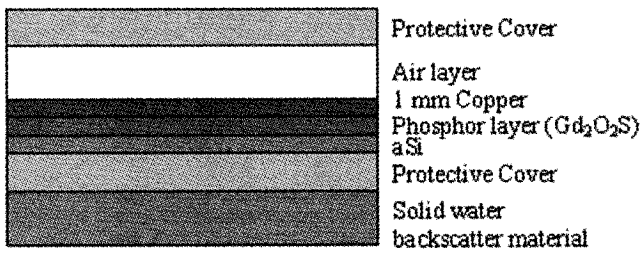

Figure 3–2: Schematic drawing of the aS500 portal imager main components.

Analytical Program. The MC model of the portal imager was used to obtain a dose versus energy curve, shown in figure 3–3. Parallel monoenergetic beams incident on the portal imager were simulated to determine the portal imager response to different energies. This response curve is used as the basis for an analytical

program which calculates the dose in the active layer of the portal imager. The analytical program reads a phase space file scored at the active layer position to obtain the position, direction, weight and energy of the particles. The dose response curve is used to obtain the dose to the active layer for a given particle energy. The dose is then scaled with the particle path length in the phosphor layer pixel, taking the incident direction into account. Although particles can travel through more than one pixel and hence deposit their dose in more than one pixel, the approximation that they deposit all their dose at the entrance pixel introduces an error of 0.15% or less for typical patient sizes and composition.

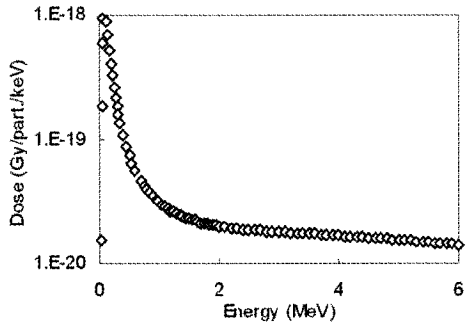

Figure 3–3: MC simulation of the dose response as a function of the beam energy for the Varian aS500 EPID.

Model Validation. Both the full MC model and the analytical program were validated against measurements. A 6 MV beam with 400 MU/min nominal dose rate was used. The images were integrated over 10 frames and each measurement was repeated three times to obtain an uncertainty inferior to 0.5%. The particles, stored in the phase space file scored after the linac jaws, were recycled 4 times to be transported through the flat-panel MC model. The detector pixel size was increased

by a factor two to ensure a statistical uncertainty inferior to 1%. The analytical model used the same phase space file, no recycling was used but the detector pixel size was also increased by a factor two. The statistical uncertainty on the active layer dose was in this case inferior to 2%, since four time less particles were used to create the image. The simulated dose was transformed to EPID signal using equation 3.1. The measured and simulated detector response to different source-to-detector distances (SDDs) and to different field sizes was evaluated. Measurement and simulation of the detector response when different thicknesses of solid water are placed in the beam were also compared. Measured and simulated portal images of IMRT fields were compared using a gamma index map with 5 mm, 5% criterion. The distance criterion was set to 5 mm to respect the 3× pixel size constraint. The IMRT fields described in section 3.2.1 were used.

3.3 Results and Discussion

3.3.1 Validation of Linac in Photon Configuration

Figure 3–4(a) shows the PDD in water for a (10 × 10) cm^2, 6 MV beam. Measurements and simulations agree within 2% except in the buildup region where the agreement is within 5%; similar agreement was obtained for a (5 × 5) cm^2 and a (20 × 20) cm^2 field. The agreement between the PDDs is an indication that the initial energy of the electron hitting the accelerator target is modeled properly. It also demonstrates that the other linac components provide the right amount of beam filtration. Figure 3–5(a) shows the simulated and measured dose profile at 1.5 cm depth in water for a (10 × 10) cm^2 field; the normalized doses are within 2% or 2 mm. Figure 3–5 shows the measured and simulated in air profile for a (40 × 40) cm^2 field

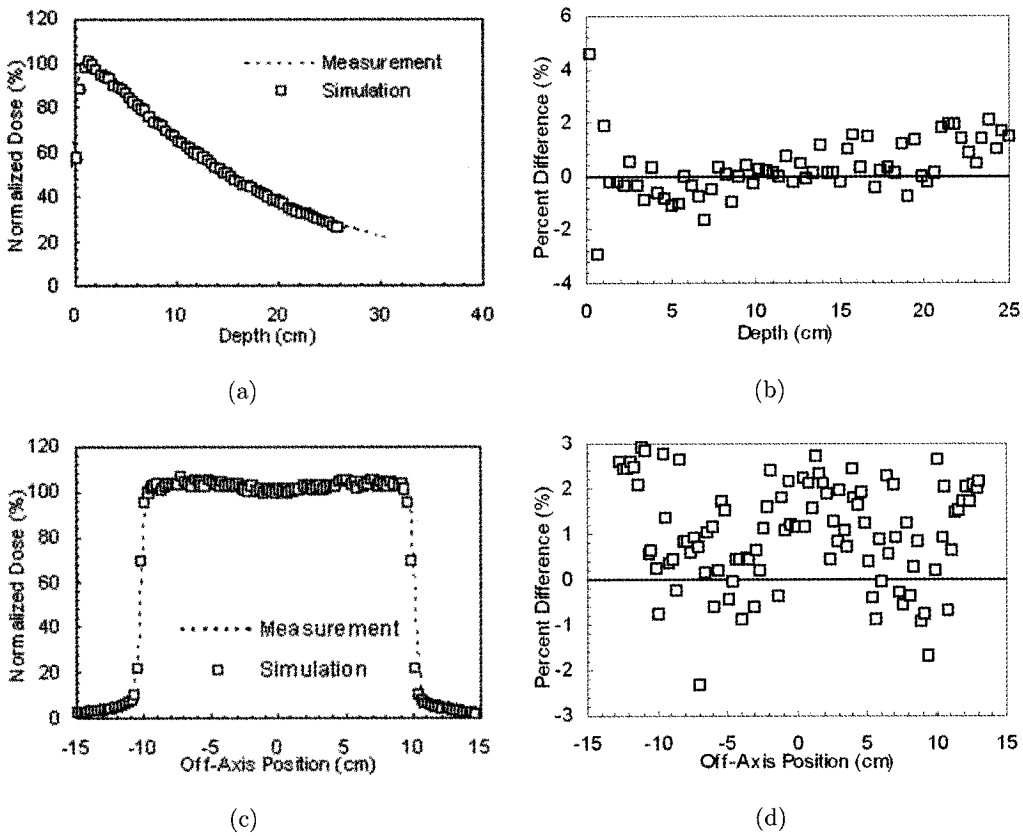

Figure 3–4: Simulated and measured (a) central axis percent depth dose (PDD) (c) profile (1.5 cm depth) in water for a (10 × 10) cm^2 open field, 6 MV beam and (b) (d) the respective percent difference.

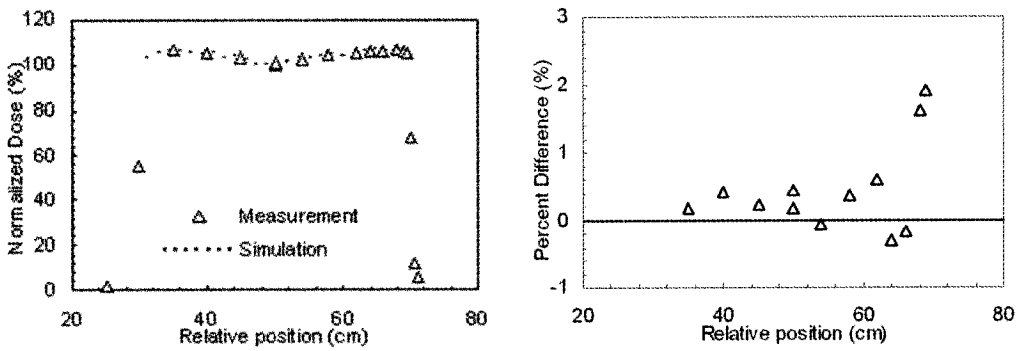

(a) (b)

Figure 3–5: (a) Simulated and measured normalized dose in-air profile for a (40×40) cm^2 open field, 6 MV beam at 100 cm from the source and (b) the percent difference.

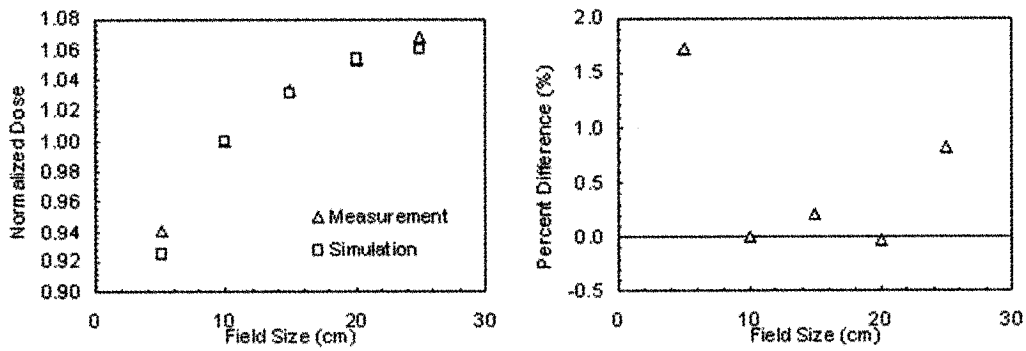

(a) (b)

Figure 3–6: (a) Simulated and measured output factor in solid water at a 1.5 cm depth for a 6 MV beam; (b) percent difference between simulated and measured values.

at 100 cm from the source. The measured and simulated normalized doses agree within 2%. Because of their high statistical uncertainty, the simulated doses in the penumbra region of the air profile are not reported. Sheikh-Bagheri and Rogers [18] suggested that in-air profiles are more sensitive to the initital electron beam parameters since they are not significantly affected by scattered radiation. The agreement between the profiles both in-air and in water, especially for the large field size, demonstrates that the initial electron beam radius was tuned properly. Figure 3–6 shows the measured and simulated output factors; an agreement within 2% is obtained.

Figures 3–7 to 3–10 show the normalized dose distribution from film measurement and from MC simulations. The gamma index maps used for the comparison of the three IMRT fields are also found in these figures. Figure 3–7 and 3–8 respectively show the dose obtained using the full MLC simulations and the analytical program developed by Siebers *et al* [3]. Both techniques generate similar dose maps; however the complete MLC simulation takes at least two times longer to run than the analytical program. In the case of the colorectal IMRT field the analytical program ran for 18 hours on a pentium 4 Xeon processor 2.8 GHz to produce 2 millions particles in the phase space file; this included the BEAMnrc simulation time to produce the phase space file above the MLC. On the other hand, the complete BEAMnrc MLC simulation ran for 40 hours to obtain the same phase space file. The simulation time for the complete MLC model can be reduced by almost a factor two if the electron transport is turned off. For the case of the pyramid IMRT field (using both MLC simulation techniques), the gamma index is inferior to 1 for 96% of the pixels that are directly exposed to radiation; this means that those pixels satisfy the 5%,

3 mm criterion. For both the colorectal IMRT fields the gamma index is inferior to 1 for 92% of the pixels directly exposed to the radiation. The discrepancies between measured and simulated pixel values can be due to the dead time error in the measurements as explained in section 4.3.5. For pixels outside of the field, and past the penumbra region, the gamma index is superior to 1, this is most likely due to the large statistical uncertainty on the MC calculations in these low dose regions. The statistical uncertainty on the MC simulations is below 3% except outside of the irradiated region where it is inferior to 30%. We can conclude that the MC model can predict accurately the dose distribution produced by IMRT fields.

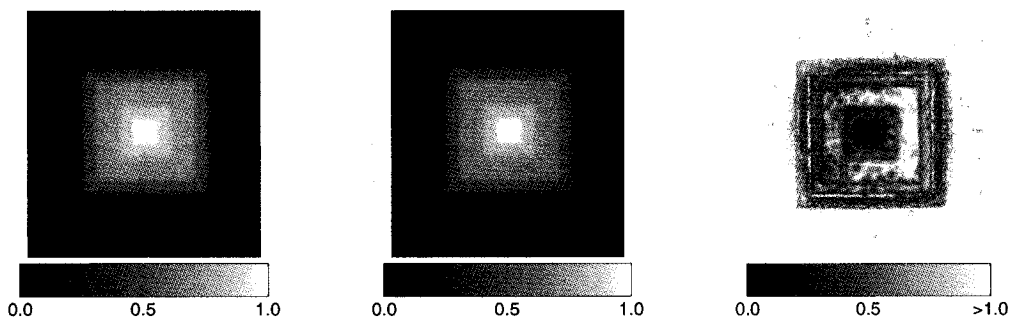

Figure 3–7: Relative dose distribution from (a) film measurements and (b) MC calculations using the full MLC model [2] to simulate the MLC for a pyramid IMRT field with gantry at 0^o and (c) gamma index map with 3 mm, 5% criterion.

3.3.2 Validation of Linac in Electron Configuration

Simulated and measured PDD for the four electron beam energies and a (20×20) cm^2 field can be found in figure 3–11. The R_{50} and R_p (electron practical range) are within 0.5 mm and 1 mm respectively; the same agreement was obtained for

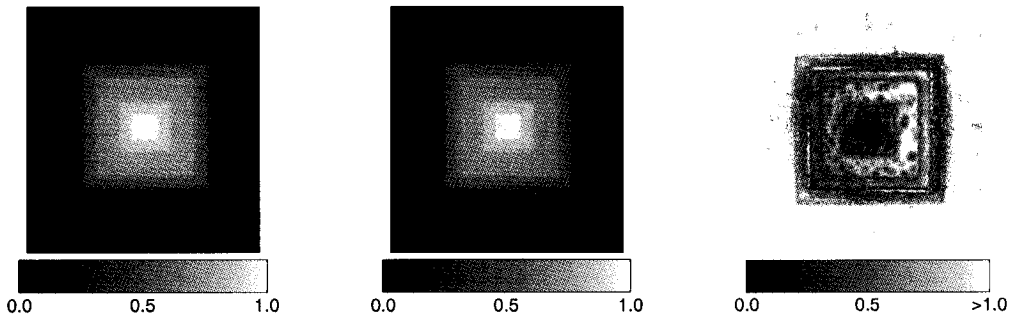

(a) (b) (c)

Figure 3–8: Relative dose distribution from (a) film measurements and (b) MC calculations using the Siebers *et al* analytical program [3] to simulate the MLC for a pyramid IMRT field with gantry at 0^o and (c) gamma index map with 3 mm, 5% criterion.

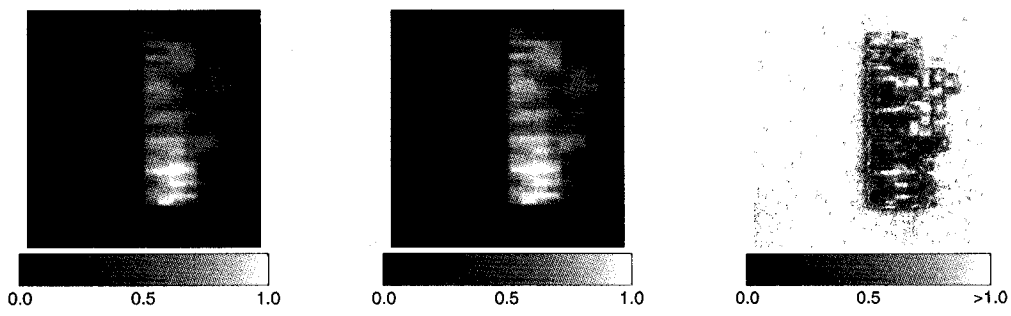

(a) (b) (c)

Figure 3–9: Relative dose distribution from (a) film measurements and (b) MC calculations for a colorectal IMRT field with gantry at 180^o and (c) gamma index map with 3 mm, 5% criterion.

(5 × 5) cm^2 and (10 × 10) cm^2 fields. The agreement between measured and simulated R_{50} and R_p indicates that the primary electron energy is modeled properly. The measured and simulated PDDs agree within 2% except in the buildup region for the 6 MeV beam where the agreement is within 3%. Figure 3–12 shows profiles at different depths for the four simulated energies and a (20 × 20) cm^2 field size. Agreement within 3% or 3 mm is obtained for the R_{max} and R_{50} depth. An agreement whithin 10% is obtained for the R_p depth where the statistical uncertainty on the measurements and the simulation is higher since few particles reach this depth. Similar agreement was obtained for the other field sizes.

3.3.3 Portal Imager Model Validation

The simulated and measured EPID responses with field size variation for a 140 cm SDD are shown in figure 3–13. The simulation values are obtained using the full detector model and the analytical program. Agreement within 3.5% and 2.5% is obtained for all field sizes for the EGSnrc simulation and the analytical

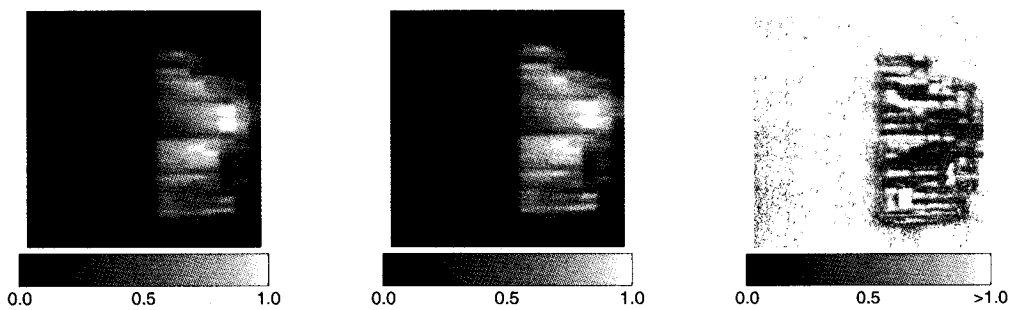

Figure 3–10: Relative dose distribution from (a) film measurements and (b) MC calculations for a colorectal IMRT field with gantry at 40° and (c) gamma index map with 3 mm, 5% criterion.

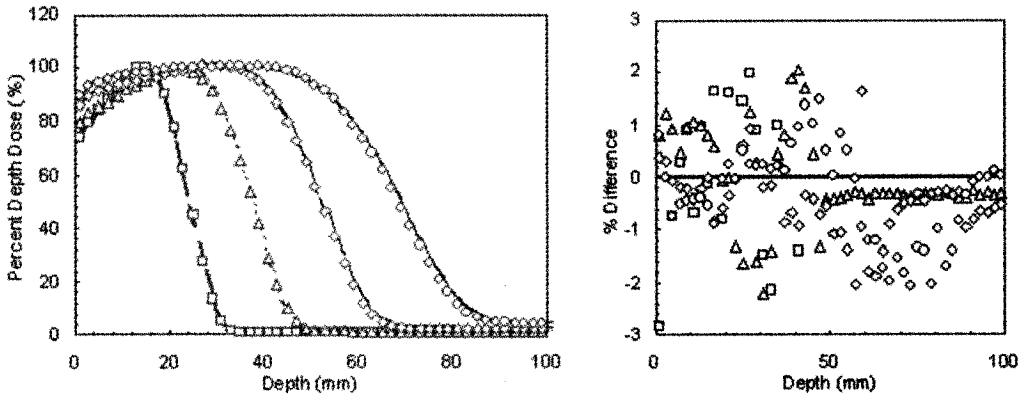

(a) (b)

Figure 3–11: (a) Simulated and measured PDD curves in water for a 6 (□), 9 (△), 12 (◇), and 16 (○) MeV beam for a (20 × 20) cm^2 open field and (b) the percent difference between simulation and measurement.

program, respectively, as shown in figure 3–13(b). Figure 3–14 shows the agreement between measurement and simulation when different thicknesses of solid water are attenuating the beam for a (10 × 10) cm^2 field size and a 140 cm SDD. An agreement within 4.5% is obtained for both the full MC simulation and the analytical program. Figure 3–15 shows the detector response to different SDDs for a (10 × 10) cm^2 field. Measurement and simulation agree within 4.0%. The full MC detector model and the analytical program are able to model correctly field size and SDD response as well as variation in detector response with attenuating material.

Figures 3–16 to 3–19 show simulated and measured portal images for three IMRT fields. The portal images for the pyramid IMRT field obtained with the full detector model and with the analytical program are shown in figures 3–16 and 3–17 respectively. The gamma index is found to be inferior to 1 for 90% of the pixels

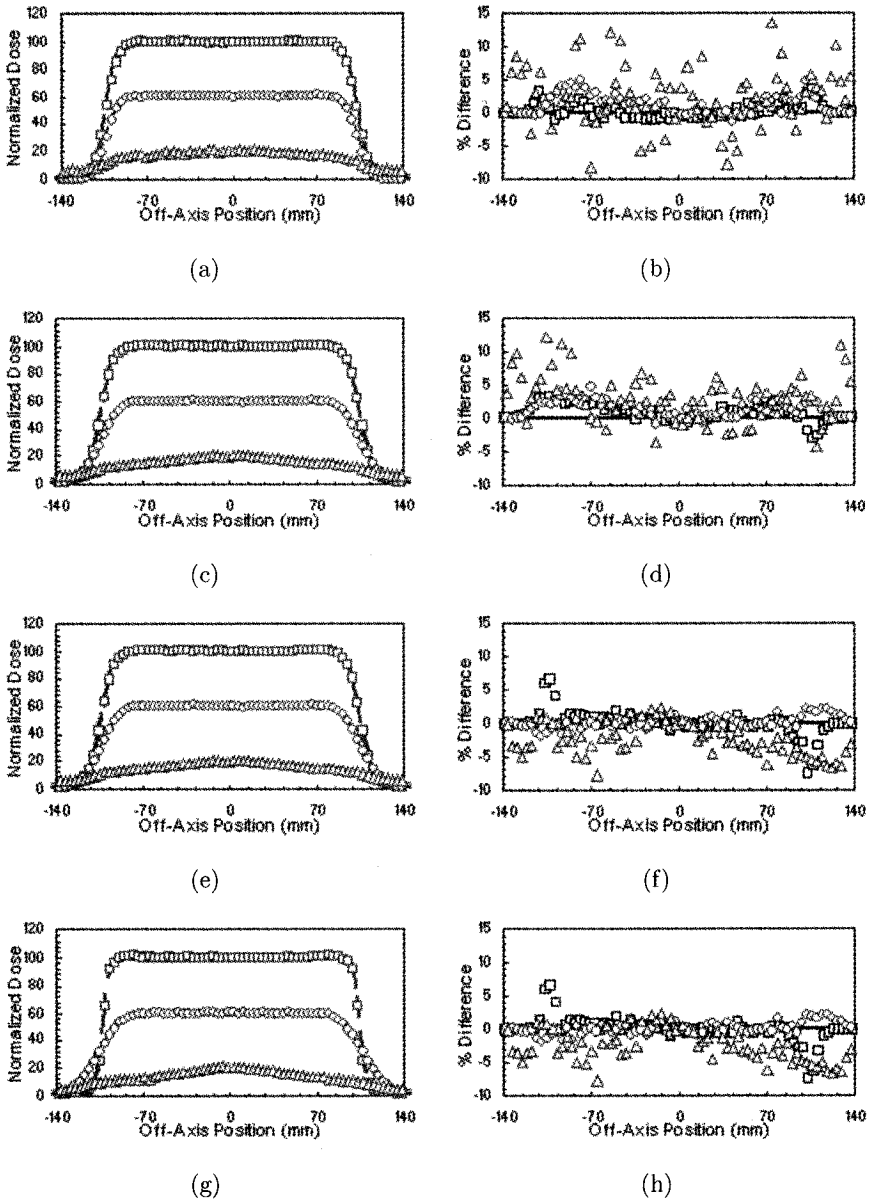

Figure 3–12: Simulated and measured off-axis profiles in water for a (a) 6, (c) 9, (e) 12, and (g) 16 MeV beam at R_{max} (□), R_{50} (○), and R_p (△) for a (20 × 20) cm^2 open field and the corresponding percent difference. The normalization factor does not reflect the dose ratio between the different depths and has been arbitrarily assigned to make the graph clearer.

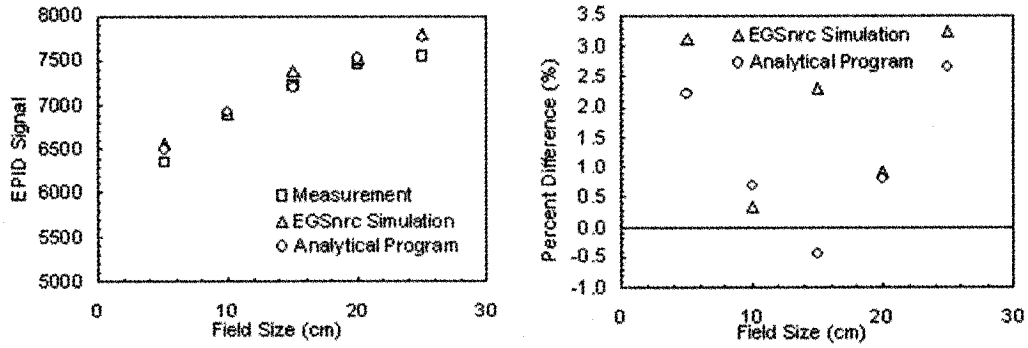

(a) (b)

Figure 3–13: (a) Comparison of field size response obtained with the detector, the EGSnrc simulation, and the analytical program, looking at the average detector signal in a (12 × 12) pixel^2 region of interest, for a 105 cm source-to-detector distance (SDD) and a 6 MV photon beam. (b) Local percent difference obtained between measurement and EGSnrc simulation and between measurement and analytical program value.

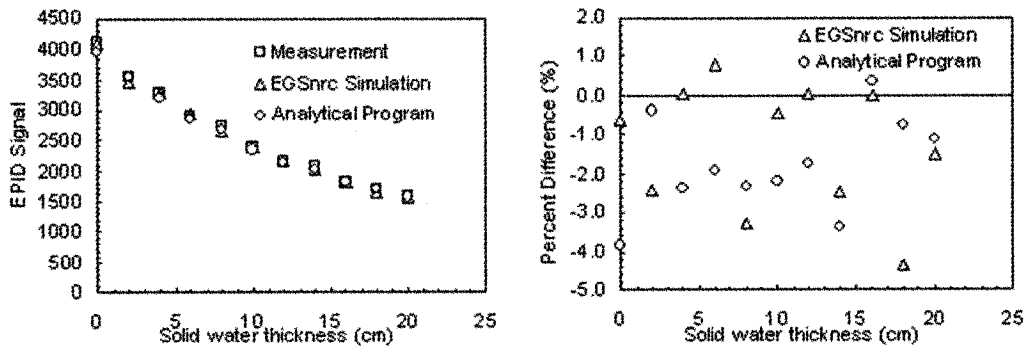

(a) (b)

Figure 3–14: (a) Comparison of detector response to solid water thickness for measurement, EGSnrc simulation and analytical program, looking at the average detector signal in a (12 × 12) pixel^2 region of interest, for a (10 × 10) cm^2 field size, 140 cm source-to-detector response and a 6 MV photon beam. (b) Local percent difference obtained between measurement and EGSnrc simulation and between measurement and analytical program value.

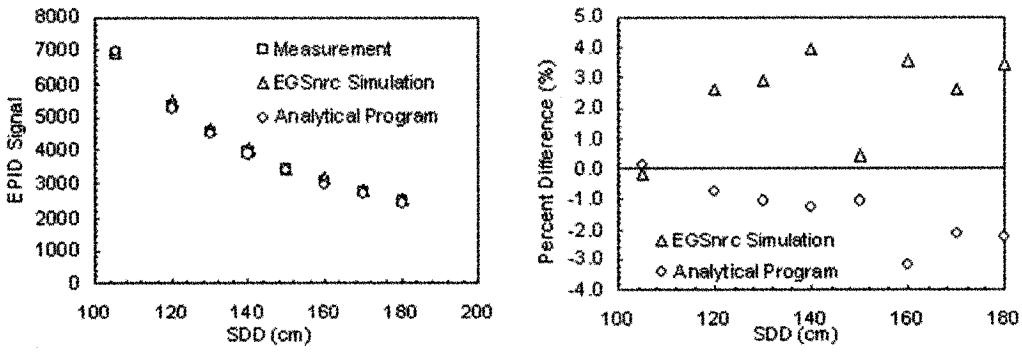

(a) (b)

Figure 3–15: (a) Comparison of source-to-detector response obtained with detector, EGSnrc simulation and analytical program, looking at the average detector signal in a (12 × 12) pixel^2 region of interest, for a (10 × 10) cm^2 field size and a 6 MV photon beam. (b) Local percent difference obtained between measurement and EGSnrc simulation and between measurement and analytical program value.

directly exposed to the radiation. The analytical program yields slightly better agreement for pixels outside the radiation field. The clinical colorectal IMRT fields yield a gamma index inderior to 1 for 95% of the pixels directly exposed. In all cases the 5 mm, 5% criterion was used. We conclude that both the full MC detector simulation and the analytical program are capable of predicting accurately portal images of IMRT fields.

3.4 Conclusion

A complete model of the Varian CL21EX linear accelerator including the aS500 portal imager was developed. The model includes the photon and the electron mode. The MLC leaves have been simulated using the BEAMnrc code and an analytical program; both techniques yielded similar results and good agreement with measurements. The simulations also includes a full and analytical model of the portal imager,

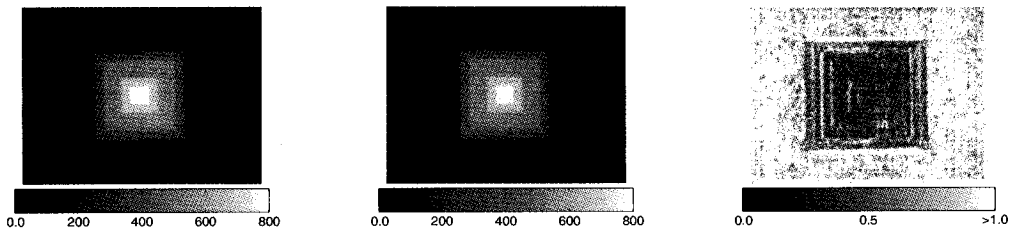

(a) (b) (c)

Figure 3–16: EPID image for a pyramid IMRT field with gantry at 0^o from (a) measurements using the Varian CL21EX and (b) MC calculations using the full MC simulation to produce the portal image and (c) gamma index map with 5 mm, 5% criterion.

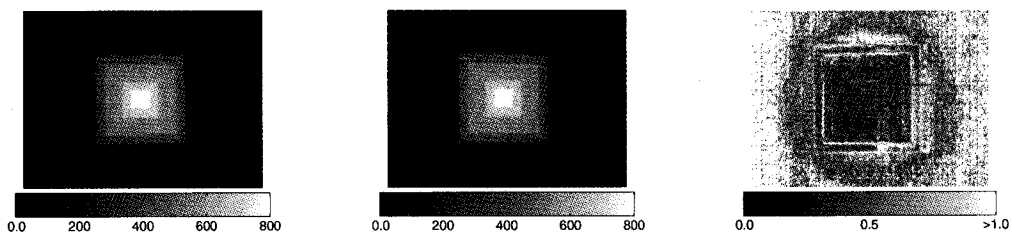

(a) (b) (c)

Figure 3–17: EPID image for a pyramid IMRT field with gantry at 0^o from (a) measurements using the Varian CL21EX and (b) MC calculations using the analytical program to produce the portal image and (c) gamma index map with 5 mm, 5% criterion.

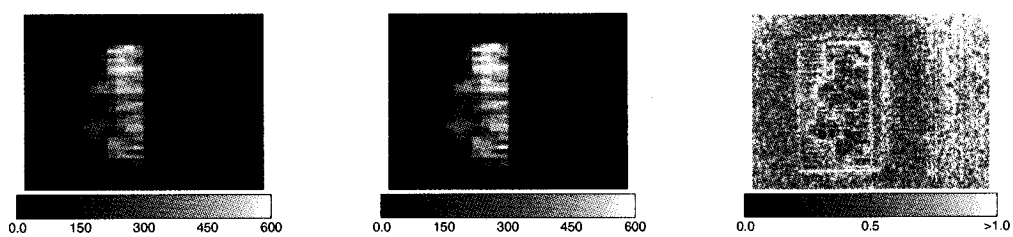

(a) (b) (c)

Figure 3–18: EPID image for a colorectal IMRT field with gantry at 180^o from (a) measurements using the Varian CL21EX and (b) MC calculations using the analytical program to produce the portal image and (c) gamma index map with 5 mm, 5% criterion.

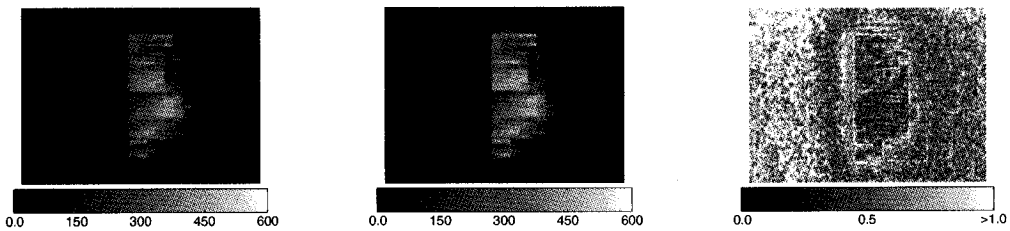

(a) (b) (c)

Figure 3–19: EPID image for a colorectal IMRT field with gantry at 40° from (a) measurements using the Varian CL21EX and (b) MC calculations using the analytical program to produce the portal image and (c) gamma index map with 5 mm, 5% criterion.

which were shown to both agree with measured portal images. The MC model can now be used to develop, test and validate the treatment verification techniques that will be presented in the next chapters.

References

[1] Rogers D W O, Faddegon B A, Ding G X, Ma C M, Wei J, and Mackie T R. BEAM: A Monte Carlo code to simulate radiotherapy treatment units. *Med. Phys.*, 22:503–524, 1995.

[2] Heath E and Seuntjens J. Development and validation of a BEAMnrc component module for accurate Monte Carlo modeling of the Varian dynamic Millenium multileaf collimator. *Phys. Med. Biol.*, 48:4045–4063, 2003.

[3] Siebers J V, Keall P J, Kim J O, and Mohan R. A method for photon beam Monte Carlo multileaf collimator particle transport. *Phys. Med. Biol.*, 47:3225–3249, 2002.

[4] Liu H H, Verhaegen F, and Dong L. A method of simulating dynamic multileaf collimators using Monte Carlo techniques for intensity modulated radiation therapy. *Phys. Med. Biol.*, 46:2283–2298, 2001.

[5] Walters B, Kawrakow I, and Rogers D W O. DOSXYZnrc users manual. PIRS 794revB, NRCC, 2004.

[6] Winkler P, Zurl B, Guss H, Kindl P, and Stuecklschweiger G. Performance analysis of a film dosimetric quality assurance procedure for IMRT with regard to the employment of quantitative evaluation methods. *Phys. Med. Biol.*, 50:643–654, 2005.

[7] Zhu X R, Jursinic P A, Grimm D F, Lopez F, Rownd J J, and Gillin M T. Evaluation of Kodak EDR2 film for dose verification of intensity modulated radiation therapy by a static multileaf collimator. *Med. Phys.*, 29:1687–1692, 2002.

[8] Palm A, Kiror A S, and LaSasso T. Predicting energy response of radiographic film in a 6 mv x-ray beam using mc calculated fluence spectra absorbed dose. *Med. Phys.*, 31:3168–3178, 2004.

[9] Yeo I J, Beiki-Ardakani A, Cho y, Heydariam M, zhang T, and Islam M. EDR2 film dosimetry for imrt verification using low-energy photon filters. *Med. Phys.*, 31:1960–1963, 2004.

[10] Low D A, Harms W B, Mutic, and Purdy J A. A technique for the quantitative evaluation of dose distribution. *Med. Phys.*, 25:656–661, 1998.

[11] Van Dyk J, Barnett R B, Cygler J E, and Shragge P C. Commissioning and quality assurance of treatment planning computers. *Int. J. Radiat. Oncol. Biol. Phys.*, 26:261–273, 1993.

[12] Low D A and Dempsey J F. Evaluation of the gamma dose distribution comparison method. *Med. Phys.*, 30:2455–2464, 2003.

[13] Verhaegen F, Mubata C, Pettingell J, Bidmead M, Rosenberg I, Mockridge D, and Nahum A E. Monte Carlo calculation of output factors for circular, rectangular, and square fields of electron accelerators (6-20 MeV). *Med. Phys.*, 44:938–949, 2001.

[14] Huang V W, Seuntjens J, Devic S, and Verhaegen F. Experimental determination of electron source parameters for accurate Monte Carlo calculations of large field electron therapy. *Phys. Med. Biol.*, 50:779–786, 2005.

[15] Siebers J V, Kim J O, Ko L, Keall P J, and Mohan R. Monte Carlo computation of dosimetric amorphous silicon electronic portal images. *Med. Phys.*, 31:2135–2146, 2004.

[16] Munro P and Bouius D C. X-ray quantum limited portal imaging using amorphous silicon flat-panel arrays. *Med. Phys.*, 25:689–702, 1998.

[17] Antonuk L E, El-Mohri Y, Huang W, Jee K W, Siewerdsen J H, Maolinbay V E, Scarpine V E, Sandler H, and Yorkstone J. Initial performance evaluation of an indirect-detection, active matrix flat panel imager (AMFPI) prototype for megavoltage imaging. *Int. J. Radiat. Oncol. Biol. Phys.*, 42:437–454, 1998.

[18] Sheikh-Bagheri D and Rogers D W O. Sensitivity of megavoltage photon beam Monte Carlo simulations to electron beam and other parameters. *Med. Phys.*, 29:379–390, 2002.

CHAPTER 4
The aS500 Portal Imager Dosimetric Properties

4.1 Introduction

Electronic portal imaging devices (EPIDs) were originally designed and developed for the purpose of geometric verification of patient set-up. However, their use has been extended to obtain dosimetric information of the treatment delivery. Careful examination of the dosimetric properties of the portal imager is an essential first step if one wants to use the EPID as a dosimeter.

The EPID used in this study is the Varian aS500 EPID. A more detailed description of the detector is found in chapter 2. Various studies have investigated the dosimetric properties of aSi EPID [1–6] and reached different conclusions, especially concerning the amount of buildup necessary for absolute dosimetry and the effect of ghosting (section 2.2.1). These characteristics may be manufacturer dependent. It is therefore essential to verify the dosimetric characteristics of each portal imager used for dosimetric purposes. In this section, various dosimetric properties of the aS500 EPID such as the buildup effect, the dose and dose rate dependence, the field size response, the ghosting effect and the effect of dead time and leaf speed are investigated.

4.2 Materials and Methods

4.2.1 Image Acquisition

The dosimetric characteristics of the Varian aS500 EPID were tested for a 6 MV beam. Images were acquired for 10 consecutive frames, at a nominal dose rate of 400 Monitor Unit (MU) per minute at the isocenter and a source-to-detector distance (SDD) of 105 cm unless stated otherwise. The 10 frames were averaged to obtain a single image which was then processed using a dark and a flood field pixel-by-pixel calibration (equation 4.1).

$$I(i,j) = \frac{(I_{\text{raw}}(i,j) - DF(i,j))}{(FF(i,j) - DF(i,j))} \times \text{mean}(FF - DF) \tag{4.1}$$

where $I_{\text{raw}}(i,j)$ is the raw pixel intensity for pixel i,j, $I(i,j)$ is the calibrated intensity, and the mean is taken over all detector pixels. The dark field (DF) image is acquired for 60 frames with no radiation present and records the pixel offsets. The flood field (FF) image is acquired for 30 frames with an open field across the whole detector. The flood field corrects for the variation in pixel sensitivity. Previous investigators [1] have shown that varying SDD and adding solid water buildup can contribute in flattening the flood field, which should results in a better calibration. In this study, the flood fields were acquired with no solid water and with a 140 cm SDD to reproduce the clinical setup.

All measurements, including the ion chamber measurements, were repeated three times. Their average is reported and the standard deviation between the three measurements is used to establish the uncertainty on the measurements.

4.2.2 Buildup Effect

In order to ensure there is sufficient inherent detector buildup, the effect of adding different thicknesses of buildup on the detector surface was investigated. The effect of buildup material was studied for three field sizes: (5×5) cm^2, (10×10) cm^2, and (25×25) cm^2. Solid water ^{TM}(GAMEX rmi, Middleton WI) slabs were placed on top of the portal imager. The amount of solid water was varied from 0.5 cm to 2 cm in 0.5 cm increments. The mean EPID signal in a (10×10) pixel^2 $((0.784 \times 0.784)$ cm$^2)$ region of interest (ROI) at the center of the field was calculated. The values presented were normalized to the mean when no buildup is present.

4.2.3 Dose and Dose Rate Response

The linearity of the detector with dose was obtained by increasing the number of MUs delivered. The EPID image is an average of the frames acquired during the beam delivery. Hence to obtain the total signal received by the detector, the average detector signal must be multiplied by the number of frames acquired. Since there is a dead time of three frames every 64 frames (section 2.2), the number of frames acquired must be corrected for that dead time. For example an image acquired for 100 frames must be multiplied by 97 since 3 frames are missing due to one dead time.

The linearity of the detector with dose rate was also investigated. The dose rate was varied by changing the distance between the linac source and the detector. Relative dose rates were computed by obtaining IC10 ion chamber (Scanditronix-Wellhofer) readings for the different distances and assuming a dose rate of 400

MU/min at 100 cm from the source. Both the dose and dose rate response images were obtained for a (10 × 10) cm^2 field size. For each of these images the mean EPID signal in a (10 × 10) $pixel^2$ ROI at the center of the field was calculated.

4.2.4 Field Size Response

The EPID field size response was compared to an ion chamber field size response. The ion chamber measurements were acquired with an IC10 ionization chamber in a 20 cm solid water phantom at the depth of dose maximum for a 6 MV beam (1.5 cm). The field size was varied from (5 × 5) cm^2 to (25 × 25) cm^2. The mean EPID signal in a (10 × 10) $pixel^2$ ROI at the center of the field was calculated. The ion chamber reading and the mean ROI values were normalized to the (10 × 10) cm^2 field value.

4.2.5 Ghosting Effect

The time decay of the ghosting effect was investigated by acquiring a series of images after irradiation of the detector. The irradiation consisted of a (4 × 4) cm^2 field size and a 6 MV beam delivered for 50 MUs. A 50 MUs delivery was chosen since Winkler *et al* [3] showed that the ghosting is more important for such MU settings. Shortly after irradiation 16 images were acquired at regular time intervals over a 60 second period. The images were acquired for 1 frame only. The mean EPID signal in a (10 × 10) $pixel^2$ ROI was evaluated for each image. The residual signal in percentage was obtained by dividing the mean image signal by the mean signal for the original (4 × 4) cm^2 field size image.

4.2.6 Dead Time Effect

The aS500 EPID acquisition software used for this project has not been upgraded to the new version in which dead time can be avoided. The effects of dead

time on a sliding window delivery were investigated. The sliding window field was designed so that a typical MLC leaf gap of 1 cm swept symmetrically across the field, homogeneously irradiating a (10 × 10) cm^2 field size, while the jaws, set to their default position defining an (11.6 × 10.4) cm^2 field, remained stationary. Sliding window deliveries with leaf speeds ranging from 0.25 cm/s to 2.5 cm/s were imaged. Images were acquired for a number of frames corresponding to the whole sliding window delivery. Profiles were obtained along the direction of leaf motion. The errors produced by the dead time were computed as a percent difference.

4.2.7 Effect of Leaf Speed

In order to ensure that the EPID accurately records rapid changes in dose rate during dynamic MLC delivery, the EPID response to sliding window delivery was compared to the ion chamber response. The sliding window fields described above were used. The effect of the leaf speed on the EPID signal was studied by looking at the mean EPID signal in a (10 × 10) $pixel^2$ ROI at the center of the field. The ion chamber measurements were obtained using an IC10 chamber in 20 cm solid water at a 1.5 cm depth.

4.3 Results and Discussion

4.3.1 Buildup Effect

Table 4–1 shows the normalized detector signal obtained for different thicknesses of buildup material with a 6 MV photon beam. The maximum signal is obtained when no buildup is present on top of the detector for all field sizes. These results are in close agreement to the ones presented by Greer *et al* [1] who found that for a (10 × 10) cm^2 field and a 6 MV beam a solid water thickness of 0.5 cm gives the

maximum signal. Employing an adequate amount of buildup is important for three reasons: (1) to absorb low-energy electrons before reaching the EPID sensitive layer, these would otherwise reduce image quality; (2) to ensure electronic equilibrium at the sensitive layer of the detector for dosimetry and (3) to minimize the scattered photons from the patient that reach the active layer of the EPID. Our results indicate that the 1 mm copper layer inherent to the portal imager is sufficient to ensure we are passed the buildup region and hence we can assume that electronic equilibrium is reached. It is also very likely that most low energy electrons are stopped given that a 1 MeV electron has a 0.07 cm continuously slowing down approximation (CSDA) range in copper. For all practical purposes the CSDA range can be defined as the expectation value of the path length that the particle follows until it comes to rest [7]. MC simulations are required to determine if this amount of copper is sufficient to remove most of the scattered photons. MC simulations (the EPID model is described in chapter 3) looking at different amounts of buildup showed that for a 1 mm copper layer 55% of the scattered photons are stopped and 13% of the primary photons are stopped. The buildup layer also produces some scattered particles, in the case of the 1 mm copper layer 8% of the primary beam produces scattered particles that reached the detector. A thickness of 20 mm of copper would be necessary to stop 75% of the scattered photons, however this would also stop 30% of the primary beam. As it will be shown in chapter 6, the scattered radiation can be removed using image post processing. Note that if higher energies are used then the requirement for buildup would have to be reassessed.

Table 4–1: Normalized detector signal recorded in the aS500 EPID for different thicknesses of solid water placed directly on top of the detector for a 6 MV beam and a 105 cm SDD.

	Normalized Signal (%)		
Solid Water Thickness (cm)	(5 × 5) cm^2	(10 × 10) cm^2	(20 × 20) cm^2
0.0	100.0 ± 0.5	100.0 ± 0.5	100.0 ± 0.5
0.5	98.9 ± 0.4	99.9 ± 0.5	100.0 ± 0.5
1.0	97.4 ± 0.5	98.9 ± 0.5	99.2 ± 0.5
1.5	95.5 ± 0.4	98.2 ± 0.5	98.9 ± 0.5
2.0	86.1 ± 0.4	97.0 ± 0.5	97.6 ± 0.5

4.3.2 Dose and Dose Rate Response

Figure 4–1 shows the linear relationship between dose and EPID signal, while figure 4–2 shows the linear relationship between the relative dose rate and the EPID signal. The error on the measurements was inferior to 0.5%. Linear functions were fit to both curves and linear equations were obtained with R-square values of 1.0 for both the dose and dose rate fit. These results agree with data previously published [1, 4–6]. The linear response of the EPID signal to dose makes dosimetry simpler since a linear calibration between pixel value and dose can be used. The fact that the EPID signal varies linearly with dose rate indicates that the detector response is independent of the dose rate. This is essential to EPID dosimetry since attenuation in the patient can create fluctuation in the dose rate.

4.3.3 Field Size Response

The aS500 EPID field size response is compared to an ion chamber field size response in figure 4–3. The error on the detector and the ion chamber measurements were inferior to 0.5%. The aS500 over responds to large field sizes and under responds

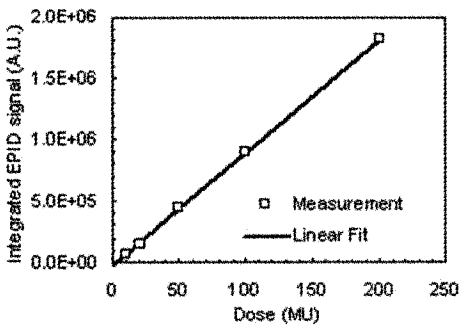

Figure 4–1: Linearity of the EPID with dose for a (10 × 10) cm^2, 6 MV beam and 105 cm SDD.

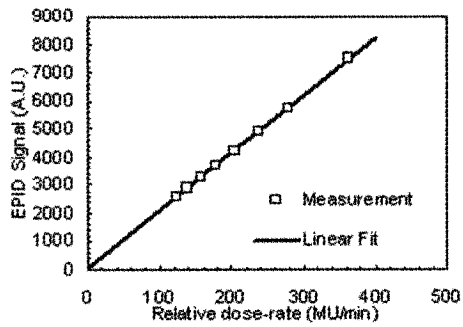

Figure 4–2: Linearity of the EPID with dose rate for a (10 × 10) cm^2, 6 MV beam and 105 cm SDD.

to small field sizes compared to the ion-chamber response. This effect has been explained by Greer *et al* [1] as being due to the high response to low energies of the aS500 EPID. A larger field size will have a more important scatter contribution and hence a higher low energy component. As shown in figure 3–3, the aS500 has in fact a higher dose response to lower energies. This dose versus energy dependence has been attributed to the materials with high atomic number which are part of the phosphor layer [8].

4.3.4 Ghosting Effect

Figure 4–4 shows the amount of residual signal as a function of time. The ghosting signal was found to decay exponentially as a function of time. For a time interval smaller than 3 s the amount of ghosting signal is around 2%; after 10 s the ghosting is inferior to 0.2%. These results agree with the findings of Greer *et al* [1] who showed that the ghosting is negligible over a time interval of 15 s. However they disagree with the results of Winkler *et al* [3] who found an effect of 5.5% for 7.5 s

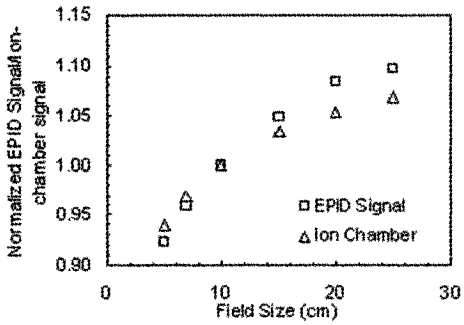

Figure 4–3: Field size response of the EPID compared to ion-chamber measurements for a 6 MV beam, 400 MU/min and 105 cm source-to-detector distance. Data is normalized to the (10 × 10) cm^2 field.

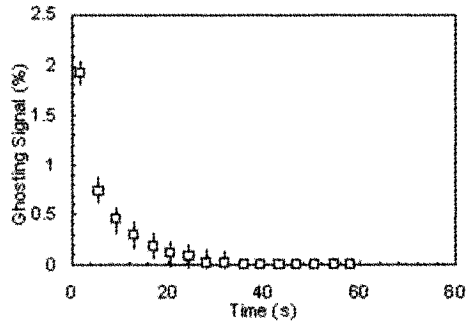

Figure 4–4: Effect of ghosting (%) as a function of time after the EPID irradiation.

interval. The latter study used the IVIEWGT Elekta EPID which may have different ghosting properties due to different image acquisition and reading techniques. The ghosting effect is something that must be kept in mind when delivering IMRT fields. A frame by frame acquisition of an IMRT delivery would suffer from ghosting which would show as a loss in signal in certain regions and an increase in signal in other regions. These losses and gains would be due to the delay in signal. However, an averaged frame acquisition, integrated over the whole IMRT delivery, would not suffer from this type of ghosting since all the signal would be collected and averaged.

4.3.5 Dead Time Effect

Figure 4–5(a) shows the effect of dead time on EPID signal profiles. The dead time causes a reduction in the EPID signal. For the highest leaf speed requiring a number of frames inferior to 64 the profile is uniform. The error due to the dead time increases linearly with leaf speed as shown in figure 4–5(b). This is because, as the

leaf speed increases a given detector region is exposed to the beam for a shorter time and so a small dead time in sampling becomes more important. It is now possible to correct for this problem by installing a software patch provided by the manufacturer. This patch was not available for this project. IMRT fields are delivered with variable leaf speeds, the error due to dead time could be up to 20% for very rapid leaf speed but it would affect only small regions of the overall detector signal.

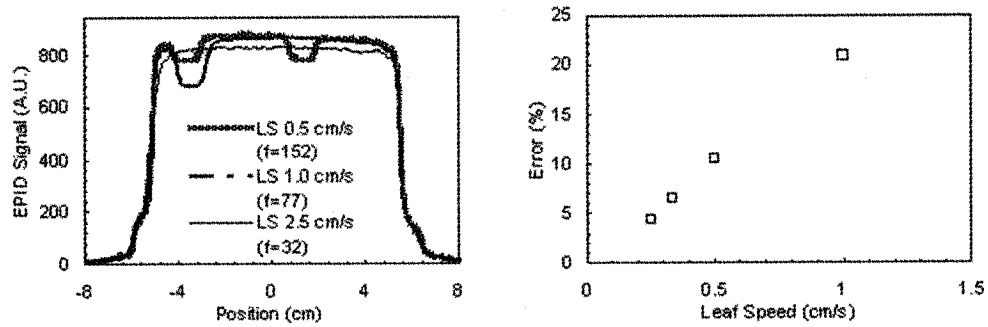

(a) (b)

Figure 4–5: (a)The effect of the dead time on the recorded signal when using a sliding window delivery for different leaf speeds (LS) and different number of averaged frames (f) and (b) the error in EPID signal due to the dead time as a function of the leaf speed. 6 MV beam, 400 MU/min and 105 cm SDD.

4.3.6 Effect of Leaf Speed

The effect of leaf speed on signal linearity is shown in figure 4–6. A linear function was fitted to the data and an R-square value of 1.0 was obtained. This shows that the EPID can accurately record rapid changes in dose rate, which is essential for IMRT dosimetry.

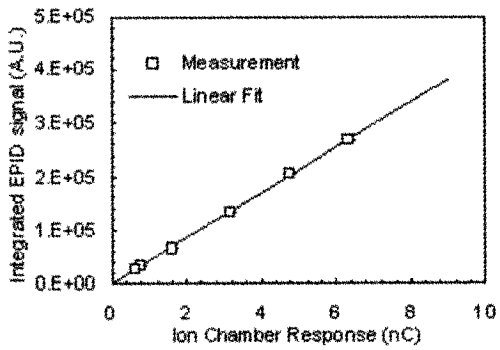

Figure 4–6: Linearity of the EPID signal with leaf speed for sliding window delivery using a 6 MV beam, 400 MU/min, and 105 cm source-to-detector distance. The linear fit has an R square value of 1.0.

4.4 Conclusion

Various dosimetric properties of the aS500 portal imager were assessed. Dosimetric properties such as the linearity of the dose response and the dose rate were found to agree with previously published data [1, 4–6]. The aS500 EPID is a good candidate for IMRT treatment verification since it exhibits a good response to rapid leaf changes and very little ghosting. In the next chapters we will see how the aSi EPID can be used to acquire images of electron beam treatments (chapter 5) and how it can be used for patient dosimetry (chapter 6).

References

[1] Greer P B and Popescu C C. Dosimetric properties of an amorphous silicon electronic portal imaging device for verification of dynamic intensity modulated radiation therapy. *Med. Phys.*, 30:1618–1627, 2003.

[2] McDermott L N, Louwe J W, Sonke J J, van Herk M B, and Mijnheer B J. Dose-response and ghosting effects of an amorphous silicon electronic portal imaging device. *Med. Phys.*, 31:285–295, 2004.

[3] Winkler P, Hefner A, and Georg D. Dose-response characteristics of an amorphous silicon EPID. *Med. Phys.*, 32:3095–3105, 2005.

[4] McCurdy B M C, Luchka K, and Pistorius S. Dosimetric investigation and portal dose image prediction using an amorphous silicon electronic portal imaging device. *Med. Phys.*, 28:911–924, 2001.

[5] El-Mohri Y, Antonuk L E, Yorkston J, Jee K W, Maolinbay M, Lam K L, and Siewerdsen J H. Relative dosimetry using active matrix flat-panel imager (AMFPI) technology. *Med. Phys.*, 26:1530–1541, 1999.

[6] Munro P. Megavoltage radiography for treatment verification. In *The Modern Technology of Radiation Oncology A Compendium for Medical Physicists and Radiation Oncologists*, editors, J van Dyk, chapter 13. Madison Medical Physics Publishing, Madison, 1999.

[7] Attix F H. *Introduction to radiological physics and radiation dosimetry.* Wiley, New York, 1986.

[8] Kirby C and Sloboda R. Consequences of the spectral response of an a-Si EPID and its implications for dosimetric calibration. *Med. Phys.*, 32:2649–2658, 2005.

CHAPTER 5
Electron Beam Radiotherapy Verification

The majority of external beam radiotherapy treatments are delivered using photon or electron beams. Although a lot of effort has been put into verification of patient positioning using portal imaging for photon radiotherapy treatments, very little investigating has been done into applying these techniques to electron beams. At the Montreal General Hospital (MGH) around 15% of patients are treated using electron beam therapy. Developing techniques to verify patient positioning during electron beam treatments is essential and is an important part of treatment verification. In this chapter, we present a paper published in *Physics in Medicine and Biology* which describes how the bremsstrahlung portion of electron beams can be used to produce portal images. Only the patient positioning component of treatment verification is considered. Monte Carlo simulations are used to characterize the bremsstrahlung beam produced in the linear accelerator head and to obtain predicted portal images. The quality of measured electronic portal images is evaluated using contrast, signal-to-noise ratio and resolution. The last section of this chapter was added to the published manuscript to demonstrate that the verification technique can be used clinically. Portal images obtained using a photon beam and an electron beam are compared in the case of a head and neck cancer patient undergoing electron beam treatment.

Title: Electron Beam Treatment Verification Using Measured and Monte Carlo Predicted Portal Images

Authors: G Jarry and F Verhaegen

Published in Physics in Medicine and Biology vol.50 p.4977-4994 (2005)

Abstract

Electron beam treatments may benefit from techniques to verify patient positioning and dose delivery. This is particularly so for complex techniques such as mixed photon and electron beam radiotherapy and electron beam modulated therapy. This study demonstrates that it is possible to use the bremsstrahlung photons in an electron beam from a dual scattering foil linear accelerator to obtain portal images of electron beam treatments. The possibility of using Monte Carlo (MC) simulations to predict the electron beam treatment portal images was explored. The MC code EGSnrc was used to model a Varian CL21EX linear accelerator (linac) and to characterize the bremsstrahlung photon production in the linac head. It was found that the main sources of photons in the electron beam are the scattering foils, the applicator and the beam-shaping cut-out. Images were acquired using the Varian CL21EX linac and the Varian aS500 electronic portal imager (EPI); four electron energies (6, 9, 12, 16 MeV), and different applicator and cut-out sizes were used. It was possible to acquire images with as little as 10.7 MU per image. The contrast, the contrast-to-noise ratio (CNR), the signal-to-noise ratio (SNR), the resolution and an estimate of the modulated transfer function (MTF) of the electron beam portal images were computed using a quality assurance (QA) phantom and were found to be comparable to those of a 6 MV photon beam. Images were also acquired using

a Rando anthropomorphic phantom. MC simulations were used to model the aS500 EPID and to obtain predicted portal images of the QA and Rando phantom. The contrast in simulated and measured portal images agrees within 5% for both the QA and the Rando phantom. The measured and simulated images allow for a verification of the phantom positioning by making sure that the structure edges are well aligned. This study suggests that the Varian aS500 portal imager can be used to obtain patient portal images of electron beams in the scattering foil linacs.

5.1 Introduction

It has long been recognized that the use of portal imaging can be of significant benefit in ensuring correct delivery of photon radiotherapy by limiting patient set-up and collimation errors [1, 2]. However, in the case of electron beam radiotherapy, portal imaging is not used clinically. For most electron beam treatments the target to be treated is superficial. In these cases, the projection of the light field on the patient skin is sufficient to ensure adequate patient positioning. However, various electron beam delivery techniques such as the combination of high energy electrons in conjunction with photons or the use of abutting fields, where cold spot and hot spots are an issue, may benefit from portal imaging. Recent interest in electron modulated radiotherapy where better dose conformity is achieved [3–5] also increases the need to develop techniques to verify patient positioning and field settings as well as tools to verify the dose delivery. Clinical electron beams contain an admixture of contamination bremsstrahlung photons, produced in various structures of the accelerator head, in the beam-defining cut-out and in the patient or phantom. The amount of contamination photons is dependent on the type of accelerator;

scanned electron beams have little bremsstrahlung contamination compared to scattering foil beams where the bremsstrahlung produced by the head dominates the one produced in the phantom or patient. Previous studies have shown experimentally that beam energy, collimation and cut-out shape influence the amount of photons produced [6, 7]. Keller [8] first suggested using the bremsstrahlung contamination in high energy electron beam to obtain electron beam radiographs. Gur *et al* [9] acquired both conventional films and storage phosphor images from 22 patients during their daily high energy beam treatments. They showed that the verification images obtained during the electron treatments are true projection images of the treatment field by comparison of images obtained with a photon beam. Portal film systems offer a relatively limited dose range over which the image is neither over- nor under-exposed which renders an electronic portal imaging device (EPID) more suitable for real-time verification images [2]. The amorphous silicon (aSi) EPID has a good sensitivity, a high resolution, a large active detection area and real-time acquisition capabilities [2]. The aSi EPID abilities as a patient positioning tool and as a dosimeter for conformal photon treatments and for IMRT have already been discussed in various studies [10–12]. There are two main approaches to verify the treatment delivery using an EPID: (i) comparison of a predicted fluence or dose at the detector with a portal image acquired during the treatment [11, 13, 14] and (ii) reconstruction of the dose in the patient from the portal image [15–17]. Although the aSi EPID has been used as a dosimetric and verification tool in photon radiotherapy, only a few preliminary studies have considered it for electron beam portal imaging. Baus and Vetterli [18] were among the first to suggest the use of the aSi EPID for electron

beam verification. Aubin *et al* [19, 20] suggested that it is possible to use the aSi EPID for routine clinical on-line electron beam verification. They obtained images of an anthropomorphic phantom, and showed that electron multi-leaf collimator shapes can be verified. More recently, Hansen [21] suggested using the aSi EPID in head and neck cases where electron fields are used to match photon fields. Although the studies have demonstrated that it is possible to acquire images during electron treatments none have done a detailed analysis of the photon production and of the image quality. The purpose of this study is to use the bremsstrahlung part of the electron beam to produce portal images during electron beam treatments and to evaluate their image quality. Monte Carlo (MC) simulation tools are used to characterize the photon production in electron beams and to acquire detailed information on where the photons were created and on their spatial, energy and angular distribution. The amount of bremsstrahlung produced by the linac head as well as its spectral and angular distribution play an important role in image formation and image quality. The contrast, the contrast-to-noise ratio (CNR), the signal-to-noise ratio (SNR), the resolution and an estimate of the modulation transfer function (MTF) of the images are evaluated and compared to images obtained with megavolt photon beams. The possibility of using MC simulations to predict the electron portal images and the use of the predicted images to verify electron beam treatments are also discussed.

5.2 Materials and Methods

5.2.1 Monte Carlo Simulations of the Photon Production in the Linac Head for an Electron Beam

The BEAMnrc MC code system [22] was used to build a linear accelerator model of the Varian CL21EX linac according to the manufacturer's specifications.

A schematic diagram of the accelerator model is shown in figure 5–1. The model includes the exit window, scattering foils, monitor chamber, jaws, applicator, and cut-out. A (20 × 20) cm^2 and a (10 × 10) cm^2 electron applicator as well as a (20 × 20) cm^2, a (10 × 10) cm^2 and a (5 × 5) cm^2 cut-outs were modeled. Four electron beam energies (6, 9, 12 and 16 MeV) were modeled with corresponding scattering foils. The primary electron beam energy (figure 5–1) was modeled as being a mono-energetic [23] divergent cone as suggested by Huang *et al* [24] who showed that the focal spot of electron beams in our Varian CL21 EX linac is elliptical and has a Gaussian spatial distribution. In order to tune the primary electron beam energy, particle transport in a (20 × 20 × 30) cm^3 water phantom with (0.2 × 1.0 × 0.2) cm^3 voxels was included in the simulations and simulated percent depth doses (PDD) were obtained; particles were recycled twice. Measured PDD were obtained using a diode detector. The primary electron beam energy was varied until the difference between the measured and simulated R_{50} and R_p (electron practical range) were within 0.5 mm and 1 mm respectively. Simulated and measured PDD for the four energies used as well as profiles at different depth for the 16 MeV beam and a (20 × 20) cm^2 filed size can be found in figure 5–2, similar agreement was obtained for the other configurations. The uncertainty on the simulation was less than 0.5% at R_{50}. For each simulation 2×10^8 primary electrons were incident on the electron

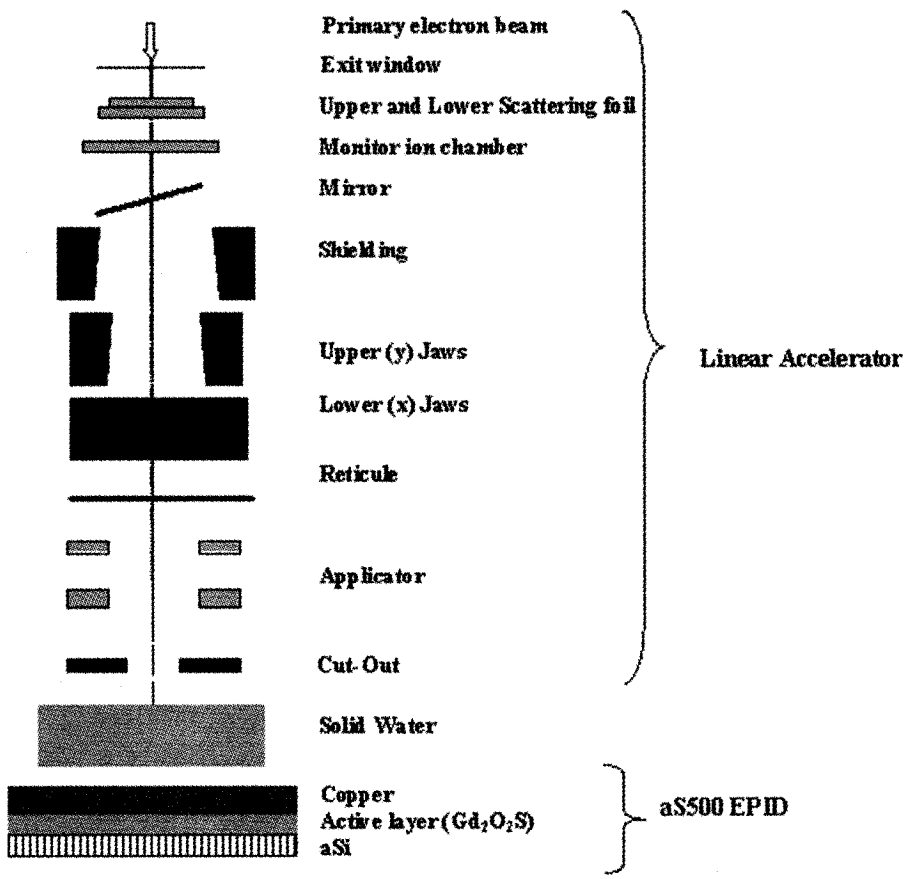

Figure 5–1: Schematic drawing of the linac components (electron configuration) of the solid water phantom and of the aS500 EPID modeled in Monte Carlo simulations.

exit window. The particles were tagged according to the linac component in which they were created. Phase space files (psf) were obtained just below the electron cut-out and contained information about the energy, the position and the direction of every particle reaching the phase space plane. The psf sizes varied from

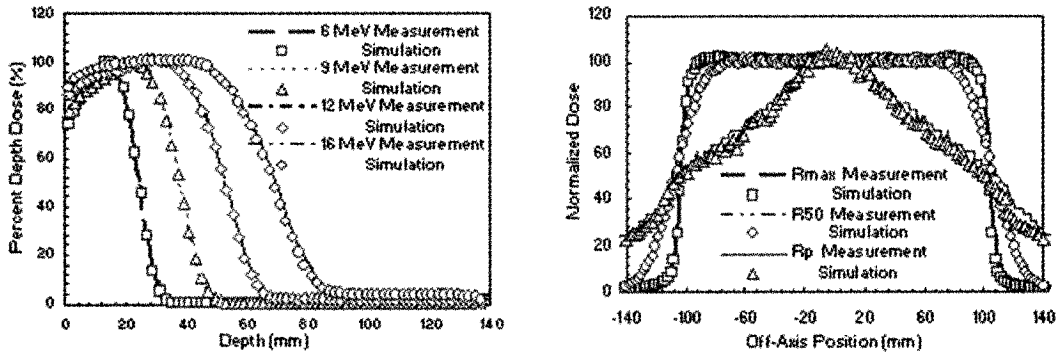

(a) (b)

Figure 5–2: (a)Simulated and measured percent depth dose curves in water for a 6, 9, 12 and 16 MeV beam and (b) off-axis profiles in water for a 16 MeV beam at R_{max}, R_{50} and R_p for a (20 × 20) cm^2 field size.

125 000 particles/cm^2 for the 6 MeV beam to 350 000 particles/cm^2 for the 16 MeV beam which was sufficient to ensure a statistical uncertainty below 2% when analyzing the psf. BEAMDP [25] was used to determine the fluence, the energy spectrum and the angular distribution of the psf particles.

5.2.2 Images Using an Electron Beam

The QC-3V phantom [26] was used to characterize the images obtained with the electron beams. The QC-3V phantom is a portal imaging QA phantom. It consists of 5 line pair (lp) sections with spatial frequencies varying from 0.1 lp/mm to 0.76 lp/mm. The line pair section is surrounded by 10 slabs of different material (Pb (ρ = 11.33 g/cm^3), Al (ρ = 2.69 g/cm^3), PMMA (ρ = 1.19 g/cm^3)) of various thicknesses (5 mm, 10 mm, 15 mm) which can be used to evaluate image contrast. The phantom is 1.5 cm thick and rests on 1.5 cm of plastic. Images were obtained using the Varian CL21EX linac, which uses the scattering foil principle and the Varian aS500

EPID. The aS500 EPID is an indirect detection system which consists of a 1 mm copper plate overlying a scintillating layer of phosphor (gadolinium oxisulfide) and a (40 × 30) cm^2 ((512 × 384) $pixels^2$) aSi light sensor photo diode array (figure 5–1).The QC-3V phantom was sandwiched between varying thicknesses of solid water to mimic patient geometry. The images were taken with four electron energies (6, 9, 12, 16 MeV), two applicator sizes ((10 × 10) cm^2 and (20 × 20) cm^2) and three cut-outs ((5 × 5) cm^2, (10 × 10) cm^2 and (20 × 20) cm^2). A 6 MV photon beam was used with the 6 MeV electron configuration, i.e. with the applicator and cut-out in place and with the corresponding jaw opening, to acquire images for comparison purposes. The distance between the source and the upper surface of the QC-3V phantom was fixed to 106 cm while the distance between the source and the surface of the imager was fixed to 135 cm. All images obtained used the continuous frame averaging mode, where a single image consists of the average of several image frames. As shown in table 5–1, increasing the number of frames will improve the SNR and the CNR. In this study the number of frames was fixed to 10 frames for all acquisitions; which corresponds to the 'high' quality setting when acquiring photon beam portal images. Although a larger amount of frames may be acquired in a clinical setting, this number of frames ensured that the SNR under a 7.5 mm lead square was superior to 30 for all energies and that the error on the contrast was below 5%. The images were acquired for an integration time of 0.160 s per frame at 400 MU/min (a monitor unit (MU) corresponds to the delivery of 0.01 Gy in the center of a (10 × 10) cm^2 field at the isocenter at the depth of maximum dose) for a total of 1.6 s or 10.7 MU per image. The image post-processing consisted in the subtraction of a dark field. The

dark field is an image acquired without radiation which is used to subtract defective pixels and electrometer offsets.

Table 5–1: Signal-to-noise ratio (SNR) and contrast-to-noise ratio (CNR) as a function of the number of averaged frames for images acquired with 6, 9, 12 and 16 MeV beam, a (10 × 10) cm^2 cut-out and applicator with a 106 cm source-to-surface distance (SSD) and a 135 cm source-to-detector distance (SDD).

	6 MeV		9 MeV		12 MeV		16 MeV	
Average frame	SNR	CNR	SNR	CNR	SNR	CNR	SNR	CNR
4.0	21.6	2.8	46.3	4.6	73.0	6.7	136	6.9
10.0	29.9	3.7	60.7	5.4	114	8.3	254	10.5
20.0	40.8	5.2	85.5	7.6	147	11.5	317	13.2
50.0	67.6	8.9	121	10.4	243	19.1	498	20.2
100.0	72.7	9.6	156	13.4	288	22.6	664	26.3

The MTF [27] was estimated using the line pair pattern of the QC-3V phantom. The method used only gives an estimate of the true MTF [28]; however this is sufficient for the purpose of this study which is to compare different ways of acquiring images. The technique used is described in detail by Rajapakshe *et al* [29]. The MTF is given by equation 5.1,

$$\mathrm{MTF}(f) = \frac{M(f)}{M(f_1)} \tag{5.1}$$

where $M(f)$ is the measured total variance in a region of interest placed on the bar pattern minus the variance due to random noise (σ). To ensure that the low frequency minimum is reached two adjacent contrast blocks of lead and plastic were used to compute $M(f_1)$, which corresponds to a frequency of 0.025 lp/mm. The 0.76 lp/mm bar pattern was not used due to aliasing at that resolution. The resolution

was then determined by extracting f50, the lp/mm frequency when the relative MTF is at 50%, from the MTF using linear interpolation.

The image contrast, the CNR and the SNR were determined using the image produced by the 7.5 mm and 15 mm slab of lead in the QC-3V phantom. The contrast, the CNR and the SNR were calculated according to equation 5.2, 5.3 and 5.4 respectively; where I_1 and I_2 respectively represent the detector intensity in a (0.8×0.8) cm^2 region of interest in the 7.5 mm and 15 mm lead regions.

$$\text{contrast} = \frac{(I_1 - I_2)}{(I_1 + I_2)} \times 200 \tag{5.2}$$

$$\text{CNR} = \frac{(I_1 - I_2)}{\sigma} \tag{5.3}$$

$$\text{SNR} = \frac{I_1}{\sigma} \tag{5.4}$$

An anthropomorphic phantom, Rando (Rando Alderson Corp.), was used to acquire images of a geometry closely related to human anatomy. The images were acquired under the same conditions as the QC-3V images. However, in this case the source to surface distance (SSD) was set to 100 cm and the source to detector distance (SDD) was set to 140 cm.

5.2.3 Monte Carlo Simulation of Portal Images

The effect of adding material in the beam on the photon fluence and on the photon average energy was studied using the DOSXYZnrc_phsp program [30]. This program is a modified version of the DOSXYZnrc program [31] which allows to obtain a psf after the dose scoring geometry (represented by the solid water slab in our case).

The psf particles of section 5.2.1. were transported through various thicknesses of solid water and through the portal imager, the psf particles were not recycled. The portal imager model was based on the Varian aS500 EPID and was developed according to the manufacturer's specifications[1] . The backscatter produced by the detector mounting was simulated by including the necessary solid water thickness [32]. The aS500 EPID model was implemented using the DOSXYZnrc_phsp program and the DOSXYZnrc program. The psf were scored after the phosphor layer of the detector and were analyzed using BEAMDP to obtain the relative number of photons in the beam and their average energy, the statistical uncertainty on these simulations is less than 2%. The DOSXYZnrc_phsp program was also used to transport the psf particles of section 5.2.1 through various phantoms; the psf particles were never recycled more than four times. The simulated phantoms included the QC-3V phantom as well as the head of the Rando phantom (voxel size $(0.2 \times 0.2 \times 0.2)$ cm^3). The QC-3V phantom was modeled using the materials and densities described in section 5.2.2; the voxel size varied from 0.01 cm in the bar pattern section to 2 cm in the contrast section. A psf was scored after the phantoms and the DOSXYZnrc program was used to transport the electrons and the photons from this point through the EPID. Since the response of the light sensor (photodiode) is proportional to the energy deposition in the phosphor [33, 34] simulated images can be obtained by scoring the dose in the gadolinium oxisulfide layer of the detector. The simulated dose images were converted to an EPID signal using the following procedure. An open field image

[1] Personal communication 2004

was obtained with the (20 × 20) cm^2 applicator and (20 × 20) cm^2 cut-out and with nothing in the beam except solid water of a thickness exceeding the practical electron range (R_p) value. A sufficient amount of solid water is necessary to make sure that the image is formed only by the contamination photons and that no electrons contribute to the signal. This open field image is both measured and simulated. The ratio of the measured calibration image (EPID signal) to the simulated calibration image (dose per particle) gives a two-dimensional array of calibration factors that can be applied to the simulated image to convert them to EPID signal. This procedure is expressed mathematically in equation 5.5, where i and j are pixel indices.

$$\begin{aligned}\text{simulated calibrated images}(i,j) &= \text{simulated image}(i,j) \\ &\times \frac{\text{measured calibration image}(i,j)}{\text{simulated calibration image}(i,j)}\end{aligned} \tag{5.5}$$

5.3 Results and Discussion

5.3.1 Photon Production in the Linac head

Table 5–2 gives the relative contributions of photons produced in various parts of the linac, as well as the percentage of photons in the total particle fluence. Figure 5–3 shows how the spatial distribution, energy spectrum and angular distribution vary according to where the photons are created for a 6 MeV, (10 × 10) cm^2 electron beam at isocenter. The normalized fluence is obtained by summing one over the cosine of the particle angle with respect to the scoring plane normal in each bin in the cases of the spatial distribution and the energy spectrum and summing the particles in each bin in the case of the angular distribution [25]. It is then normalized to unity at the

Table 5–2: Photon production percentage for different components of the Varian CL21EX and for different beam energies, applicator and cut-outs as well as photon and electron percentage in the total particle fluence.

Applicator size	(10×10) cm^2				(10×10) cm^2				(20×20) cm^2			
Cut-out size	(5×5) cm^2				(10×10) cm^2				(20×20) cm^2			
Energy (MeV)	6	9	12	16	6	9	12	16	6	9	12	16
Exit window	3.1	1.6	1.4	1.1	4.8	2.7	2.1	1.5	3.8	2.8	1.3	0.9
Scattering foil (upper)	26.6	15.8	16.8	23.2	38.0	25.5	28.5	37.2	41.6	28.0	26.9	37.5
Scattering foil (lower)	6.3	5.7	5.4	3.3	9.2	9.3	9.6	5.8	11.2	11.9	11.7	7.4
Ion chamber	1.2	0.8	0.5	0.4	1.8	1.4	0.9	0.6	2.5	2.1	1.5	1.0
Jaws	3.6	3.4	3.2	3.1	4.0	4.2	4.2	3.9	4.3	4.3	3.9	4.0
Applicator	20.1	25.0	19.7	18.6	21.6	30.2	25.1	23.5	3.2	2.6	1.7	1.0
Cut-out	37.8	46.9	52.4	50.0	18.9	25.5	28.8	26.9	30.6	47.2	51.7	47.2
Other components	1.3	0.8	0.6	0.3	1.7	1.2	0.8	0.6	2.8	1.1	1.3	1.0
Electron	24.0	16.1	12.7	8.9	48.6	39.2	32.7	23.6	68.6	61.2	49.9	40.6
Photon	76.0	83.9	87.3	91.1	51.4	60.8	67.3	76.4	31.4	38.8	50.1	59.4

maximum point of the distribution. The main sources of photons, contributing to varying degrees depending on the beam configuration, are the scattering foils, the applicator and the cut-out. The latter has the highest contribution to the photon fluence beyond the edge of the field as shown in figure 5–3. The jaws contribute very little to the photon production. Although many photons are created in the jaws, most of them are stopped by the applicator and the cut-out. The curvature in the central part of the profile is caused by the upper scattering foil and by the exit window while the applicator and the cut-out are responsible for the wide angled scattered photons at the isocenter. The dimensions of the applicator, the cut-out as well as the beam energy have a direct impact on the relative number of photons produced. As shown in the last two rows of table 5–2, larger field sizes have a lower

relative number of photons with respect to electrons, since for those fields a smaller portion of the applicator and cut-out are exposed to the electron beam. Figure 5–4 shows how the total photon fluence, spectrum and angular distribution of a 6 MeV beam vary with the field sizes, defined by the cut-out.

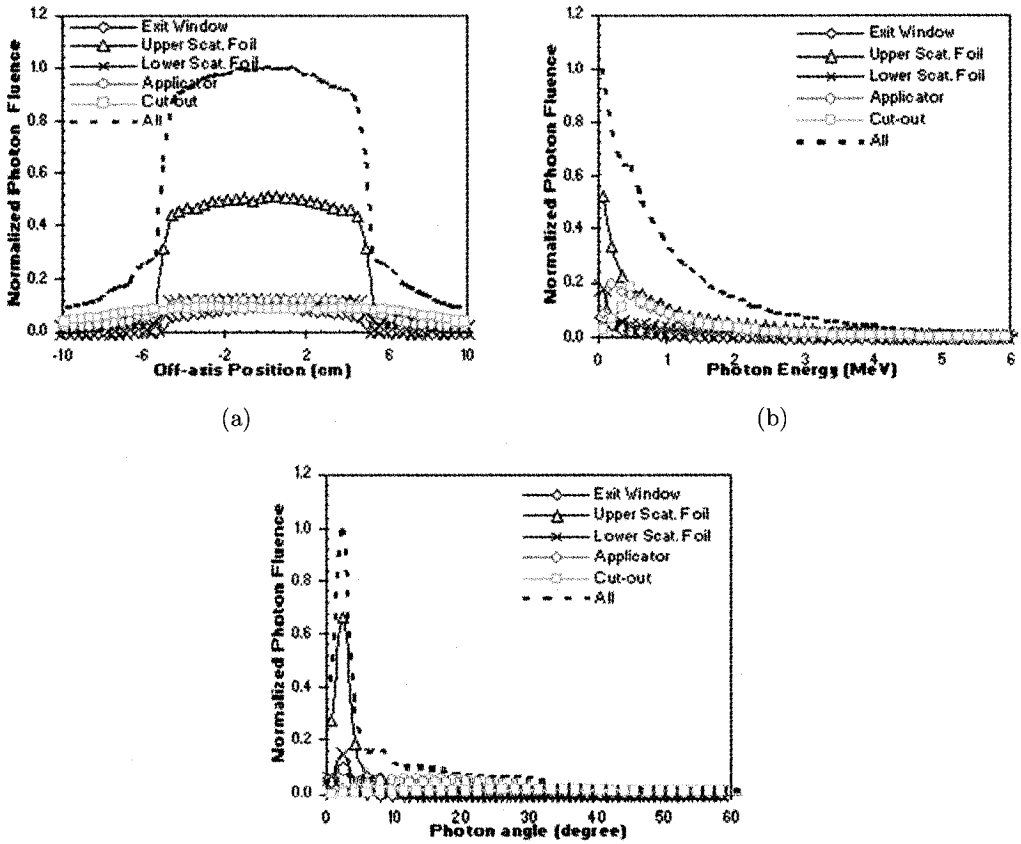

(a) (b)

(c)

Figure 5–3: (a)Particle distribution ,(b) spectral distribution averaged over a (20 × 20) cm^2 scoring plane and (c) angular distribution averaged over a (20 × 20) cm^2 scoring plane as a function of where the photons were created in the linac head for a 6 MeV electron beam and a (10 × 10) cm^2 field size at isocenter.

As shown in table 5–2 the relative number of photons goes up with increasing energy. As the energy increases, the bremsstrahlung x-rays, created in the scattering foil, tend to go in the electron's direction [35] and photon angular distribution is more forward as shown in figure 5–5. Figure 5–5 shows how the total photon fluence, spectrum and angular distribution of a (10 × 10) cm^2 field size vary with energy.

Table 5–3: Average energy of the photons (MeV) for different electron beam energies, applicator and cut-out sizes, and differentiated according to site of origin.

Applicator size	(10 × 10) cm^2				(10 × 10) cm^2				(20 × 20) cm^2			
Cut-out size	(5 × 5) cm^2				(10 × 10) cm^2				(20 × 20) cm^2			
Energy (MeV)	6	9	12	16	6	9	12	16	6	9	12	16
Exit window	1.4	1.8	2.2	2.8	1.1	1.5	1.9	2.6	1.0	1.4	1.9	2.6
Scattering foil (upper)	1.6	2.1	2.6	3.2	1.3	1.7	2.1	2.8	1.1	1.4	1.9	2.6
Scattering foil (lower)	1.5	2.0	2.4	2.9	1.1	1.5	1.9	2.3	0.9	1.2	1.6	2.0
Ion chamber	1.5	2.0	2.4	2.9	1.1	1.5	1.8	2.2	0.8	1.2	1.6	1.9
Jaws	1.6	2.1	2.5	2.9	1.4	1.9	2.4	2.8	1.2	1.7	2.1	2.5
Applicator	1.4	1.8	2.2	2.6	1.2	1.7	2.0	2.4	0.8	1.1	1.4	1.7
Cut-out	1.4	1.8	2.1	2.3	1.3	1.6	1.9	2.2	1.4	1.8	2.1	2.4
Total	1.5	1.9	2.2	2.6	1.2	1.6	2.0	2.5	1.1	1.6	2.0	2.4

The average energies of the photons produced by different parts of the linear accelerator as a function of beam energy and field size are shown in table 5–3. Larger field sizes tend to have lower average energy due to the increase in scattered radiation. The average energy obtained with MC calculations indicates that the bremsstrahlung portion of the beam is softer than the x-ray beam of corresponding nominal energy. This is in agreement with the findings of Zhu *et al* [7]. Previous studies [36, 37] have reported an average energy of 1.8 to 1.9 MeV for 6 MV photon beams from the Varian linacs when large fields are used; hence in the case of the 6 MeV, (20 × 20) cm^2

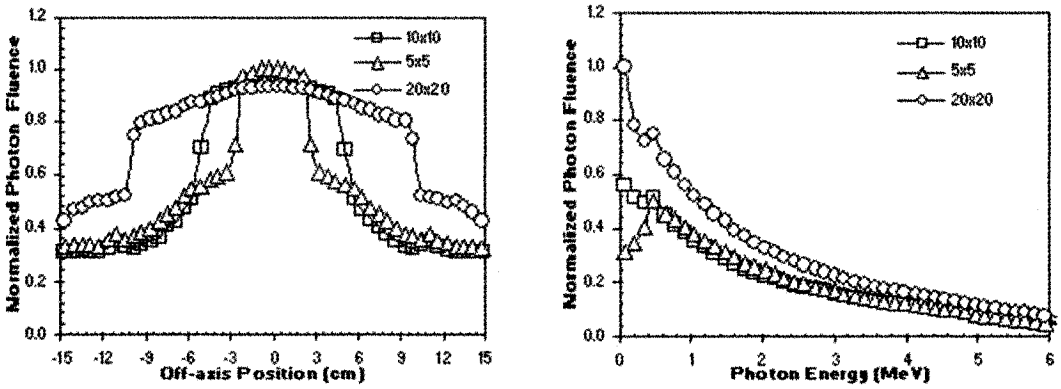

(a)

(b)

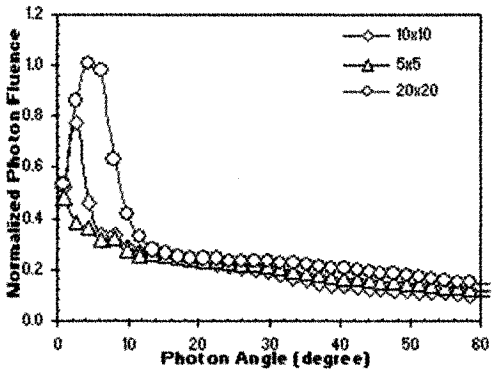

(c)

Figure 5–4: (a) Particle distribution , (b) spectral distribution averaged over a (20 × 20) cm^2 scoring plane and (c) angular distribution averaged over a (20 × 20) cm^2 scoring plane for all photons created by the linac head as a function of field size for a 6 MeV electron beam.

electron beam the corresponding x-ray beam has an average energy which is more than 50% higher.

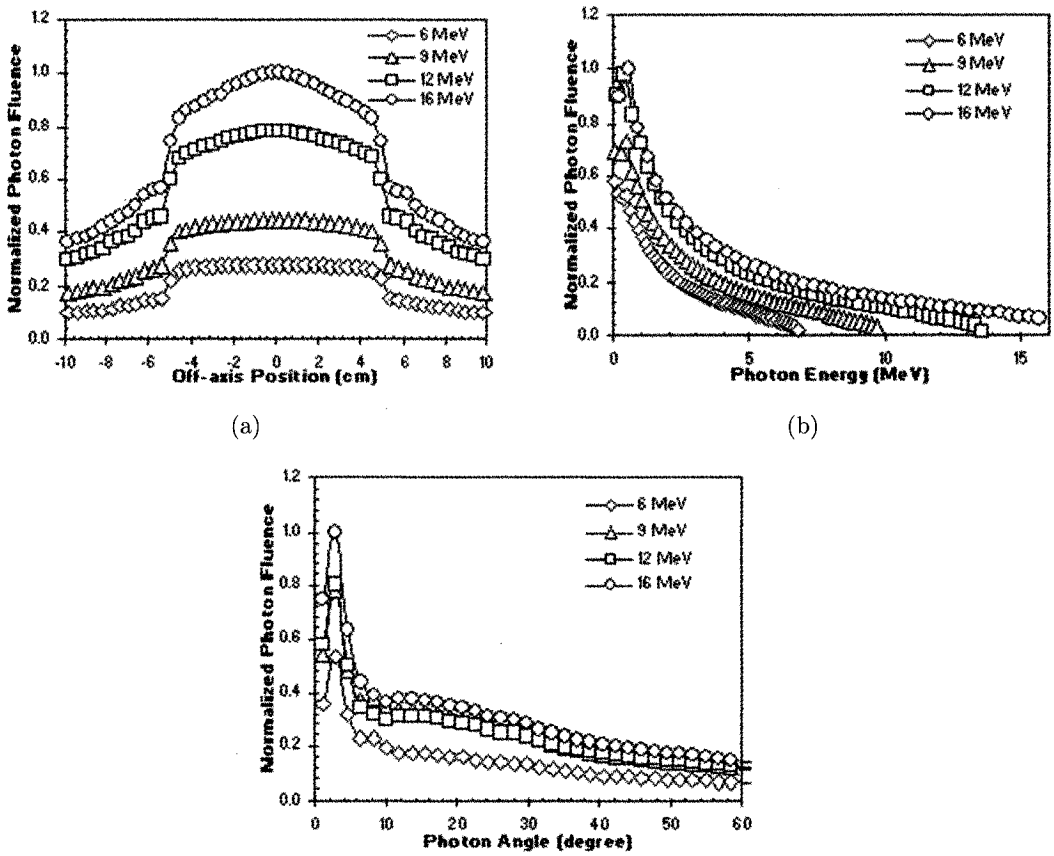

Figure 5–5: (a) Particle distribution , (b) spectral distribution averaged over a (20 × 20) cm^2 scoring plane and (c) angular distribution averaged over a (20 × 20) cm^2 scoring plane for all photons created by the linac head as a function of energy for a (10 × 10) cm^2 field size at isocenter.

5.3.2 Image Characterization

The image quality is highly dependent on photon production. The contrast, the CNR, the SNR and the resolution of the QC-3V phantom images obtained for different thicknesses of solid water, different beam energies, different applicator sizes

and different cut-outs can be found in table 5–4. The SNR is highest for higher energy beams, larger field sizes and photon beams which are the configurations that generate the most photons. The SNR tends to be low for electron beam images but it can always be improved by acquiring more frames, as shown in table 5–1. The CNR is also improved when increasing the number of frames, however the relation between CNR and the number of photons created in the linac head is not as direct as the SNR relation due to the contrast dependence on energy and field size. The contrast is highest for small fields and low energies. The lower energy electron beams have a lower photon average energy (table 5–3) which leads to an increase in the number of photoelectric interactions and hence an improvement in contrast. The scatter contribution at the center of the larger fields is greater which deteriorates the contrast. The resolution is highest for higher energy beams and for smaller field sizes. The resolution obtained with the electron beams is comparable to the one obtained with the photon beams. In figure 5–6, which shows how the MTF varies for different beam configurations, it can be seen that the MTF obtained with the four electron beam energies is comparable to the one obtained with the 6 MV photon beams. Higher energy beams tends to have a better MTF; this is due to the reduced amount of scattered radiation in the phantom for higher energies. Similar to our findings for the resolution, the MTF degrades when a large amount of solid water is placed on top of the QC-3V phantom or when the (20 $\times$ 20) cm^2 applicator and cut-out are used. These configurations produce more scattered radiation which blurs the images and reduces the resolution. Moreover, in the case of the large fields, the scattered radiation produced by the applicator and cut-out has a wide angle when it

reaches the field center since it was produced farther away than in the case of smaller field. In fact, looking at a (1 × 1) cm^2 region at the center of the EPID, Monte Carlo calculations determined that the average angle of the particles created by the cut-out and the applicator is 15.6 , 16.0 and 36.0 , for a (5 × 5) cm^2, a (10 × 10) cm^2, a (20 × 20) cm^2 field respectively.

Figure 5–7 and 5–8 show images of the QC-3V phantom sandwiched between two slabs of 10 cm of solid water, obtained with different electron energies and different applicators and cut-outs. In figure 5–8, it can be seen that although the higher energy beams are more forward peaked (figure 5–5(a)), the images are not significantly affected by the fluence profile curvature. In all four images, it is possible to distinguish the 10 contrast squares. Note also that the cut-out and the applicator produce an image which can be seen surrounding the QC-3V phantom image. Figure 5–8 shows an image obtained with a (5 × 5) cm^2 cut-out; it can be seen that the photons going through the metal of the applicator also produce an image of the phantom. In MV photon portal imaging a double exposure technique is used to align the field with respect to the anatomy. In this technique the portal image is superimposed on top of an open field image [38]. The double exposure technique is not necessary in the case of electron beam portal imaging since it is possible to see the field shape superimposed on the geometry. Figure 5–9 shows measured images of the head of the Rando phantom obtained with a 9 MeV beam and with a 6 MV photon beam with the 9 MeV electron configuration. The nose, the mouth as well as the contour of the head can be identified on both images. The two images are of comparable overall image quality. However, the image acquired with the electron beam suffers

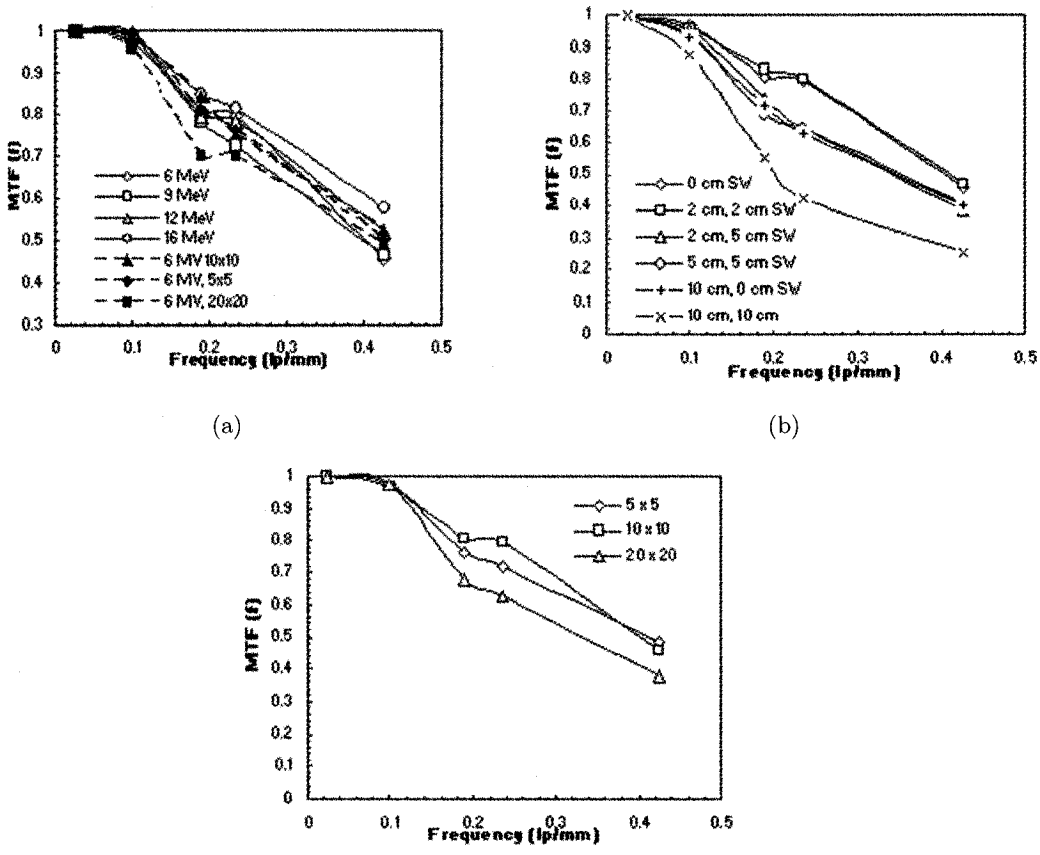

Figure 5–6: (a) MTF, obtained using the QC-3V phantom with 96 cm SSD and 135 cm SDD, for different beam energies, no solid water (SW) and a (10 × 10) cm^2 field size ,(b) various solid water thicknesses on top and under the QC-3V phantom, a 6 MeV beam and a (10 × 10) cm^2 filed size and (c) different cut-out sizes with a 6 MeV beam and no solid water .

from over-exposures at the left and at the right of the phantom outside of the useful part of the image. This is due to the field size being larger than the phantom and hence electrons reaching the portal imager directly. Monte Carlo simulations of the

photon transport only have shown that this effect can be removed by making sure only photons reach the portal imager.

Table 5–4: Contrast and resolution measured with the QC-3V phantom sandwiched between various thicknesses of solid water for different beam energies, applicator sizes and cut-out sizes, 106 cm SSD and 135 cm SDD. The first three rows of the table present results for photon beams acquired with the 6 MeV electron configuration, i.e., with applicator and cut-out in place and corresponding jaw opening while the following rows present results for electrons beams.

Field Size (cm^2)	Energy	Solid water top (cm)	Solid water bottom (cm)	SNR	CNR	Contrast (%)	f50 (lp $mm^{-}1$)
5 × 5	6 MV	0	0	721	197	29.4	0.4
10 × 10	6 MV	0	0	769	185	29.4	0.45
20 × 20	6 MV	0	0	811	172	23.7	0.4
10 × 10	6 MeV	0	0	31.9	4.8	16.1	0.4
10 × 10	9 MeV	0	0	60.4	5.1	8.8	0.4
10 × 10	12 MeV	0	0	125	9.4	7.8	0.45
10 × 10	16 MeV	0	0	276	9.3	3.4	0.45
10 × 10	6 MeV	2	2	22.9	3.1	14.5	0.4
10 × 10	6 MeV	2	5	22.0	3.0	14.4	0.3
10 × 10	6 MeV	5	5	21.4	2.8	13.8	0.3
10 × 10	6 MeV	10	0	20.1	2.6	13.6	0.3
10 × 10	6 MeV	10	10	16.1	1.6	10.4	0.2
5 × 5	6 MeV	0	0	27.6	4.5	17.8	0.4
20 × 20	6 MeV	0	0	42.8	2.4	5.7	0.3

5.3.3 Photon Transport in the Phantom and in the EPID

The percentage of photons and their average energy for a 6, 9, 12, and 16 MeV, (10 × 10) cm^2 beam at isocenter after various thicknesses of solid water and the portal imager up to the phosphor layer are shown in table 5–5. Table 5–5 shows that 5 cm of solid water followed by the aS500 EPID is sufficient to stop most electrons for electron beams below 12 MeV while for higher energies more solid water is needed. The images acquired with the aSi EPID under such conditions are therefore produced

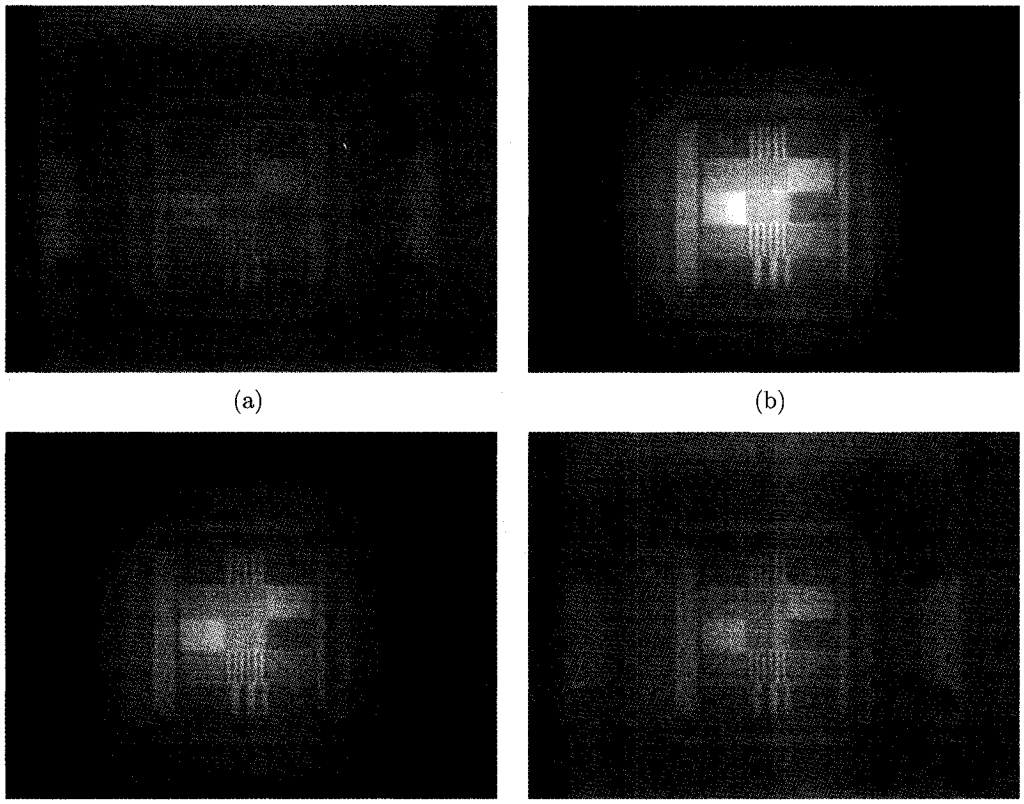

(a) (b)

(c) (d)

Figure 5–7: Measured portal images of the QC-3V phantom sandwiched between 2 slabs of 10 cm of solid water obtained with the aS500 Varian portal imager for a (10 × 10) cm^2 field at isocenter and a (a) 6 MeV, (b) 9 MeV, (c) 12 MeV, (d) 16 MeV electron beam . SSD is 96 cm and SDD is 135 cm.

only by the bremsstrahlung part of the beam. Adding solid water in the beam also affects its average energy. When solid water is added there are two main effects on the beam: low energy photons are stopped and the electron interactions produce low energy photons. In the case of a low energy electron beam (6 MeV) the first effect is dominant and the beam is hardened as solid water is added; while in the

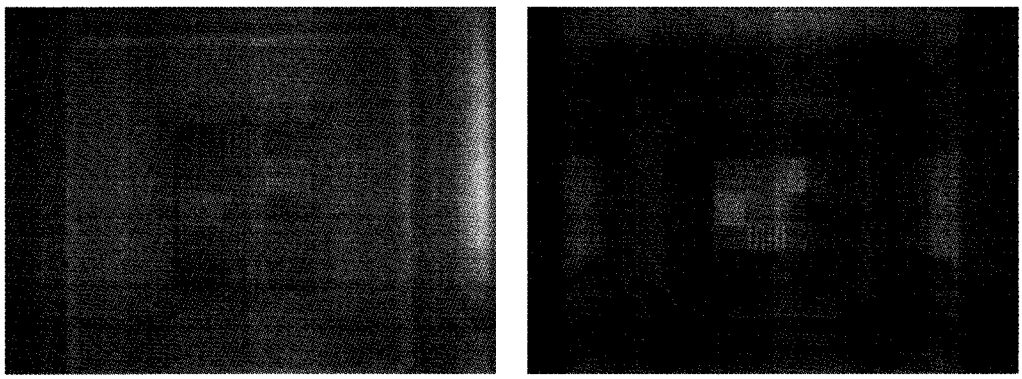

(a) (b)

Figure 5–8: Measured portal images of the QC-3V phantom sandwiched between 2 slabs of 10 cm of solid water obtained with the aS500 Varian portal imager for (a) a 6 MeV electron beam and a (20 × 20) cm^2, (b) (5 × 5) cm^2 field. SSD is 96 cm and SDD is 135 cm.

case of higher energy beams the second effect is dominant when less than 5 cm of solid water is present and so the average energy first decreases. Figure 5–10 shows the contribution of the electrons and of the photons in a simulated image of the QC-3V phantom with no additional solid water obtained for a 16 MeV beam and a (10 × 10) cm^2 beam at isocenter. It demonstrates that if an insufficient thickness of material is present in the beam, the electrons will contribute to the image. The electrons are a source of noise and thus, to increase the image quality it is important to make sure that only photons are reaching the detector. Moreover, ensuring that a sufficient amount of attenuation material is in the beam will reduce the risks of over-exposing the portal imager.

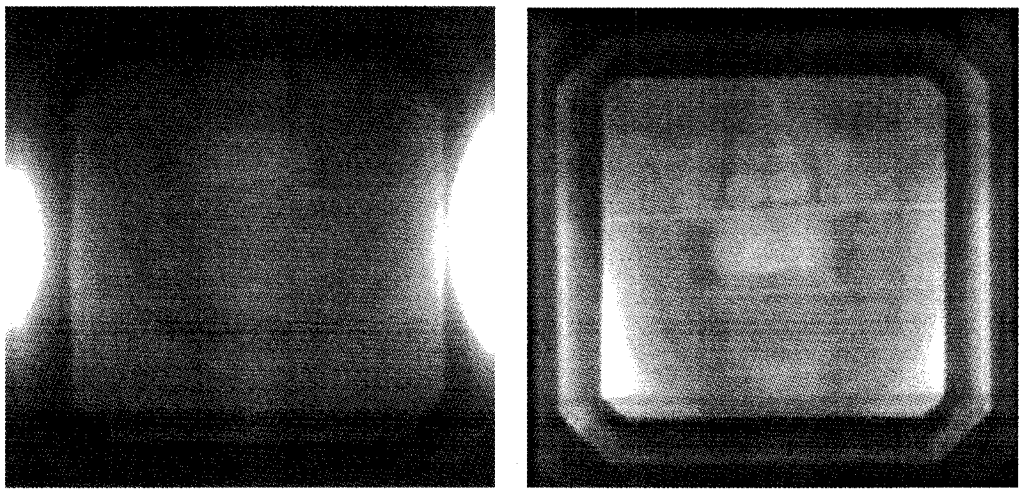

(a) (b)

Figure 5–9: Measured portal images of the head of Rando obtained with the aS500 Varian portal imager for (a) a 9 MeV, (10 × 10) cm^2 electron beam and (b) a 6 MV, photon beam using a 9 MeV electron beam configuration. SSD is 100 cm and SDD is 140 cm.

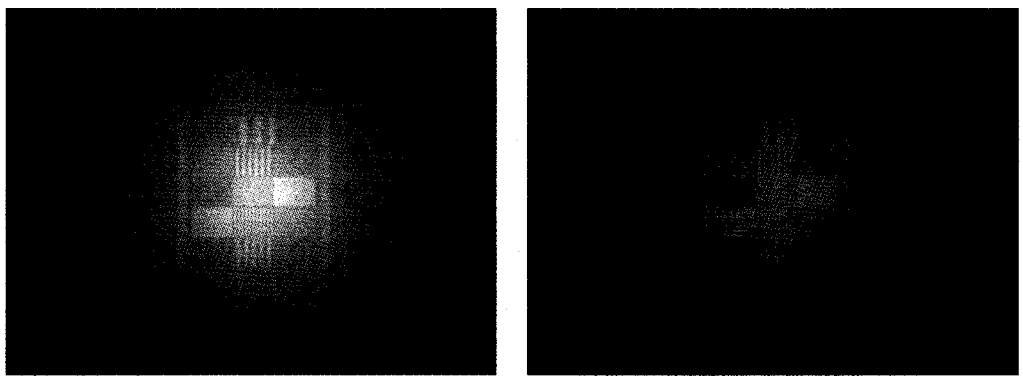

(a) (b)

Figure 5–10: Simulated images of the QC-3V phantom for a 16 MeV electron beam, (10 × 10) cm^2 field at isocenter, 98 cm SSD, 121 cm SDD and no additional solid water, image formed with (a) all particles and (b) photons.

Table 5–5: Percentage of photons in the electron beam and photon average energy after various thicknesses of solid water (SW) and the active layer of the aSi EPID for a 6, 9, 12, 16 MeV beam and a (10 × 10) cm^2 cut-out and applicator.

	Percentage of photons (%)				Average energy of photons (MeV)			
Energy (MeV)	6	9	12	16	6	9	12	16
0 cm SW	62.2	64.8	69.2	76.8	1.0	1.5	1.9	2.4
5 cm SW	99.5	99.3	98.2	89.0	1.1	1.5	1.8	2.1
10 cm SW	99.5	99.3	99.1	98.9	1.2	1.5	1.9	2.2
15 cm SW	99.5	99.3	99.1	98.8	1.2	1.5	1.9	2.3
20 cm SW	99.4	99.2	99.0	98.8	1.3	1.7	2.1	2.6

5.3.4 Comparison of Measurements and Simulations

Figure 5–11 and 5–12 respectively show the simulated and measured images of the QC-3V and Rando phantom as well as profiles through the images. The measured and simulated images are presented for a 12 MeV beam and a (10 × 10) cm^2 applicator and cut-out. The profiles were taken through the contrast media in the QC-3V phantom and through the center of the head of Rando as shown in figure 5–11 and 5–12. The pixels in the simulations and measurements were grouped 8 × 8 to reduce the statistical uncertainty to less than 2%. The profiles through the QC-3V phantom and through the Rando phantom agree within 5% expressed as local differences. Similar agreement was obtained for the 6, 9 and 16 MeV beam. Obtaining good agreement between the simulated and measured images is of importance as the MC images can then be used as references images to verify the treatment delivery. The measured and simulated images allow for a verification of the phantom positioning by making sure that the structure edges are well aligned.

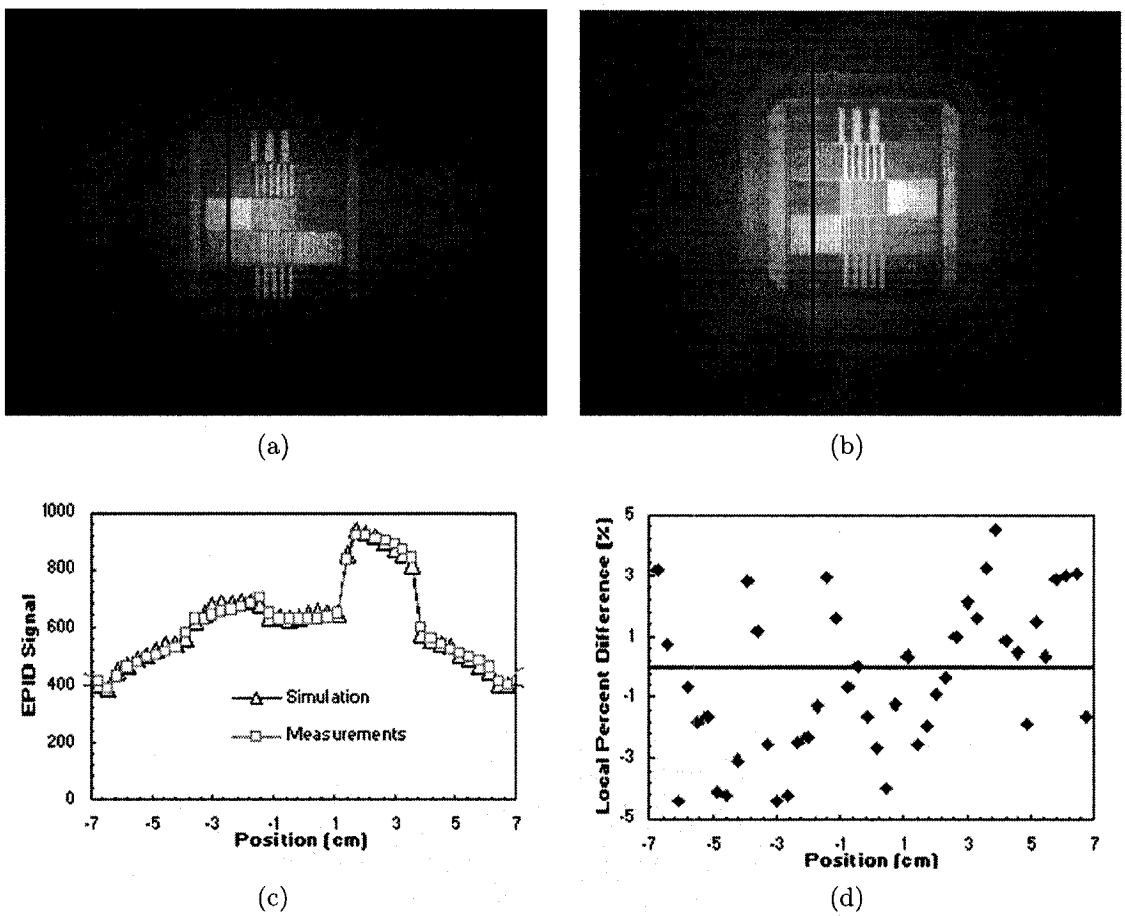

Figure 5–11: (a) Measured and (b) simulated images of the QC-3V phantom obtained with a 12 MeV electron beam, (10 × 10) cm^2 applicator and cut-out sizes, 98 cm SSD and 121 cm SDD. Corresponding (c) profiles of the detector signal and (d) local percent difference between measurements and simulations. The local percent difference is defined as the difference between measurement and simulation divided by the measurement for a given position. The position of the profile is indicated by the bar in (a) and (b).

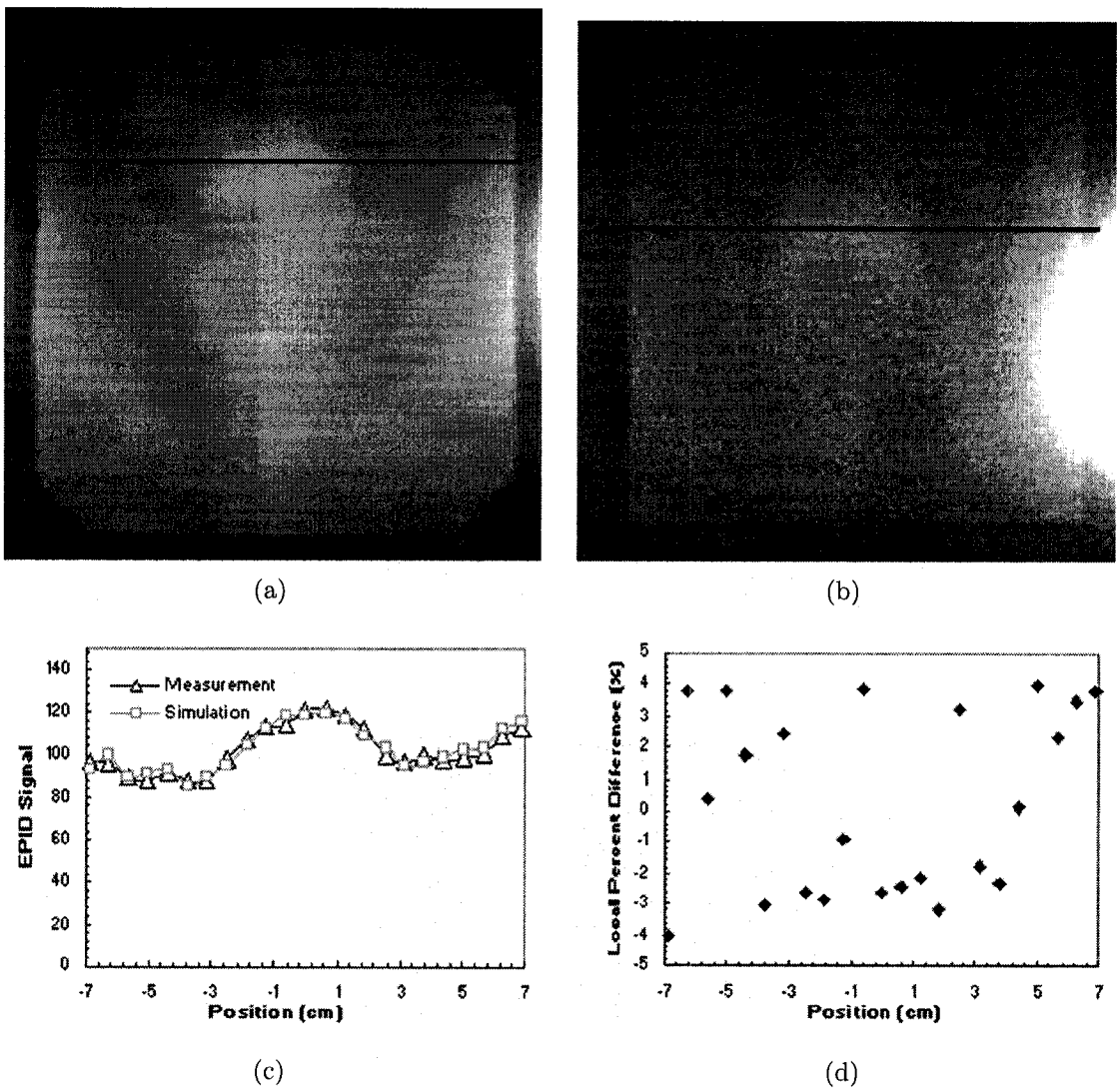

Figure 5–12: (a) Measured and (b) simulated images of the head of the Rando phantom obtained with a 12 MeV electron beam, (10 × 10) cm^2 applicator and cut-out sizes 100 cm SSD and 140 cm SDD. Corresponding (c) profiles of the detector signal and (d) local percent difference between measurements and simulations. The local percent difference is defined as the difference between measurement and simulation divided by the measurement for a given position .The position of the profile is indicated by the bar in (a) and (b).

5.4 Conclusion

In this paper, MC simulations have been used to investigate the production of bremsstrahlung photons in clinical electron beams flattened by scattering foils and to study how this production is affected by different factors such as the beam energy, the applicator and the cut-outs. It was shown that the factors that affect the beam also have an impact on the image quality. It was possible to obtain measured images with adequate contrast and resolution under various conditions which resemble clinical conditions. A preliminary study also showed that it is possible to predict the portal images using MC simulations. In the future, these predictions could be compared to the actual portal image during electron beam treatments to ensure that the treatment was delivered as planned.

5.5 Clinical Application of Electron Beam Treatment Verification

The paper presented above described and validated a technique to acquire portal images of patients using an electron beam; however no clinical cases were described. After publication of the manuscript, the method described above was applied to head and neck cancer patients. At the MGH head and neck cancer patients that are not fit for IMRT treatments receive a combination of photon and electron beam treatments. The photon treatment consists in two lateral fields and one anterior field giving a significant radiation dose to the spinal cord. The electron component of the treatment is referred to as a boost. It is used to supplement the dose to the nodes while sparing the spinal cord. It is delivered using two lateral fields delineated with patient specific cut-outs. Adequate patient positioning during the electron boost is essential to ensure that a minimal dose is delivered to the cord.

Figure 5–13 shows left and right lateral portal images of a patient treated for a head and neck cancer. The portal images in (a) and (c) were acquired using a 6 MV photon beam and the images in (b) and (d) were acquired during the patient electron beam treatment. Typical photon verification images consist in an open field and a superimposed collimated field. The photon portal images shown in figure 5–13 were acquired with an open field; the cut-out shape was delineated. The photon portal image was acquired with a 6 MV photon beam, 400 MU/min dose rate. The image was averaged over 4 frames and the SDD was set to 150 cm. The electron beam portal images were acquired using a 9 MeV electron beam, they were averaged for 50 frames to improve the SNR. The dose rate was set to 400 MU/min and the portal imager was 150 cm from the source. On both the photon and the electron images the contours of the patient head and neck are clearly visible. It is also possible to distinguish part of the patient shoulder (which is brighter) in the collimated field for both types of portal images. The contour of the head and the neck and the shoulder are anatomical landmarks that can be used to determine if the patient is positioned correctly. The portal images acquired using the electron beam display the same anatomical markers as the photon portal images and therefore can be used to position the patient.

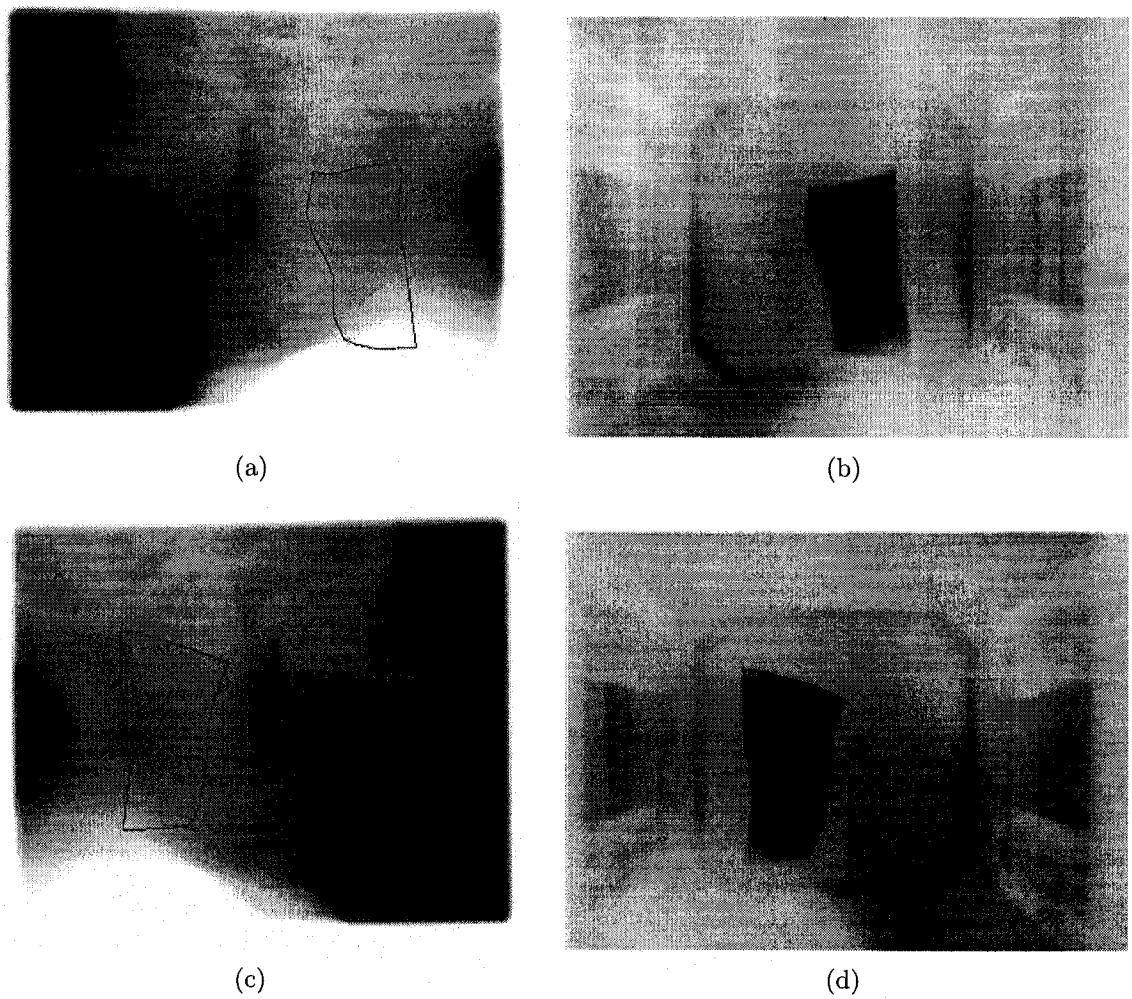

Figure 5–13: Portal images of a head and neck cancer patient acquired with (a)(c) a 6 MV photon beam (4 averaged frames) and (b)(d) a 9 MeV electron beam (50 averaged frames). A (a)(b) left lateral and (c)(d) a right lateral field are presented, images were acquired at 150 cm SDD and 400 MU/min dose rate.

In this chapter, we presented how the bremsstrahlung photons in an electron beam can be used to produce portal images during electron beam treatments. The MC simulations gave information on the bremsstrahlung production that could not have been obtained otherwise. The portal images acquired during the electron beam treatments were shown to have sufficient image quality to be used to detect if the patient is positioned correctly. Not all electron beam treatments may benefit from portal imaging but treatments that target structures that are at a certain depth or that aim at sparing radio-sensitive organs can certainly benefit from patient positioning verification. The work presented was only concerned with patient positioning; dose verification is an aspect that has not been investigated in the case of electron beam treatments. Although comparing predicted and measured portal images as suggested in section 5.3.4 may give an indication of the treatment delivery; the nature of electron beams (short range, numerous interactions) makes accurate dose verification almost impossible. However, in the case of photon beam treatments online dose verification using portal imaging is definitely possible. In the next chapter a novel method of dose verification based on MC simulations will be presented.

References

[1] Verhey L V, Goitein M, McNulty P, Munzenrider J E, and Suit H D. Precise positioning of patients for radiation therapy. *Int. J. Radiat. Oncol. Biol. Phys.*, 8:289–294, 1982.

[2] Antonuk L E. Electronic portal imaging devices: a review and historical perspective of contemporary technologies and research. *Phys. Med. Biol.*, 47:R31–R65, 2002.

[3] Karlsson M G, Karlsson M, and Zackrisson B. Intensity modulation with electrons: calculations, measurements and clinical applications. *Phys. Med. Biol.*, 43:1159–1169, 1998.

[4] Hogstrom K R, Antolak J A, Kudchadker R J, Ma C M, and Leavitt D D. Modulated electron therapy. In *The state of the art Medical Physics monograph No.29.* Medical Physics publishing, Madison,WI, 2003.

[5] Al-Yahya K, Hristov D, Verhaegen F, and Seuntjens J. Inverse Monte Carlo based modulated electron beam treatment planning based on a few leaf electron collimator - feasibility study. *Phys. Med. Biol.*, 50:847–857, 2005.

[6] Rustgi S N and Rodgers J E. Analysis of the bremsstrahlung components in 6-18 MeV electron beams. *Med. Phys.*, 14:884–888, 1987.

[7] Zhu T C, Das I J, and Bjarngard B E. Characteristics of bremsstrahlung in electron beams. *Med. Phys.*, 28:1352–1358, 2001.

[8] Keller B E. Electron-beam radiographs. *Radiology*, 128:830–831, 1978.

[9] Gur D, Weiser J C, Deutsch M, Furhrman C R, Gennari R C, and Rosenthal M S. Verification of electron beam therapy with conventional and storage phosphor images: preliminary experience. *Int. J. Radiat. Oncol. Biol. Phys.*, 17:1337–1340, 1989.

[10] El-Mohri Y, Antonuk L E, Yorkston J, Jee K W, Maolinbay M, Lam K L, and Siewerdsen J H. Relative dosimetry using active matrix flat-panel imager (AMFPI) technology. *Med. Phys.*, 26:1530–1541, 1999.

[11] Greer P B and Popescu C C. Dosimetric properties of an amorphous silicon electronic portal imaging device for verification of dynamic intensity modulated radiation therapy. *Med. Phys.*, 30:1618–1627, 2003.

[12] Siebers J V, Kim J O, Ko L, Keall P J, and Mohan R. Monte Carlo computation of dosimetric amorphous silicon electronic portal images. *Med. Phys.*, 31:2135–2146, 2004.

[13] McCurdy B M C, Luchka K, and Pistorius S. Dosimetric investigation and portal dose image prediction using an amorphous silicon electronic portal imaging device. *Med. Phys.*, 28:911–924, 2001.

[14] Spezi E and Lewis D G. Full forward Monte Carlo calculation of portal dose from MLC collimated treatment beams. *Phys. Med. Biol.*, 47:377–390, 2002.

[15] McNutt T R, Mackie T R, Reckwerdt P, and Paliwal B R. Modeling dose distributions from portal dose images using the convolution/superposition method. *Med. Phys.*, 23:1381–1392, 1996.

[16] Grein E E, Lee R, and Luchka K. An investigation of a new amorphous silicon electronic portal imaging device for transit dosimetry. *Med. Phys.*, 29:2262–2268, 2002.

[17] Jarry G and Verhaegen F. Modeling of an aSi EPID using forward and inverse Monte Carlo techniques and its applications in patient dosimetry. *Proceedings of the 8th International Workshop on Electronic Portal Imaging*, pages 34–35, 2004.

[18] Baus W and Vetterli D. Electron beam verification using electronic portal imaging - test of a commercial a-Si based system. *Proceedings of the 6th International Workshop on Electronic Portal Imaging*, page 64, 2000.

[19] Aubin M, Faddegon B, and Pouliot J. Electron beam verification with an A-Si flat panel electronic portal imaging device. *Progress in Biomedical Optics and Imaging*, 3:549–557, 2002.

[20] Aubin M, Faddegon B, and Pouliot J. Clinical implementation of electron beam verification with an a-Si EPID (abstract). *Med. Phys.*, 29:1242, 2002.

[21] Hansen V N. Feasibility study of imaging head and neck electron fields using an ASi EPID. In *Proceedings of the 8th International Workshop on Electronic Portal Imaging*, Brighton,UK, June 2004.

[22] Rogers D W O, Faddegon B A, Ding G X, Ma C M, Wei J, and Mackie T R. BEAM: A Monte Carlo code to simulate radiotherapy treatment units. *Med. Phys.*, 22:503–524, 1995.

[23] Verhaegen F, Mubata C, Pettingell J, Bidmead M, Rosenberg I, Mockridge D, and Nahum A E. Monte Carlo calculation of output factors for circular, rectangular, and square fields of electron accelerators (6-20 MeV). *Med. Phys.*, 44:938–949, 2001.

[24] Huang V W, Seuntjens J, Devic S, and Verhaegen F. Experimental determination of electron source parameters for accurate Monte Carlo calculations of large field electron therapy. *Phys. Med. Biol.*, 50:779–786, 2005.

[25] Ma C-M and Rogers D W O. BEAMDP as a general-purpose utility. PIRS 0509, NRCC, 2002.

[26] Shalev S, Rajapakshe R, and Luchka K. Techniques for commissioning electronic portal imaging devices. In *Proc. XII Int. Conf. on the use of computers in radiation therapy*, 1997.

[27] Bushberg J T, Seibert J A, Leidholdt E M, and Boone J M. *The essential physics of medical imaging.* Williams and Wilkins, Baltimore, 1994.

[28] Pang G and Rowlands J A. Electronic portal imaging with an avalanche-multiplication-based video camera. *Med. Phys.*, 27:676–684, 2000.

[29] Rajapakshe R, Luchka K, and Shalev S. A quality control test for electronic portal imaging devices. *Med. Phys.*, 23:1237–1244, 1996.

[30] Spezi E, Lewis D G, and Smith C W. Monte Carlo simulation and dosimetric verification of radiotherapy beam modifiers. *Phys. Med. Biol.*, 46:3007–3029, 2001.

[31] Walters B, Kawrakow I, and Rogers D W O. DOSXYZnrc users manual. PIRS 794revB, NRCC, 2004.

[32] Kim J O Ko L and Siebers J V. Investigation of the optimal backscatter for an aSi electronic portal imaging device. *Phys. Med. Biol.*, 49:1723–1738, 2004.

[33] Munro P and Bouius D C. X-ray quantum limited portal imaging using amorphous silicon flat-panel arrays. *Med. Phys.*, 25:689–702, 1998.

[34] Antonuk L E, El-Mohri Y, Huang W, Jee K W, Siewerdsen J H, Maolinbay V E, Scarpine V E, Sandler H, and Yorkstone J. Initial performance evaluation of an indirect-detection, active matrix flat panel imager (AMFPI) prototype for megavoltage imaging. *Int. J. Radiat. Oncol. Biol. Phys.*, 42:437–454, 1998.

[35] Attix F H. *Introduction to radiological physics and radiation dosimetry.* Wiley, New York, 1986.

[36] Sheikh-Bagheri D and Rogers D W O. Monte Carlo calculation of nine megavoltage photon beam spectra using the BEAM code. *Med. Phys.*, 29:391–402, 2002.

[37] Mohan R, Chui C, and Lidofsky L. Energy and angular distributions of photons from medical accelerators. *Med. Phys.*, 12:592–597, 1985.

[38] Reinstein L E, Amols H I, Biggs P J, Droege R T, Filimonov A B, Lutz W R, and Shalev S. Radiotherapy portal imaging quality. Technical Report 24, AAPM, 1987.

CHAPTER 6
Dosimetric Verification of Photon Beam Radiotherapy using Dose Reconstruction

An important aspect of treatment verification is dosimetric verification. Portal images contain information on the dose delivered to the patient during the treatment. In photon beam radiotherapy different techniques have been explored to extract this information and reconstruct the dose delivered to the patient. In this chapter, we present a paper submitted to *Physics in Medicine and Biology*, which describes a new dose verification technique based on portal imaging and Monte Carlo simulations. In the last section of the chapter, we discuss the performance of the dose verification technique in the case of an IMRT plan delivered to the lung of an anthropomorphic phantom.

Title: Patient specific dosimetry of conventional and intensity modulated radiation therapy using a novel full Monte Carlo phase space reconstruction method from electronic portal images

Authors: G Jarry and F Verhaegen

Accepted for publication in Physics in Medicine and Biology; March st 2007

Abstract

Electronic portal imagers have promising dosimetric applications in external beam radiation therapy. In this study a patient dose computation algorithm based on Monte Carlo (MC) simulations and on portal images is developed and validated.

The patient exit fluence from primary photons is obtained from the portal image after correction for scattered radiation. The scattered radiation at the portal imager and the spectral energy distribution of the primary photons are estimated from MC simulations at the treatment planning stage. The patient exit fluence and the spectral energy distribution of the primary photons are then used to ray-trace the photons from the portal image toward the source through the CT geometry of the patient. Photon weights which reflect the probability of a photon being transmitted are computed during this step. A dedicated MC code is used to transport back these photons from the source through the patient CT geometry to obtain patient dose. Only Compton interactions are considered. This code also produces a reconstructed portal image which is used as a verification tool to ensure that the dose reconstruction is reliable. The dose reconstruction algorithm is compared against MC dose calculation (MCDC) predictions and against measurements in phantom. The reconstructed absolute absorbed doses and the MCDC predictions in homogeneous and heterogeneous phantoms agree within 3% for simple open fields. Comparison with film-measured relative dose distributions for IMRT fields yields agreement within 3 mm, 5 %. This novel dose reconstruction algorithm allows for daily patient-specific dosimetry and verification of patient movement.

6.1 Introduction

Recent improvements in dose delivery techniques have rendered it possible to paint the dose exactly to the tumor volume [1, 2] while improvements in computation techniques such as Monte Carlo (MC) simulations have made it possible to compute accurately the dose given to the tumor and the surrounding organs [3–5].

The limitations of radiation therapy are now in defining the tumor volume and in verifying that the dose has been properly delivered. The treatment conformity makes dose verification essential as improper dose delivery can potentially compromise clinical results by insufficient dose coverage of the target volume and/or over dosage to normal tissues [6–8]. Dose delivery verification can be accomplished by doing pre-treatment verification or by taking in-vivo measurements during the treatment. In the case of intensity modulated radiation therapy (IMRT), the reproduction of a single patient treatment fraction on a phantom has become the norm for pre-treatment dose verification of the combined beam delivery and treatment planning dose calculation [9]. Dose measurements can be done in phantom at one point using an ion chamber and in a plane using film. The former measurement puts the verification on an absolute basis while the latter verifies the dose distribution relative to this point. In-vivo dose verification during treatment can be done by placing dosimeters such as diodes, thermoluminescence dosimeters (TLDs) or metal oxide semiconductor field effect transistors (MOSFETs) on the patient skin or inside patient cavities. These measurements are limited to point measurements and increase the treatment time.

In recent years, electronic portal imaging devices (EPIDs) have demonstrated interesting possibilities for dosimetric verification of conventional and IMRT treatments. Many different types of EPIDs have been considered for dosimetry [10–18]. The amorphous silicon (aSi) type is generally recognized as being the best suited for dosimetric purposes [17, 18]. It has a linear response to dose and dose rate and it is stable with time [17]. The aSi system can acquire images in real-time at a high frame rate which is essential for IMRT verification. It was also demonstrated that the aSi

EPID signal can be calibrated in terms of absolute absorbed dose. Grein *et al* [18] obtained a relationship between dose and aSi EPID pixel value by comparing the EPID signal and ion chamber readings taken with a sufficient amount of solid water for buildup. They found a linear relationship between EPID signal and ion chamber readings which holds for different detector distances and field sizes. Siebers *et al* [19] chose a MC approach in which measured and simulated flood fields are used to obtain a pixel-by-pixel calibration matrix. This calibration can be used to transform EPID signal to EPID dose.

There are two main approaches to portal imaging dosimetric verification: (i) comparison of a predicted fluence or dose at the detector with a portal image acquired during the treatment [15, 16, 20, 21] and (ii) reconstruction of the dose in the patient from the portal image [22–28]. The first technique has mostly been used in pre-treatment verification. It can only indicate if the field sequence was delivered correctly, and does not calculate the actual dose delivered to the patient. Different approaches have been explored for dose reconstruction. McNutt *et al* [22] proposed to use an iterative convolution/superposition algorithm to reconstruct the dose distribution in patients. Steciw *et al* [27] used extracted fluence profiles from the EPID and a treatment planning system to obtain three-dimensional doses. Wendling *et al* [26] adapted the technique developed by Boellaard *et al* [24] and Louwe *et al* [29] for IMRT deliveries. The technique uses back-projection of primary fluence and pre-calculated scatter dose in phantom to obtain the dose delivered to the patient. The technique was shown to work for IMRT fields in homogeneous phantoms. Another approach based on back-projection is to ray-trace the primary fluence at the

detector through a CT of the patient; an inverse attenuation correction is used to obtained an input fluence between the patient and the linear accelerator [25]. The primary fluence at the detector is obtained by correcting for scatter radiation using pre-calculated kernels. The back-projected input fluence is then used to calculate the patient dose using a convolution/superposition method [25]. Most dose reconstruction techniques are limited when non-homogeneous phantoms are used since they rely on pre-calculated kernels in homogeneous water. Van Elmpt *et al* [28] used this same back-projection technique to develop an IMRT pre-treatment verification tool where the dose is calculated in a phantom using MC simulations. Their method requires an image acquired before the treatment without the patient or phantom in the beam. Hence, it is impossible to detect errors that occur during the delivery such as leaf position errors. Dose reconstruction techniques usually require a primary fluence map at the portal imager. Methods based on pre-calculated scatter radiation kernels [23] or using lateral scatter measurements [26] have been used to obtain the primary fluence.

It is well accepted that although MC simulations are computationally intensive and not widely available in the clinic yet, they offer the most advanced and accurate techniques for radiotherapy treatment planning. Such methods can take into account an accurate and complete representation of the patient anatomy. Recently, MC simulations have been used to model portal imagers. The MC models were used to predict portal images [19, 20, 30, 31] and to study the image formation process [32]. MC simulations were shown to predict reliably portal images of conventional photon and electron beams and IMRT fields. To our knowledge MC simulations have not

been used to correct for scatter radiation at the portal imager and obtain primary fluences.

In this study, we develop a new technique that uses the accuracy of MC calculations to reconstruct dose from an aSi portal image for a 6 MV photon beam. MC simulations allow an accurate calculation of the dose in highly inhomogeneous regions. The dose reconstruction technique is patient specific and allows a verification of the radiation dose delivered for every treatment fraction. The method is based on MC simulations both for the prediction of the primary fluence at the detector and for the patient calculations. Although a previous study has used MC simulations to reconstruct the dose to phantom [28], the method was based on an image acquired prior to treatment and hence day-to-day delivery errors were not taken into account. Similarly to all dose reconstruction techniques based on portal imaging, the approach presented here is limited when patient motion occurs and would perform best if a three-dimensional image of the patient was acquired before every dose delivery. However, our method includes a reconstructed and measured portal image comparison which can be used to estimate the accuracy of the dose reconstruction process and detect important patient or organ movement. This extra validation was not designed to quantify the patient motion but can be very useful when no CT information on the day of the treatment is available as a tool to evaluate the accuracy of the dose reconstruction. In the next sections, the dose reconstruction algorithm will be described in detail and the outcome of validation tests on phantoms for both conventional and IMRT fields will be presented.

6.2 Materials and Methods

6.2.1 Experimental Set-up

The conventional and IMRT measurements presented in this study are obtained with a Varian CL21 EX linear accelerator (linac) equipped with an aS500 EPID. The aS500 EPID is an indirect detection system which consists of a 1 mm copper plate overlying a scintillating layer of phosphor (gadolinium oxysulfide) and a (40×30) cm^2 $((512 \times 384)$ pixels$^2)$ aSi light sensor photo diode array. The dose measurements in phantom were performed using Kodak EDR2 films only; no ion chamber measurements were performed since only relative doses were considered. The films were inserted between two slabs of solid water providing 6 cm of buildup material and 11 cm of backscatter material. Films were developed with a Kodak RPX-Omat processor and digitized using an ArgusII AGFA scanner with 16 bit depth and 127 dpi resolution, resulting in a (0.02×0.02) cm^2 pixel size. The film calibration curve was obtained by exposing films to different levels of dose and plotting the relative levels of dose versus the scanner transmission values.

6.2.2 Dose Reconstruction Method

The dose reconstruction algorithm uses the information stored in the electronic portal image to obtain dose to the patient for each fraction. The algorithm is optimized for 6 MV photon beams. Figure 6–1 is a schematic diagram of the dose reconstruction algorithm. The algorithm can be split in four main steps: the MC dose calculation, the portal image processing, the MC phase space reconstruction and the MC dose and portal image reconstruction. The following sections will describe the different steps in more detail.

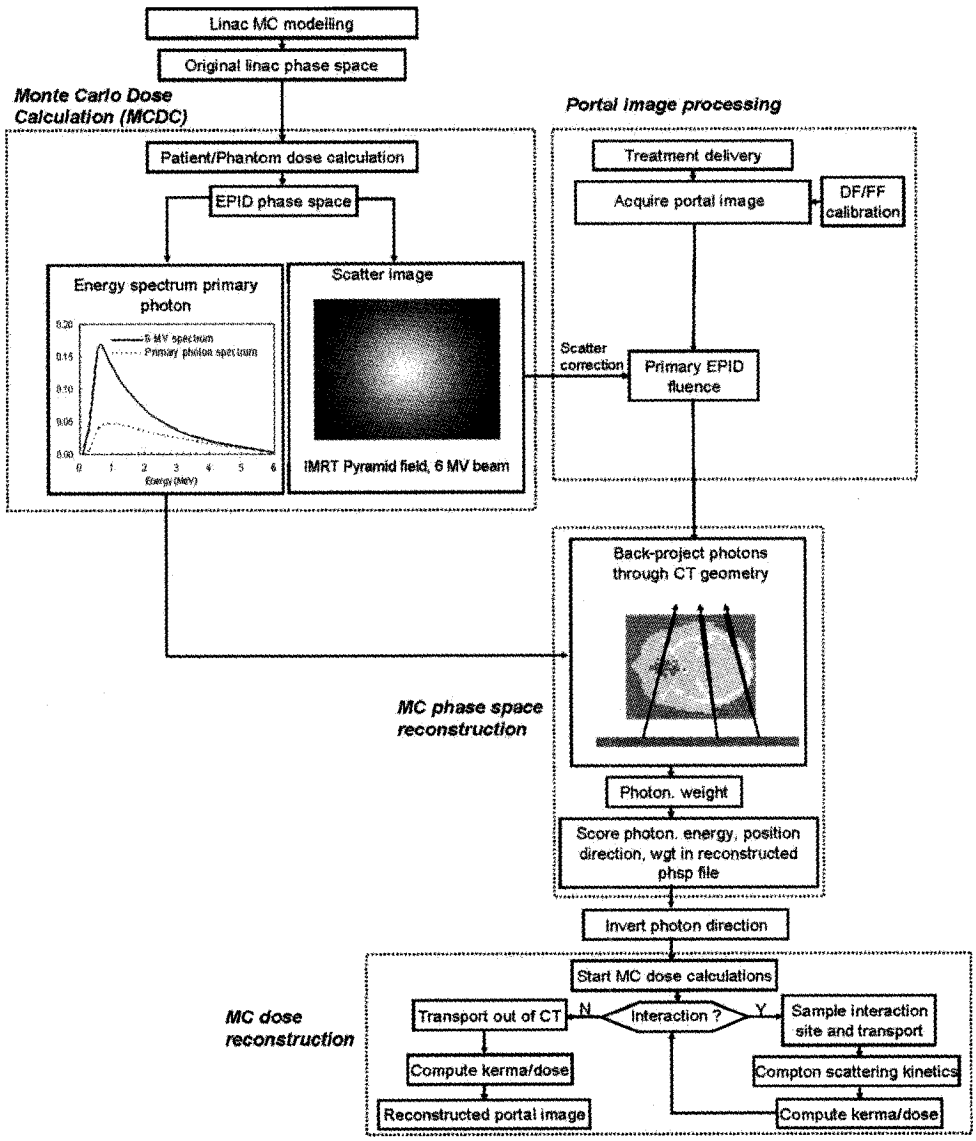

Figure 6–1: Schematic diagram of the dose reconstruction algorithm process, including the primary photon spectrum at the EPID for the head of an anthropomorphic phantom and the portal image produced by the scattered photons in a 20 cm thick water phantom for a pyramidal IMRT field.

Monte Carlo dose calculation and beam modeling. Monte Carlo dose calculations (MCDC) are used to compute the dose to the phantoms as well as to produce portal images and energy spectra at the portal imager plane. The BEAMnrc MC code system [4] was used to build a linear accelerator model of the Varian CL21EX linac according to the manufacturer's specifications. The model includes the DYNVMLC component module developed at our institution [33]. A beam energy of 6 MV was modeled. The photon and electron transport cut-offs were set to 0.01 MeV and 0.700 MeV, respectively. Validation of the accelerator model was performed by comparing measured and simulated percent depth dose (PDD) curves in water and profiles in water and in air for different field sizes. The local percent differences calculated between the PDDs are within 2% with a statistical uncertainty of 1% on the MC simulations. Profiles agree within 2% or 2 mm. Original linac phase space files for the different fields are scored at 100 cm from the source with a least 100 000 particles/cm^2 which ensured an uncertainty smaller than 2% on the quantities derived from that phase space. The DOSXZYnrc program [34] which is part of the EGSnrc MC code package was modified to obtain a phase space file at the EPID (denoted EPID phase space in figure 6–1) behind the dose scoring geometry in which primary and scattered photons [35] are identified. The modified DOSXZYnrc program is also used to compute dose in various voxelized geometries. The number of sampled particles from the original linac phase space file is made sufficiently high so that the statistical uncertainty on the phantom dose and EPID phase space calculations is up to 2 %. EPID phase space files are used to obtain a spectrum of the primary photons. As an illustration, the spectrum of the primary

photons behind the head of an anthropomorphic phantom is found in figure 6–1. An analytical program [35] that utilizes a dose response function from a complete MC model of the EPID is used to transform the EPID phase space files into dose deposition in the EPID sensitive layer. Details of the EPID MC model were presented previously in Jarry and Verhaegen [30]. The dose response function was obtained by scoring the dose per unit fluence in the gadolinium oxysulfide layer of the detector, assuming the response of the light sensor is proportional to the energy deposition in the phosphor [36, 37]. The following calibration step (equation 6.1) is used to transform the dose to the sensitive layer into an EPID signal. A given MC computed dose to the sensitive layer (D_{MC}) is transformed to the corresponding EPID signal ($\mathrm{EPID}_{\mathrm{MC}}$) by multiplying it by a ratio of measured EPID signal for flood field ($\mathrm{F}_{\mathrm{meas}}$) to a MC computed dose for the same flood field (F_{MC}) for each pixel (i, j).

$$\mathrm{EPID}_{\mathrm{MC}}(i,j) = D_{\mathrm{MC}}(i,j) \times \frac{F_{\mathrm{meas}}(i,j)}{F_{\mathrm{MC}}(i,j)} \tag{6.1}$$

A simulated portal image of the scatter signal for a pyramidal IMRT field can be found in figure 6–1.

Portal image processing. An integrated electronic portal image contains information on the photon fluence at the detector and on the amount of radiation delivered to the patient. Various steps are required to extract the primary EPID fluence from the portal image. One portal image must be acquired for each delivered field. In the case of IMRT, a field is defined as the sum of the individual beamlets for one gantry angle. Since the portal images are an average of many frames that were

acquired during the treatment delivery, they must be multiplied by the number of frames acquired. The portal images must also be corrected for the difference in pixel gain and offset values. This procedure has been described in great length [17, 19, 26] and consists in subtracting a dark field (DF) image and dividing by a flood field (FF) image.

The next step consists in extracting the primary EPID fluence from the portal image. The method developed in this study relies on MC simulations. At the MCDC stage a patient-specific portal image produced by scattered particles is generated (figure 6–1). The MC estimation of scatter relies on the fact that the scatter distribution and amplitude does not vary significantly between treatment fractions so this calculation is performed only once. The primary EPID fluence is obtained by subtracting the simulated scattered EPID image from the measured original image. Given that the energy distribution of the primary photons is fairly constant over the portal imager area, the dose is proportional to the primary EPID fluence. It was found from MC simulations that the primary photon spectrum for homogeneous phantoms does not vary significantly over the portal imager area. For a 20 cm thick water phantom and a (10×10) cm^2 field size at isocenter, a difference in average energy of up to 3% was found for a spectrum taken at the center of the portal imager compared to one at the field edge. For larger field sizes covering the complete area of the portal imager the difference in average energy was closer to 8%. In the case of non-homogeneous geometries the spectrum can vary significantly over the portal imager area. Figure 6–2 shows the difference in primary photon spectrum at the EPID for a 20 cm thick water and a 20 cm lung phantom. The spectra are significantly

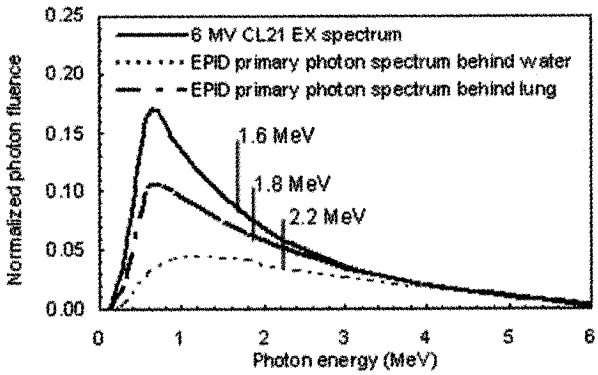

Figure 6–2: Primary photon spectrum at the EPID calculated using MC simulations for a $(20 \times 20 \times 20)$ cm^3 water phantom and a $(20 \times 20 \times 20)$ cm^3 lung phantom compared to the Varian CL21 EX spectrum obtained from a complete MC model of the accelerator. The average energy of the spectra are indicated in the graph.

different as photons from a 6 MV beam going through water will be hardened more than the photons going through lung. Although it would be easier to extract the energy fluence from the portal imager, the phase space reconstruction step requires the photon spatial and energy distribution separately.

Phase space reconstruction. In order to backproject the primary fluence information with correct weighting, the photon energy must be known. A patient-specific spectrum of the primary photons at the EPID is generated at the MCDC stage. In the case of an homogeneous phantom a single spectrum can be used for all portal imager positions. However in the case of an inhomogeneous geometry, such as the chest, dividing the portal imager in rectangular sub-sections and obtaining a spectrum for each of these sub-sections provides a better dose reconstruction. The number of sub-sections is selected by the user and is geometry dependent; it can be

based on the patient CT scan. Further investigations are required to establish guidelines relating the number of subsections required for different geometries imaged.

The phase space reconstruction step is similar to the backprojection method described by Partridge *et al* [25] except that here a patient-specific spectrum is used. Photons with position sampled from the primary fluence obtained from a processed portal image are started at the EPID position. Their energy is sampled from the EPID simulated primary photon spectrum. The photons are ray-traced back through the CT patient geometry to the linear accelerator source. The linear accelerator source is approximated to be a point source at the center of the linac target. This is an approximation as the off-focus radiation origination from the primary collimator and the flattening filter contribute 3 to 9% to the fluence in a 6 MV photon beam [38]. The CT geometry is described as a voxelized geometry where every voxel is assigned a material and density according to the CT number. During the backward ray tracing step the primary photons are attributed a weight ($\geq$1) which corresponds to their probability to be transmitted through to the source; this weight (w) is given by equation (6.2) where $\mu_i(E)$ is the total (narrow beam) attenuation coefficient for a given photon energy E and t_i is the photon path length through voxel i of the CT data:

$$w = \sum_{i=1}^{n_{\text{voxel}}} \mathrm{e}^{\mu_i(E)t_i} \tag{6.2}$$

The increasing weight with traveled path length compensates for photons that were removed from the beam by scatter and absorption. The photon information,

e.g., their position, direction (given directly by the source and the photon position), energy and weight, is stored in the reconstructed phase space file at a plane between the patient and the linac as illustrated in figure 6–1. To ensure an uncertainty on the reconstructed dose less than 2% the reconstructed phase space file should contain around 100 000 particles/cm^2.

Monte Carlo dose reconstruction. A dedicated MC code integrated in the dose reconstruction algorithm is used to transport the photons that are stored in the reconstructed phase space file back through the CT geometry. This MC code uses simplified photon transport and no electron transport. During the transport, the position of the photon interaction is sampled using attenuation coefficients. Only Compton interactions are considered which is an acceptable approximation given the energy range of the photons in a 6 MV beam and the patient tissue composition. A rejection sampling method is used to sample the Compton cross-section and to obtain the scattered photon energy and angle [39]. The photons are transported until they exit the geometry or their energy drops below a cut-off set by the user. Kerma can be calculated and absorbed dose can be estimated. The kerma computations are based on a track length estimate. The track length estimates the fluence of the photons which can be converted to collision kerma by multiplying it by the photon energy and the mass-energy absorption coefficient [40]. The dose is obtained by multiplying the kerma with pre-calculated collision kerma to dose conversion factors. These factors were generated using MC simulations (EGSnrc code) for different depths in water and monoenergetic broad beams. The conversion factors were obtained for water only; the assumption is made that the first centimeters of a patient or a phantom

are water equivalent and that past that initial region the collision kerma is equal to absorbed dose since charged particle equilibrium is achieved for most media.

Reconstructed portal image and absolute dose computation. After the MC transport of the photons through the dose scoring geometry, the photon information is used to produce a reconstructed portal image. The portal image is obtained using the same analytical program described in section 6.2.2. The analytical program is included in the dose reconstruction algorithm. This reconstructed portal image should be identical to the actual portal image if the dose reconstruction was performed correctly. A comparison of the actual portal image and the reconstructed portal image using the planning CT will detect to some extent if there was patient motion or change in patient geometry between the treatment planning and the dose delivery. In addition, the two images acquired for a static phantom can be used for quality assurance testing on the dose reconstruction algorithm. If the dose algorithm is performing as it should and no beam delivery error occurred the two images should be identical for static phantoms.

The dose scored during the dose reconstruction process, if not processed further, will be a dose in units of Gy per initial simulated particle. In order to obtain an absolute dose in units of Gy to the patient, the following procedure was added to the dose reconstruction algorithm. The procedure requires the MC reconstructed and actual portal images. The measured EPID ($EPID_{meas}$) signal in arbitrary units (A.U.) is transformed to dose delivered to the EPID using the calibration procedure used by Siebers *et al* [19] and described earlier in this paper. The dose in Gy (D) is obtained by multiplying the dose in Gy per particle by a ratio of the sum of all pixel

values in the measured EPID over the sum of all pixel values in reconstructed EPID ($\text{EPID}_{\text{MC,reconst}}$). The calibration procedure is described mathematically by

$$\begin{aligned}\text{EPID}_{\text{meas}}(i,j)[\text{Gy}] = \text{EPID}_{\text{meas}}(i,j)[\text{A.U./MU}] \times \\ \frac{FF_{\text{MC}}(i,j)[\text{Gy/MU}]}{FF_{\text{meas}}(i,j)[\text{A.U./MU}]} \times \text{MU}\end{aligned} \tag{6.3}$$

and

$$D[\text{Gy}] = D[\text{Gy/particle}] \times \frac{\sum_{i,j} \text{EPID}_{\text{meas}}(i,j)[\text{Gy}]}{\sum_{i,j} \text{EPID}_{\text{MC,reconst}}(i,j)[\text{Gy/particle}]} \tag{6.4}$$

where i, j are the pixel indices and MU stands for monitor units.

6.2.3 Validation of the Dose Reconstruction Algorithm

Validation of the EPID model. The first validation step consists in ensuring that the MCDC program can accurately predict portal images since these predicted portal images will be used to obtain the EPID primary fluence. Portal images of IMRT fields were measured and simulated. The portal images were compared using a gamma index map. The gamma index combines a dose-difference criterion, or signal difference criterion in this case, with a distance-to-agreement criterion. A gamma index smaller than unity means that both distributions agree for that point [41]. This comparison method is particularly interesting in high dose gradient region where a small difference in position can lead to a large dose difference. To date, no uniform guidelines regarding the definition of tolerance criteria for quantitative evaluations in IMRT quality assurance can be found in the literature. Van Dyk *et al* [42] proposed 0.4 cm, 3% for static photon fields. Low and Dempsey [43]

suggest 0.3 cm and 5% for clinical IMRT fields. A 5% signal difference criterion was chosen. The distance criterion was set to 5 mm since Low and Dempsey [43] suggest that the pixel spacing should be less than or equal to 1/3 of the distance criterion. Although the aS500 pixel size is 0.784 mm, the pixels were grouped two by two to reduce the noise to arrive at a pixels size of 1.568 mm.

The second step consists in checking that the MC model could accurately predict the amount of scattered radiation reaching the detector. A technique described by Swindell and Evans [44] was used to validate the MC simulation of scattered radiation at the detector. A first set of images of a $(30 \times 30 \times 20)$ cm^3 solid water phantom were acquired for different field sizes. A second set of images was acquired with no solid water in the beam. The detector signal over a (12×12) pixel^2, (0.94×0.94) cm^2 array at the center of the field was averaged for all images. The average values for the first set of images were divided by the corresponding average values for the second set of images which yields a data set $ES(A)$. The variation in these values is only due to changes in phantom scatter and not due to changes in the linac output. These values are fitted as a function of the field size using a quadratic fit and the extrapolated value for zero area, $ES(0)$, is used to obtain the scatter-to-primary ratio (SPR) as shown by equation (6.5).

$$\text{SPR} = \frac{ES(A) - ES(0)}{ES(0)} \tag{6.5}$$

The simulated SPR was determined using two techniques. The SPR was first obtained using the technique described above where both sets of measurements were

simulated using the EGSnrc code. The SPR was also determined by simulating only the first set of measurements with solid water in the beam. The modified version of the DOSXYZnrc program described in section 6.2.2 was used to determine directly the amount of scattered and primary particles in the region of interest described above and the SPR was obtained from those numbers.

Validation of the dose reconstruction using Monte Carlo simulations. MCDC was used to validate the dose reconstruction method. Figure 6–3 is a schematic of how the validation was done using MC simulations. The MCDC program was used to obtain simulated portal images as described in section 6.2.2. These images were transformed to primary EPID fluence and used as input in the dose reconstruction algorithm. Various homogeneous and heterogeneous mathematical phantoms were modeled. The phantoms were made of water, bone and lung. Simple open fields of different sizes were simulated. The dose reconstruction was run for a number of particles sufficient to ensure a statistical uncertainty smaller than 1.5% of the dose maximum. The reconstructed dose was compared to the MCDC dose. The original MCDC and reconstructed portal images were compared using a ratio map.

Validation of the dose reconstruction using measurements in a phantom for IMRT fields. The dose reconstruction algorithm was further validated using phantom measurements of relative dose. The main steps of this validation process are described in fig 6–4. Treatments that had been previously planned using inverse treatment planning software were recalculated using the MCDC program for consistency.

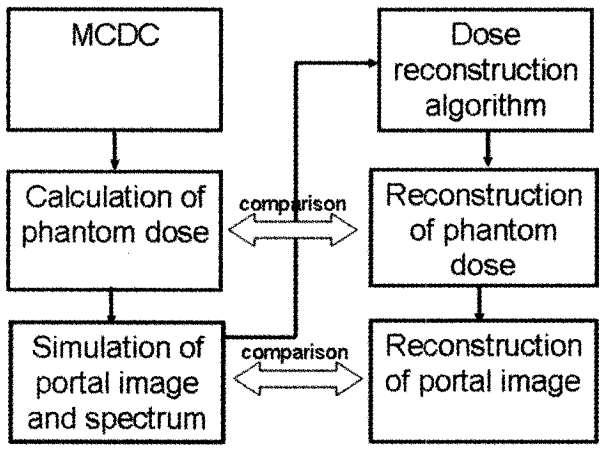

Figure 6–3: Schematic diagram of the validation steps for the dose algorithm when using MC simulations.

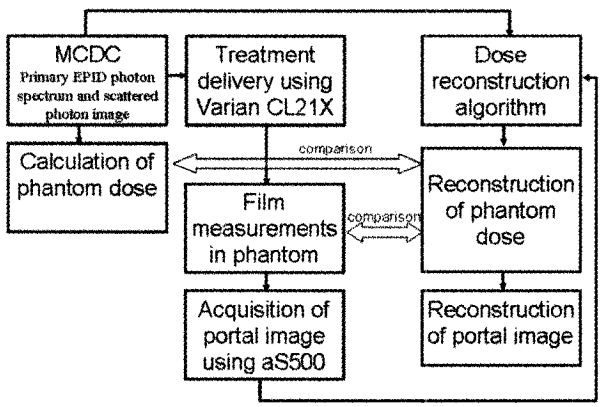

Figure 6–4: Schematic diagram of the validation steps for the dose algorithm when using MC simulations and measurements.

Three IMRT fields were delivered: a pyramid IMRT test field and two clinical IMRT fields. The clinical fields consisted in inverse planned fields for a colorectal cancer treatment at gantry angles of 40° and 180°. Kodak EDR2 films were used for the dose measurements; this type of film has been shown to be adequate for the dosimetry of IMRT fields [45]. The reconstructed dose in water was compared to the film measurements. The voxel size for the dose reconstruction was set to $(0.1 \times 0.1 \times 0.5)$ cm^3, ensuring a good resolution and minimizing the noise. The number of photons for which the dose reconstruction was run was sufficient to ensure a statistical uncertainty less than 2%. Before comparison of film and reconstructed dose the digitized film data was re-binned to obtain pixel sizes corresponding to the dose reconstruction. The measured and reconstructed doses were normalized to the dose maximum because the film doses were considered to be relative doses. A gamma map index was obtained to compare measurements and dose reconstruction. A 3 mm and 5% error and distance criteria were chosen for the dose comparison as suggested by Low and Dempsey [43] and Winkler *et al* [46].

Comparison of treatment planned dose to reconstructed dose in an anthropomorphic phantom. An anthropomorphic phantom was used to test the dose reconstruction procedure as it would be applied clinically. A treatment plan consisting of an anterior/posterior(AP) (10×10) cm^2 open field was calculated using the MCDC code. The plan was delivered to the head and the chest of an anthropomorphic phantom. The corresponding portal images were acquired. These images were processed and used as input for the dose reconstruction algorithm. The voxel size for the phantom model were set to $(0.4 \times 0.4 \times 0.6)$ cm^3 for the head and

$(0.4 \times 0.4 \times 0.8)$ cm^3 for the chest. The dose predicted by the MCDC code were compared to the reconstructed dose.

Quantifying the difference in EPID signal for organ and patient motion. Portal image predictions obtained during the dose reconstruction can be used to check for patient movement. In order to demonstrate the capability of this method, MC was used to simulate patient and organ motion. The steps involved in this demonstration are shown in figure 6–5. A water, lung and bone phantom was displaced by 1 cm or the lung part of the phantom was made smaller by decreasing its size by 1 cm on each side in the lateral direction keeping the density constant. A dose distribution and a portal image were simulated using the MCDC program after the movement was introduced. The simulated portal image obtained was used as input for the dose reconstruction with the energy spectrum and the scattered photon distribution obtained with MCDC before any motion was introduced. The dose reconstruction was performed on the original phantom with no patient or organ motion to reproduce the clinical set up where the planning CT would be used. The simulated and the dose reconstructed portal images were then compared using a ratio of the reconstructed image over the original image.

6.3 Results

6.3.1 Validation of the EPID Model

Figure 6–6 shows a comparison between measured and simulated portal images for a pyramidal IMRT field. The gamma index (0.5 cm and 5% criteria) is less than 1 for 93% of the pixels inside the field showing a good agreement between simulated and measured portal images. Reasons for discrepancies include the uncertainty in

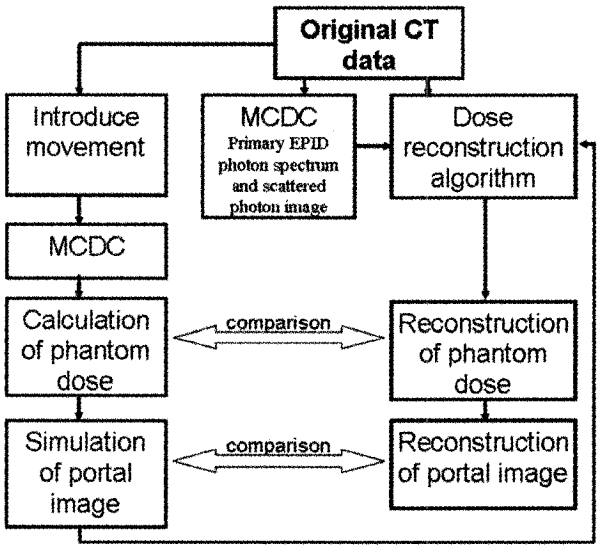

Figure 6–5: Schematic diagram of how portal images predictions can be used to verify the validity of the dose reconstruction calculations

the positioning of the portal imager and the MLC leaf movements and are mostly present in the steep dose gradient regions.

Figure 6–7 shows the simulated SPR and the measured SPR obtained using the technique described in section 6.2.3; as well as the simulated SPR obtained with the modified DOSXYZnrc program. An agreement within 4% was found between the measured SPR and the simulated SPR obtained with the modified DOSXYZnrc program which explicitly gives the number of scattered and primary particles. For the larger field size where the agreement was found to be within 8%. Given the good agreement obtained between simulated and measured portal images (figure 6–6), we would expect a better agreement of the SPR. The discrepancy is likely due to the Swindell and Evans [44] method used to evaluate the measured SPR, which assumes

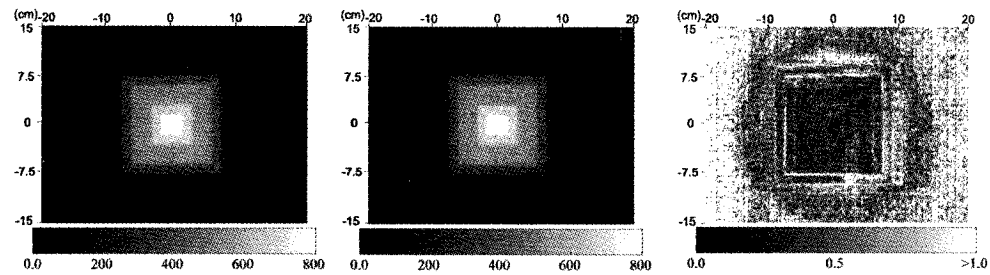

(a) (b) (c)

Figure 6–6: Comparison of (a) measured and (b) simulated portal images for a pyramidal IMRT field and (c) gamma map comparison of the two portal images with a 5%,0.5 cm criteria.

that no scatter is present for the zero field size. In fact, when this method is used to evaluate the simulated SPR, the simulated and the measured values now agree within 4% for all field sizes. Therefore, the modified DOSXYZnrc program predicts accurately the scatter amplitude at the central axis.

6.3.2 Validation of the Dose Reconstruction Using Monte Carlo Simulations

The dose reconstruction algorithm was tested for different field sizes and different simulated materials. Figure 6–8 shows the reconstructed and the MCDC central absolute depth dose curves and profiles at 2.5 cm and 6.5 cm depth from a 6 MV, (10×10) cm^2 photon beam simulated in a uniform water phantom. The mathematical water phantom is $(20 \times 20 \times 20)$ cm^3 with $(1 \times 1 \times 1)$ cm^3 voxels. The depth dose curves agree within 3% and the profiles at 2.5 cm and 6 cm depth show agreement within 3%. The most important discrepancies are observed in regions where charged particle equilibrium is not achieved, such as the buildup region and the field edges, since electron transport is not modeled. For homogeneous phantoms

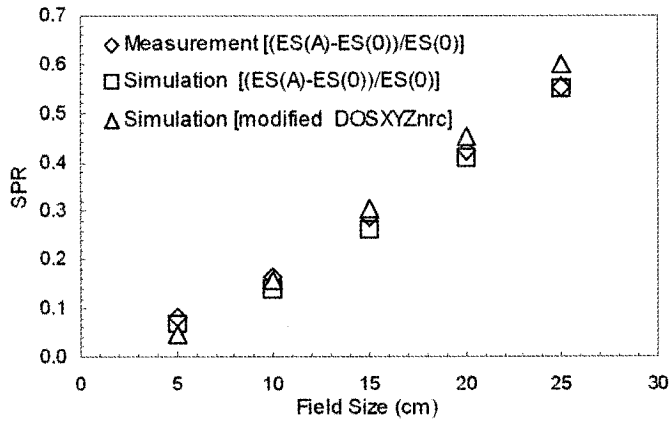

Figure 6–7: Comparison of measured and simulated scatter-to-primary ratio (SPR) as a function of field size for a (20 × 20 × 20) cm^3 water phantom. Measured SPR obtained using SPR=(ES(A)-ES(0))/ES(0), simulated SPR obtained with SPR=(ES(A)-ES(0))/ES(0) and directly with the modified DOSXYZnrc program.

and open fields the algorithm is able to backproject the photons from a portal image (in this case simulated) and to calculate a reconstructed dose to an accuracy within the statistical uncertainty of the simulations (2%).

Figure 6–9 shows a more complicated case where the irradiation of a mathematical heterogeneous phantom composed of water, lung, and bone with an open (10 × 10) cm^2, 6 MV beam is simulated. A good agreement is obtained between the MCDC absolute isodose lines and the reconstructed absolute isodose lines. Figure 6–9(b) and (d) show the reconstructed and MCDC central axis absolute depth doses and lateral profiles at 2.5, 5 and 10 cm depth for the same set-up. The dose curves agree within 3%, and the profiles agree within 4% with the largest discrepancies at the field edges. This demonstrates that the primary photons from a portal

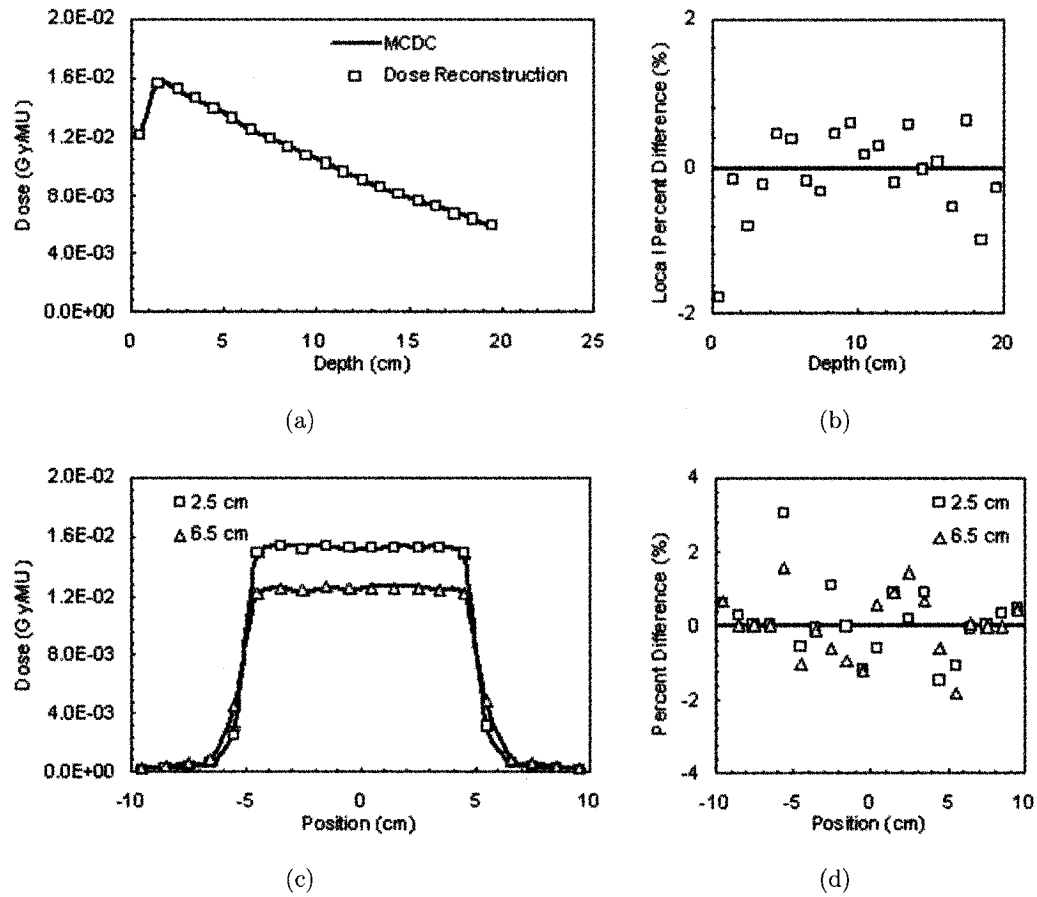

Figure 6–8: Comparison of (a) central depth dose curve and (c) central profiles at 2.5 cm and 6.5 cm depth obtained with the MCDC code (full lines) and the dose reconstruction method (symbols) in a $(20 \times 20 \times 20)$ cm^3, $((1 \times 1 \times 1)$ cm^3 voxels) water phantom, for a 6 MV, (10×10) cm^2 field.

image (in this case simulated) can be backprojected accurately and that the dose reconstruction transports adequately particles in heterogeneous phantoms.

Figure 6–10 shows the original and reconstructed portal images as well as a ratio comparison for the mathematical phantom of figure 6–9. 97% of the pixels within the field have a ratio between 0.95 and 1.05 which means that the two portal images agree within 5% for most pixels. The poor agreement outside of the field is due to the increased uncertainty typical for the low dose regions. The good agreement between the two portal images is an indication of the validity of the dose reconstruction. This agreement was expected since the MC and reconstructed doses were shown to agree in fig 6–9.

Figure 6–11 shows the sensitivity of the dose reconstruction algorithm on the initial primary photon spectrum. The absolute central axis depth dose and lateral profiles at 2.5, 5 and 10 cm depth for the heterogeneous phantom if only one primary photon spectrum is used for the whole detector are found in figure 6–11. Previously (figure 6–9), the portal imager had been divided in 60 rectangular sub-sections of (4×5) cm^2 and a primary photon spectrum was calculated for each sub-sections. In the case where a single spectrum is used the dose reconstruction underestimates the dose by up to 7% in the water region and overestimates the dose slightly in the lung region. In the case where the number of regions is reduced to 15 rectangular sub-sections of (8×10) cm^2 the dose difference observed when compared to the 60 region division was less than 4%. Hence the number of sub-sections does not need to be specified in a very precise manner. However it is still important to have an accurate spectrum or set of spectra to ensure the best dose reconstruction possible.

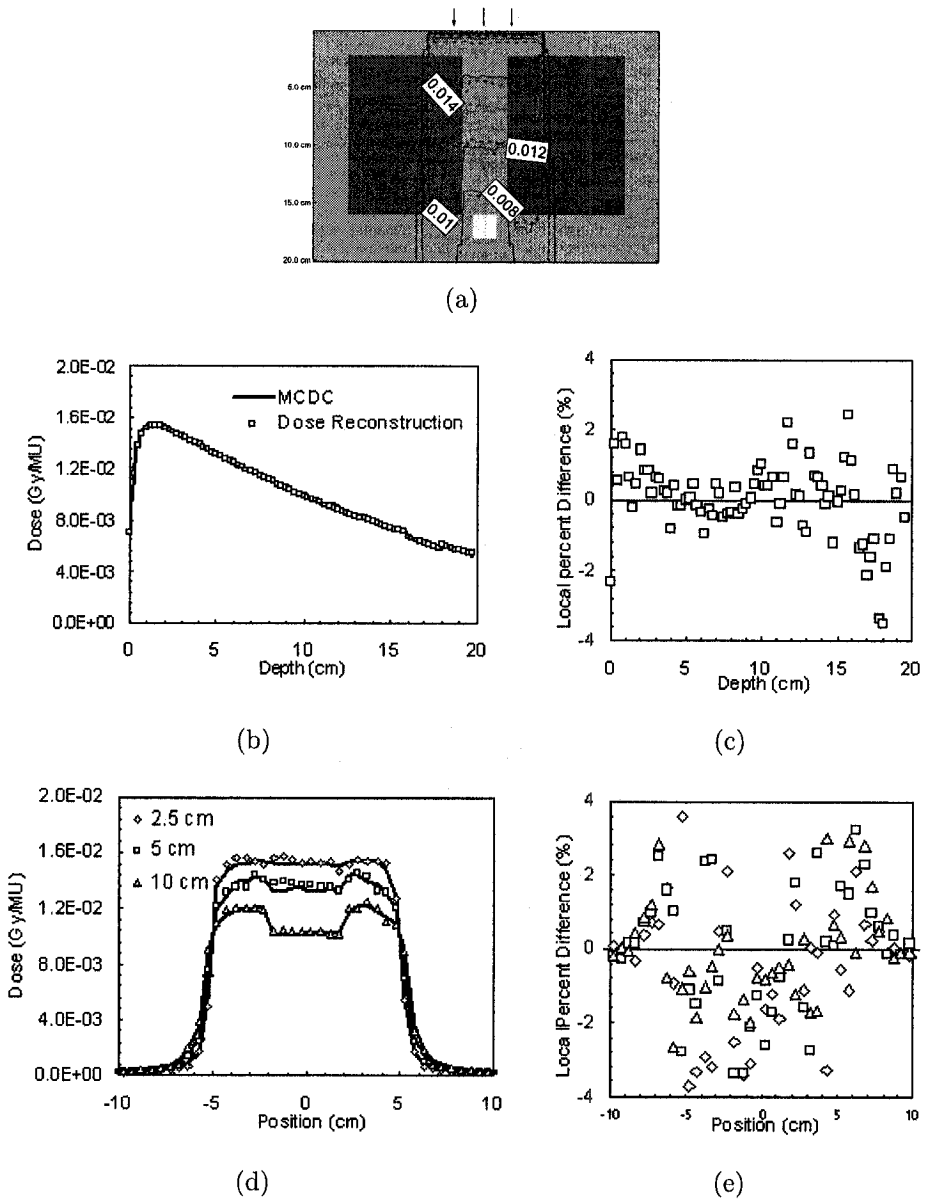

Figure 6–9: Comparison of absolute isodoses in Gy/MU in (a) the axial plane for a mathematical phantom obtained with the dose reconstruction algorithm (dashed lines) and with the MCDC code (full lines) for a 6 MV, (10 × 10) cm^2 field. Comparison of (b) central axis depth dose and (d) lateral profiles at 2.5 cm, 5 cm and 10 cm depth obtained for the same set-up (c) and (e) give the respective local percent difference. The phantom is (30 × 20 × 20) cm^3 with (0.5 × 0.5 × 0.25) cm^3 voxels. The phantom is composed of two lung regions (dark gray) each of (10 × 20 × 24) cm^3 and a bone region (white) of (2 × 20 × 2) cm^3 surrounded by water(grey).

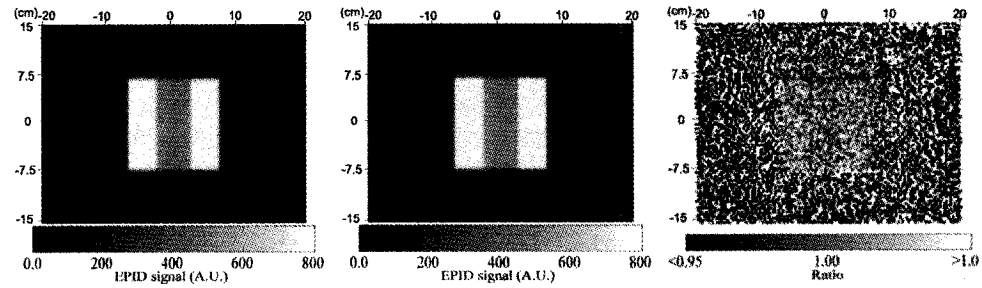

(a) (b) (c)

Figure 6–10: (a) Original and (b) reconstructed portal images for the mathematical water, lung and bone phantom for a 6 MV, (10 × 10) cm^2 field. (c) Ratio of the reconstructed and the original portal image.

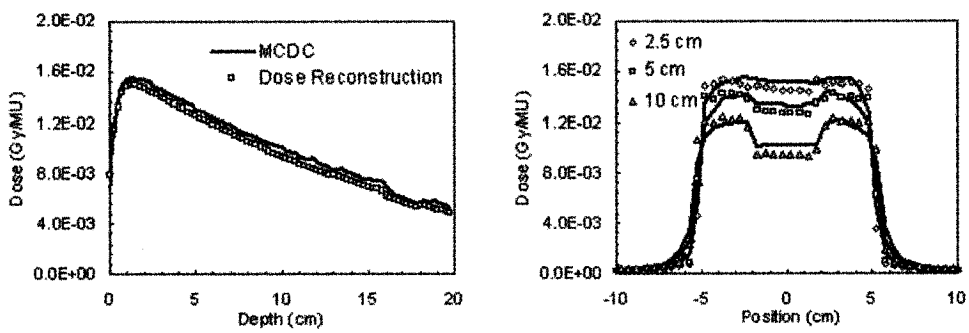

(a) (b)

Figure 6–11: Comparison of (a) absolute central depth dose and (b) absolute lateral dose profiles at 2.5 cm, 5 cm and 10 cm depth obtained algorithm for the heterogeneous phantom when only one spectrum is used over the whole detector. The MCDC calculations are represented by the full lines and the dose reconstruction by various symbols.

6.3.3 Validation of the Dose Reconstruction Using Measurements in a Phantom for IMRT Fields

Figure 6–12 shows the film measurements, the MCDC dose prediction and the dose reconstruction for three IMRT fields. Gamma index maps comparing the dose reconstruction against the film measurements and the MCDC dose prediction are also given in figure 6–12. In the case of the pyramid IMRT field, a gamma index inferior to 1 is obtained for 85% of the pixels within the field when compared to film and 96% of the pixels within the field when compared to MC calculations. The field is defined as the projection of the jaws opening on the portal imager. In the case of the colorectal fields for the two different gantry angles; a gamma index inferior to 1 is obtained for 80% of the pixels within the field when compared to film and 90% of the pixels within the field when compared to MC calculations. The discrepancies between the dose reconstruction and the MCDC may be due to uncertainty in the portal imager position or in the MLC leaf position. The agreement when comparing the dose reconstruction with the MCDC calculations is slightly better than when comparing it with the film measurements. Uncertainty in the positioning of the film can explain a greater discrepancy. The dose reconstruction algorithm can calculate the dose from IMRT fields within acceptable limits.

6.3.4 Comparison of Treatment Planned Dose to Reconstructed Dose in an Anthropomorphic Phantom

Figure 6–13 shows the absolute isodoses computed using the dose reconstruction algorithm and MCDC for the head and the chest of the anthropomorphic phantom in the axial and midsagittal plane. The isodose lines are in close agreement for both the chest and the head region. A gamma map comparison (3 mm, 5%) of the absolute

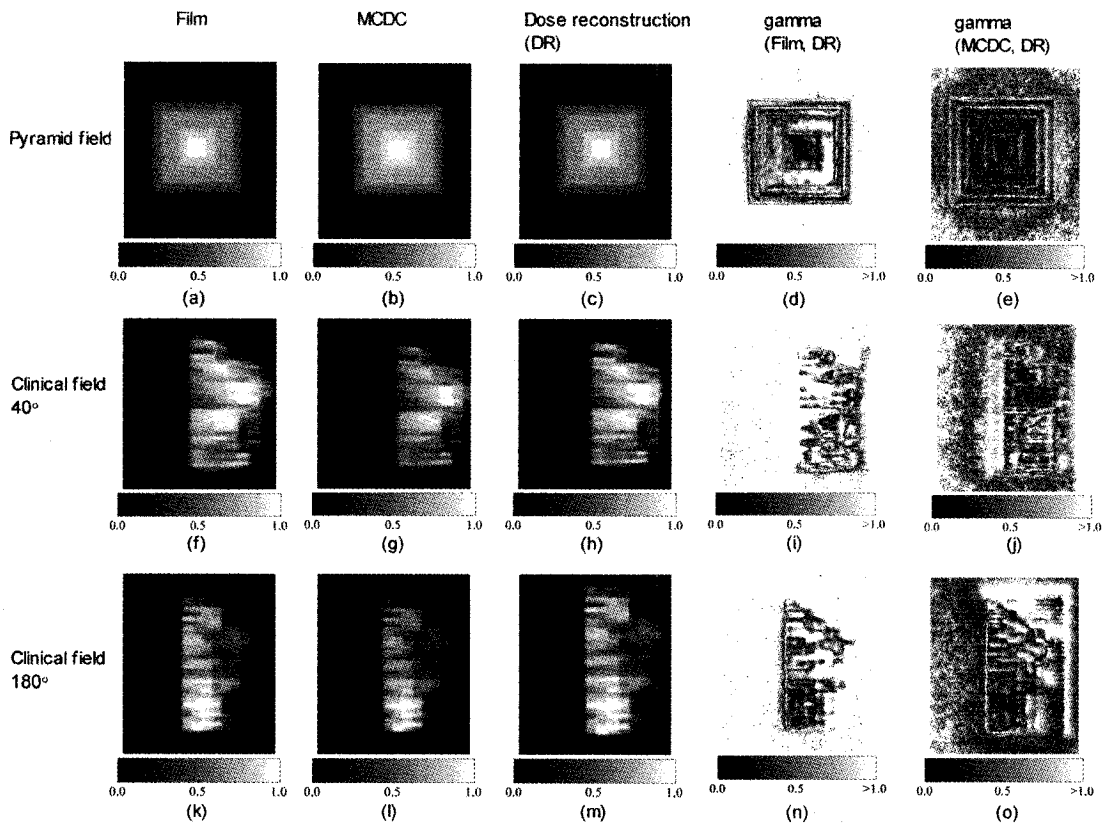

Figure 6–12: (a)(f)(k)Film measurements, (b)(g)(l)MCDC dose prediction, (c)(h)(m) dose reconstruction calculation and (d)(i)(n) comparison between the film and the dose reconstruction and (e)(j)(o) between the MC predictions and the dose reconstruction using the gamma index with 0.3 mm, 5% criteria for (a-e) a pyramid IMRT field and two clinical IMRT fields. For a 17 cm thick solid water phantom, measurements were taken at 6 cm depth.

dose distribution in the axial and midsagittal plane for the head and the chest region gave the following results: for the head 94% and 87% of the pixels had a gamma index inferior to 1 in the axial and midsagittal plane respectively, for the chest 91% and 87% of the pixels had a gamma index inferior to 1 in the axial and midsagittal plane respectively. Uncertainty in the phantom alignment and in the portal imager positioning can explain why some discrepancies are observed between the MCDC and the dose reconstruction. The agreement in the chest region is an example of how the dose reconstruction algorithm is able to predict dose accurately in regions with inhomogeneities.

6.3.5 Quantifying the Difference in EPID Signal for Organ and Patient Motion

Figure 6–14a shows absolute isodoses when the water, lung and bone phantom is shifted by 1 cm between the treatment plan and the treatment delivery while figure 6–15a shows absolute isodose lines when the size of the lungs is reduced by 1 cm on each side in the lateral direction between the treatment plan and the treatment delivery. In these figures, the actual dose delivered (i.e., taking the shift and the shrinkage into account) to the phantom calculated with the MCDC code is compared to the dose reconstruction. Obviously, the dose reconstruction using the original CT does not accurately predict the dose delivered to the patient because of the phantom movement. Figure 6–14b and figure 6–15b show the ratio of the reconstructed images over the original images. In figure 6–14b a dark streak (ratio inferior to 0.95) and a bright streak (ratio superior to 1.05) are showing at the water and lung junctions where the effect of the shift can be seen. Similarly on figure 6–15b two light lines (ratio superior to 1.05) can be seen showing the effect of reducing the lung size.

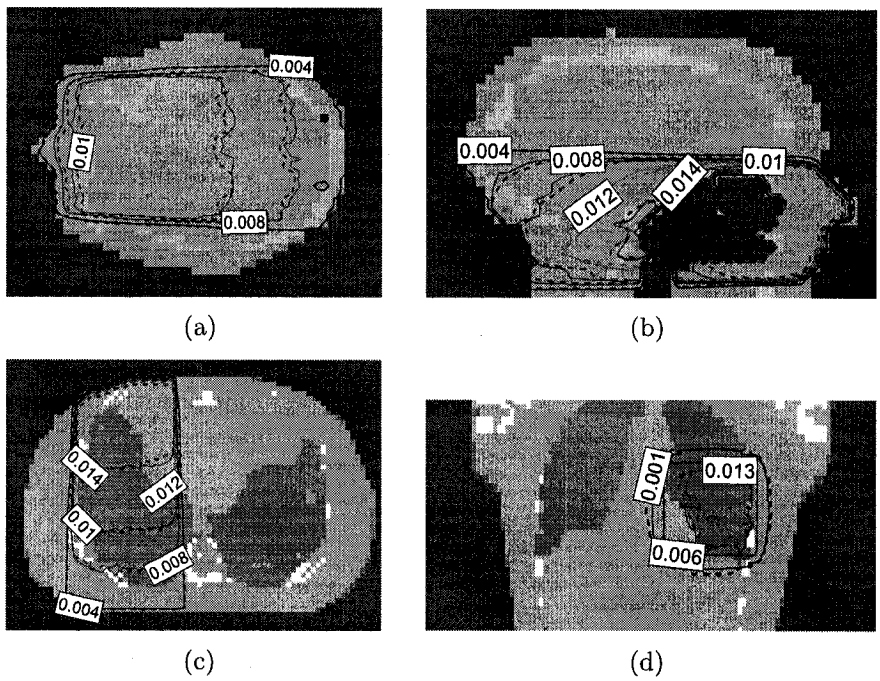

Figure 6–13: Comparison of absolute isodoses in Gy/MU in (a)(c) the axial plane and (b)(d) the sagittal plane for (a)(b) the head and the (c)(d) the chest of an anthropomorphic phantom obtained with the dose reconstruction algorithm (dashed line) and with the MCDC code (full line) for a 6 MV, (10×10) cm^2 anterior/posterior field.

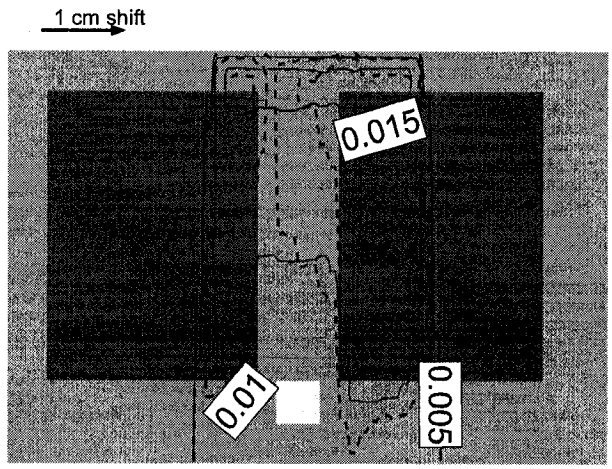

(a)

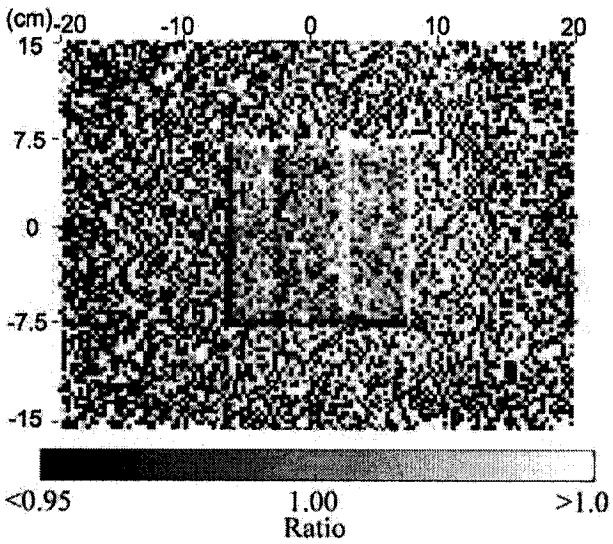

(b)

Figure 6–14: (a) Comparison of MCDC calculated (full lines) and reconstructed (dashed lines) absolute isodoses in Gy/MU when 1 cm shift is introduced in the water, lung and bone mathematical phantom. (b) Ratio of the reconstructed image over the original image for the mathematical water, lung and bone phantom for a 6 MV, (10 × 10) cm^2 field.

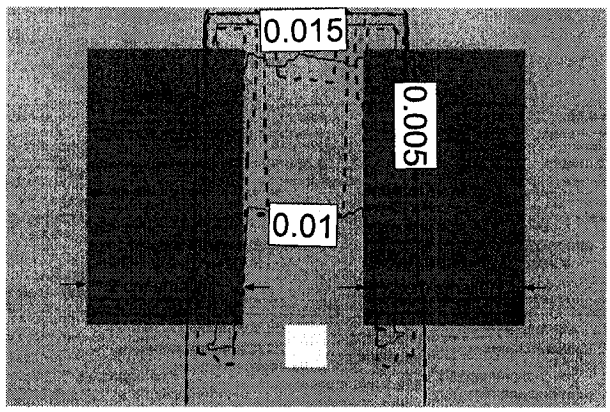

(a)

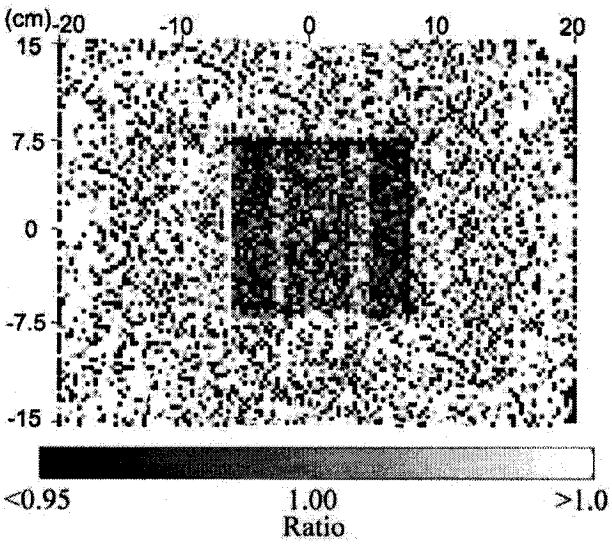

(b)

Figure 6–15: (a) Comparison of MCDC calculated (full lines) and reconstructed (dashed lines) absolute isodoses in Gy/MU when the lung part of the water, lung and bone mathematical phantom is reduced by 1 cm. (b) Ratio of the reconstructed image over the original image for the mathematical water, lung and bone phantom for a 6 MV, (10×10) cm^2 field.

Although the dose reconstruction was performed with the original spectrum from primary photons and the original scattered particle distribution, the main reason for failure of the dose algorithm in the case of patient movement is the use of the original CT data. Comparison of the scattered particle distribution generated before and after the phantom motion showed no statistically significant differences. More important changes in the phantom geometry were found to induce small changes in the scattered particle distribution. For example replacing the lung and bone by water in the mathematical heterogeneous phantom increased the amplitude of scatter by up to 10%. Reducing the thickness of the water and lung portion by half reduced the scatter amplitude by less than 20%. As shown in figure 6–2, the spectrum is somewhat more dependent on the phantom used. However, the impact of the spectrum on the reconstructed dose is indirect, because the photon weighting step corrects the spectrum to some extent, giving a smaller weigth to less probable energies. For example using the lung spectrum (figure 6–2) to reconstruct the dose in the water phantom would produce dose difference of the order of 15%. This is an extreme case that would happen only for some of the voxels in the patient. Moreover, the spectrum is averaged over regions of the patient which include different types of materials. This reduces the impact of motion on the spectrum and hence on the dose reconstruction.

6.4 Discussion

The drive for dose escalation and hypofractionation protocols has rendered dose delivery verification essential. The introduction of MC treatment planning systems which take into account patient inhomogeneities requires dose verification tools which

can also deal with these inhomogeneities. Most dose reconstruction methods presented up to now do not deal with inhomogeneities and were tested on homogeneous phantoms [26, 29]. The dose reconstruction algorithm presented in this paper is based on MC calculations. MC simulations are used to obtain the primary fluence at the portal imager which must be accurate to obtain an accurate reconstructed phase space file and reconstructed dose to the patient. MC simulations are also used to compute the dose to the patient hence inhomogeneities are included in the dose computation.

One drawback of MC simulations is that they are computationally intensive and cannot rapidly produce a dose distribution. However, we believe that the dose reconstruction algorithm presented here can be used clinically if the dose calculation is done overnight. The MCDC step is done only once per patient at the treatment planning stage; it runs 4 hours on a 2.8 GHz AMD processor for the case of the chest of the anthropomorphic phantom presented in section 6.2.3 (voxel size $(0.4 \times 0.4 \times 0.6)$ cm^3) if the linac phase space file is already available. No variance reduction techniques were used but only Compton scattering was taken into account and electron transport was not performed. In the case of IMRT fields the linac phase space generation requires more time because of the leaf movements, the simulation time is dependent on the complexity of the field used. For the IMRT fields used in this study, the linac phase space simulation time was about twice the simulation time required for open fields. This computation time can be reduced by using an analytical program to simulate the leaf movements instead of a full MC simulation [47] or by ignoring the electron transport in the MLC. The phase space reconstruction and

the dose reconstruction require a total of 60 hours on an AMD 2.8 GHz processor for the chest of the anthropomorphic phantom. The computation time can be reduced if it is run on a cluster of computers which are now widely available. In the case of IMRT fields the reconstruction step does not require more simulation time. The dose reconstruction can easily be calculated overnight and if necessary changes to the treatment plan can be made before the next fraction.

Advanced technology such as IMRT delivery allows highly conformal dose distributions and has the potential to improve the treatment outcome. However, day-to-day dose verification becomes even more important not only because small patient movement can now have a significant impact on the dose distribution but also because mechanical failures are more likely to occur. Hence even though pre-treatment verification is necessary it may not be sufficient to ensure accurate dose delivery. The technique presented here uses portal images acquired during the treatment delivery. Compared to other techniques which acquire images without the patient in the beam [28], it can detect treatment delivery errors that occurred during the dose delivery and this at every treatment fraction. Moreover no additional dose is given to the patient since the portal image is acquired with the treatment beam.

One of the main limitations of dose reconstruction techniques based on a planning CT is that the reconstruction becomes unreliable when patient motion occurs. This is a problem that all dose reconstruction methods face [26, 29]. Although this limitation exists for the method presented here, the reconstructed portal image allows for a detection of movement and hence the user is aware that the dose reconstruction may not be as reliable. The purpose of this paper was not to quantify the amount of

movement; however, this is something that could be investigated further. Other reconstruction methods do not have this extra feature [22, 25, 26, 29]. This limitation can be avoided if a CT scan is acquired on the treatment day and in the treatment position [22, 25]. This can be achieved using cone beam computed tomography (CBCT) or a CT on rails. In that case the dose algorithm presented here can be adapted to use the daily CT scan instead of the planning CT. CT images acquired right before the treatment can be used to provide patient information that is more representative of the patient anatomy and the treatment geometry. The scattered particle distribution at the EPID, the spectrum of the primary particles and the voxelized representation of the patient can all be derived from these CT images without increasing the dose reconstruction time significantly (around 7 %). For facilities that are not equipped with CBCT or CT on rails, the dose algorithm presented in this paper can at least give an indication that significant motion has occurred.

The algorithm was shown to work for 6 MV beams and could be adapted to work for 10 MV beams. Although the method could also be adapted for higher energy beams (e.g. 18 MV) it would require a significant amount of modifications. The active layer of the detector is not in electronic equilibrium for higher energy beams and hence an additional layer of buildup material needs to be placed on top of the portal imager and its response needs to be studied in more detail. Moreover, the algorithm was written under the assumption that most interactions are Compton scattering events and this may not be the case for increased beam energies.

At first glance the many steps of the dose reconstruction algorithm may not seem very user friendly. However, all these steps can easily be integrated in any

MC treatment planning system. It will, in fact, be built in the McGill Monte Carlo Treatment Planning (MMCTP) system [48] in the near future.

6.5 Conclusion

In this study we developed a new dose verification tool based on portal imaging and MC simulations. This verification tool can accurately predict the dose distribution for complex IMRT fields and in the presence of patient inhomogeneities. The dose verification algorithm was tested for various phantoms and radiation fields. Agreement within 4% was obtained for static fields and within 3 mm or 5% for IMRT fields when compared to Monte Carlo calculations and to measurements. A test was also included in the algorithm which can detect patient or organ movement.

6.6 Clinical Application of the Dose Reconstruction Method for a Lung Tumor in an Anthropomorphic Phantom

This section was added to complement the manuscript submitted to *Physics in Medicine and Biology.* In the manuscript, the dose reconstruction method was verified using static fields on an anthropomorphic phantom and IMRT fields on a water phantom; however, the dose reconstruction was not tested for a complete IMRT treatment delivered to an anthropomorphic phantom. In this section, we present how the dose reconstruction method performs in the case of a lung IMRT treatment for the chest of an anthropomorphic phantom.

Planning CT images of the anthropomorphic phantom were acquired. The contour of an imaginary lung tumor was defined and the organs at risk were contoured. The IMRT treatment was planned with Corvus®(NOMOS Radiation Oncology, PA), an inverse treatment planning system. The IMRT plan consists of four 6 MV beams modulated using MLCs and irradiating from four different gantry angles.

This plan was delivered using the Varian CL21EX linac, the phantom was positioned carefully using markers placed during the planning CT acquisition. A portal image was acquired using the aS500 EPID for each field delivered. The SDD was set to 150 cm. The treatment plan was recalculated using MC simulations. For this purpose, the planning CT images were transformed to a voxelized phantom of $(0.5 \times 0.5 \times 0.8)$ cm^3 voxels; the same phantom was later used with the dose reconstruction algorithm. The dose to the phantom and the spectrum from primary photons were derived from the simulations. The simulations were also used to obtain the portal image produced by the scattered photons, which is needed by the reconstruction algorithm. The dose reconstruction algorithm was then used to reconstruct the absolute dose to the anthropomorphic phantom for each of the four fields. A reconstructed portal image was obtained for each of the four fields.

Figure 6–16 shows the absolute isodoses, in units of Gy, computed using the dose reconstruction algorithm and the MC dose recalculation in the axial and sagittal planes. The reconstructed isodoses are in close agreement to the MC recalculated one. A gamma map comparison (15 mm, 5%) yields a gamma index smaller than 1 for 92% and 95% of the pixels in the sagittal and the axial plane respectively. If the distance criteria is reduced to 5 mm, the gamma index is now smaller than 1 for 88% and 92% of the pixels in the sagittal plane and in the axial plane. However, it should be kept in mind that Low and Dempsey [43] recommend that the distance criterion be 3 times the pixel size.

Figure 6–17 shows the comparison of the original and reconstructed portal images for the IMRT fields at 0° and 250° gantry angle. All four IMRT fields were

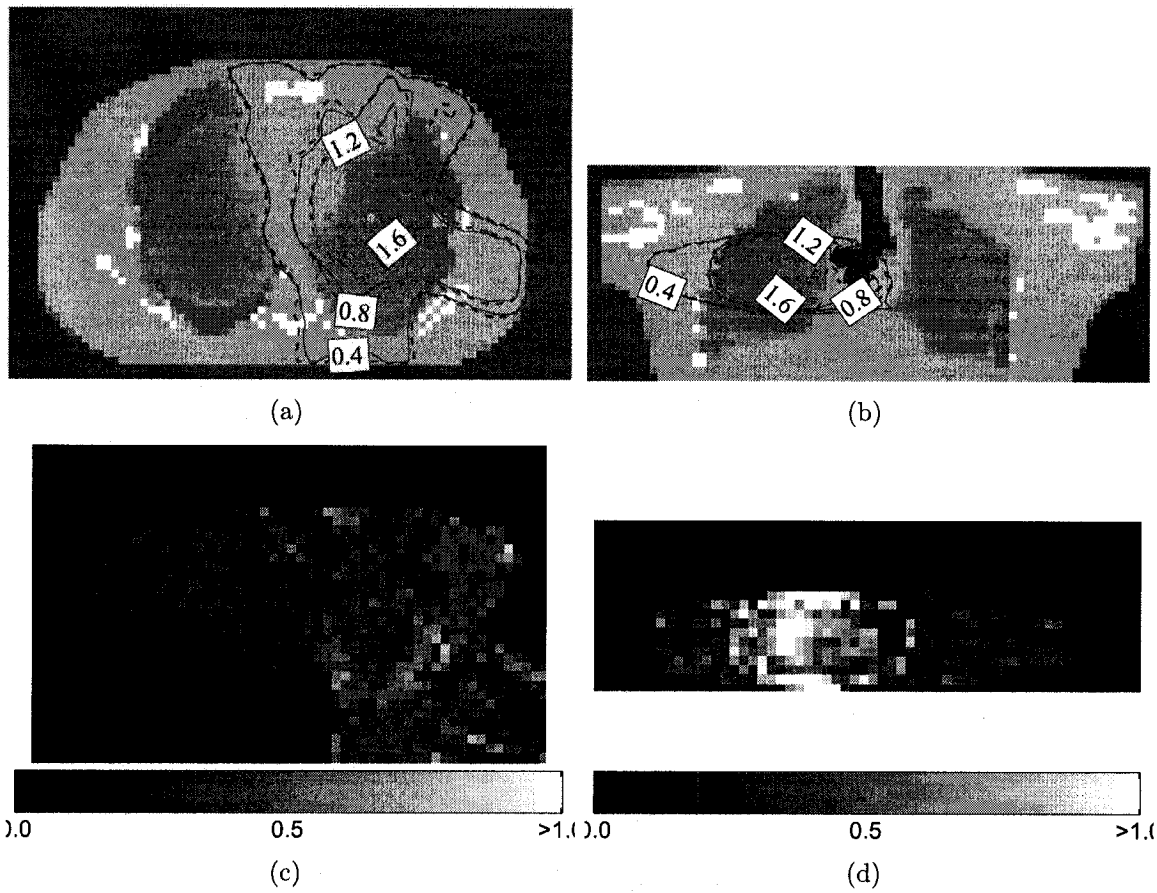

(a) (b)

(c) (d)

Figure 6–16: Comparison of absolute isodoses in Gy in (a) the axial plane and (b) the sagittal plane for the chest of an anthropomorphic phantom obtained with the dose reconstruction algorithm (dashed line) and with the MCDC code (full line) for a 6 MV, IMRT treatment. (c) and (d) are the gamma maps with 5% and 15 mm criterion for the axial and sagittal plane respectively.

analyzed; they all yield similar agreement. The original and reconstructed portal images agree within 5% for 96% of the pixels that are within the radiation field for both gantry angles. This good agreement indicates that no motion occurred between the CT scan and the treatment delivery.

The test described above is very similar to a clinical situation. It includes a complex treatment plan, involving many fields with dynamic IMRT delivery. The phantom is close to human anatomy, the region studied includes inhomogeneities such as the lungs, the ribs and the spine. However, this is still a simplified scenario: (1) with a rigid phantom motion can be reduced to a minimum between the planning CT and the treatment delivery and (2) there is no breathing motion or cardiac motion during the treatment delivery. Further investigation is required to determine the effect of respiratory motion on the dose reconstruction, this could be achieved using a breathing phantom or patients.

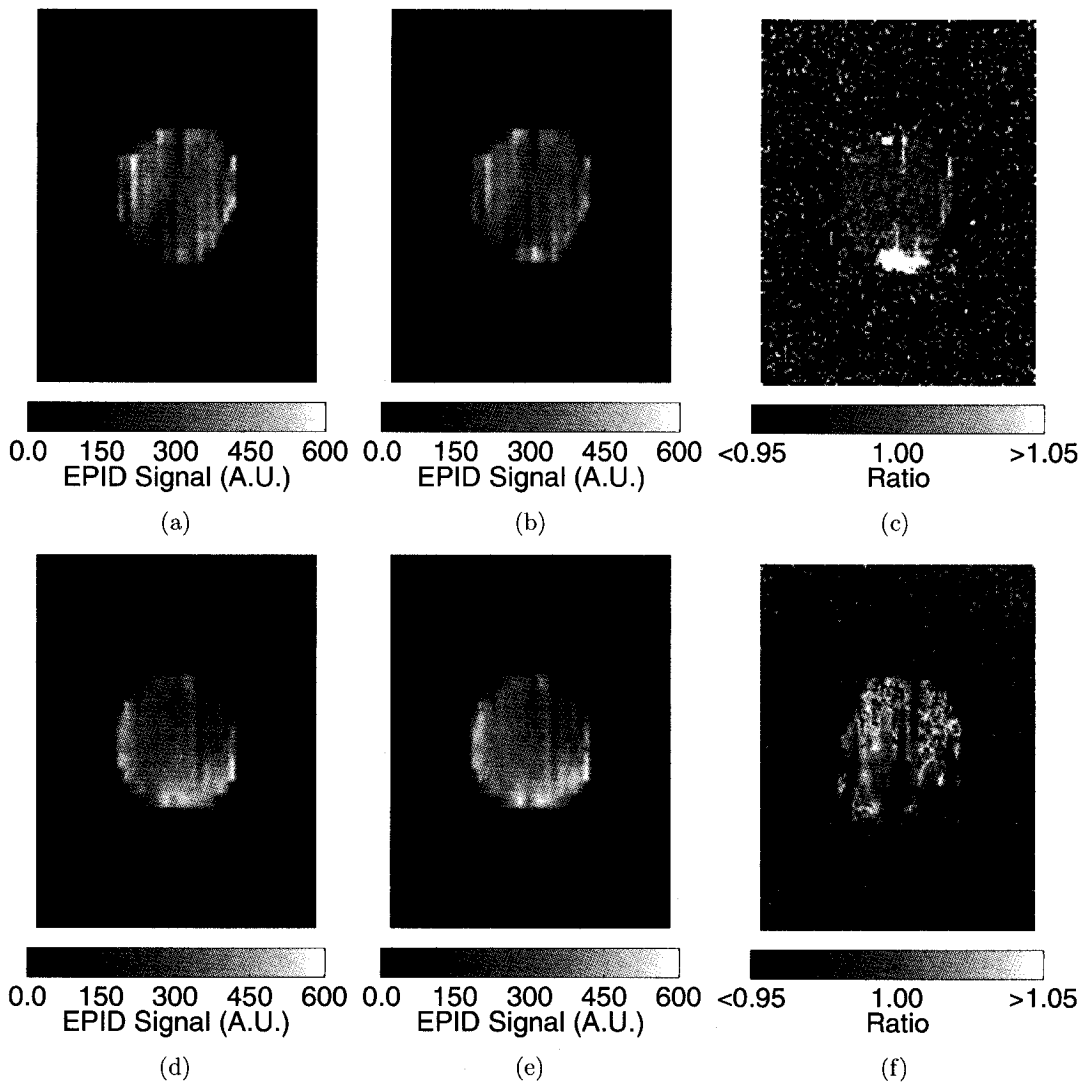

Figure 6–17: (a)(d) Original and (b)(e) reconstructed portal images for the chest of the anthropomorphic phantom for a 6 MV, IMRT field at (a)(b)(c) 0° and 250° gantry angle. (c)(f) Ratio of the reconstructed and the original portal image.

In this chapter, we have shown that it is possible to reconstruct the dose delivered during conventional and IMRT treatments using portal images and MC simulations. This is an essential step of treatment verification. However, as it was discussed in section 6.4 adequate patient positioning is essential to do accurate dose reconstruction. This can be achieved in part through thorough patient alignment using portal images. However, due to the poor image quality of portal images, only bony anatomy can be aligned. Hence the need for new technologies, such as kV CBCT, which allow soft tissue alignment. In the next chapter, we will discuss how the image quality of kV CBCT images can be improved by removing the scattered particles contribution. Such improvements can also lead to the use of kV CBCT images acquired the day of the treatment to perform the dose reconstruction.

References

[1] Webb S. *The physics of three dimensional radiation therapy conformal radiotherapy, radiosurgery and treatment planning.* Institute of Physics Publishing, Bristol, UK, 1993.

[2] Bentzen S M. Theragnostic imaging for radiation oncology: dose painting by numbers. *Lancet Oncol.*, 6:112–117, 2005.

[3] Andreo P. Monte Carlo techniques in medical radiation physics. *Phys. Med. Biol.*, 36:861–920, 1991.

[4] Rogers D W O, Faddegon B A, Ding G X, Ma C M, Wei J, and Mackie T R. BEAM: A Monte Carlo code to simulate radiotherapy treatment units. *Med. Phys.*, 22:503–524, 1995.

[5] Verhaegen F and Seuntjens J. Monte Carlo modeling of external radiotherapy photon beam. *Phys. Med. Biol.*, 48:R107–R164, 2003.

[6] Dutreix A. When and how can we improve precision in radiotherapy. *Radiother. Oncol.*, 2:271–292, 1984.

[7] Brahme A. Dosimetric precision requirements in radiation therapy. *Acta Radiol. Oncol.*, 23:379–91, 1984.

[8] Brahme A. Optimized radiation therapy based in radiobiological objectives. *Semin. Radiat. Oncol.*, 9:35–47, 1999.

[9] van Esch A, Bohsung J, Sorvari P, Tenhunenc M, Paiuscod M, Iorid M, Engstrome P, Nystrome H, and Huyskens D P. Acceptance tests and quality control procedures for the clinical implementation of intensity modulated radiotherapy (IMRT) using inverse planning and sliding windows technique: experience from five radiotherapy departments. *Radiother. Oncol.*, 65:53–70, 2004.

[10] Antonuk L E. Electronic portal imaging devices: a review and historical perspective of contemporary technologies and research. *Phys. Med. Biol.*, 47:R31–R65, 2002.

[11] Chang J, Mageras G S, Chui C S, Ling C C, and Lutz W. Relative profile and dose verification of intensity-modulated radiation therapy. *Int. J. Radiat. Oncol. Biol. Phys.*, 47:231–240, 2000.

[12] van Esch A, Vanstraelen B, Verstraete J, Kutcher g, and Huyskens D. Pre-treatment dosimetric verification by means of a liquid-filled electronic portal imaging device duting dynamic delivery of intensity modulated treatment fields. *Radiother. Oncol.*, 60:181–190, 2001.

[13] Partridge M, Symonds-Tayler R N, and Evans P M. IMRT verification with camera-based electronic portal imaging system. *Phys. Med. Biol.*, 45:N183–N196, 2000.

[14] El-Mohri Y, Antonuk L E, Yorkston J, Jee K W, Maolinbay M, Lam K L, and Siewerdsen J H. Relative dosimetry using active matrix flat-panel imager (AMFPI) technology. *Med. Phys.*, 26:1530–1541, 1999.

[15] McCurdy B M C, Luchka K, and Pistorius S. Dosimetric investigation and portal dose image prediction using an amorphous silicon electronic portal imaging device. *Med. Phys.*, 28:911–924, 2001.

[16] van Esch A, Depuydt T, and Huyskens D P. The use of an aSi-based EPID for routine absolute dosimetric pre-treatment verification of dynamic IMRT fields. *Radiother. Oncol.*, 71:223–234, 2004.

[17] Greer P B and Popescu C C. Dosimetric properties of an amorphous silicon electronic portal imaging device for verification of dynamic intensity modulated radiation therapy. *Med. Phys.*, 30:1618–1627, 2003.

[18] Grein E E, Lee R, and Luchka K. An investigation of a new amorphous silicon electronic portal imaging device for transit dosimetry. *Med. Phys.*, 29:2262–2268, 2002.

[19] Siebers J V, Kim J O, Ko L, Keall P J, and Mohan R. Monte Carlo computation of dosimetric amorphous silicon electronic portal images. *Med. Phys.*, 31:2135–2146, 2004.

[20] Spezi E and Lewis D G. Full forward Monte Carlo calculation of portal dose from MLC collimated treatment beams. *Phys. Med. Biol.*, 47:377–390, 2002.

[21] van Elmpt W J, Nijsten S M J J G, Mijnheer B J, and Minken A W H. Experimental verification of a portal dose prediction model. *Med. Phys.*, 32:2805–2818, 2005.

[22] McNutt T R, Mackie T R, Reckwerdt P, and Paliwal B R. Modeling dose distributions from portal dose images using the convolution/superposition method. *Med. Phys.*, 23:1381–1392, 1996.

[23] Hansen V N, Evans P M, and Swindell W. The application of transit dosimetry to precision radiotherapy. *Med. Phys.*, 23:713–721, 1996.

[24] Boellaard R, Essers M, van Herk M, and Mijnheer B J. New method to obtain the midplane dose using portal in vivo dosimetry. *Int. J. Radiat. Oncol. Biol. Phys.*, 41:465–474, 1998.

[25] Partridge M, Ebert M, and Hesse B-M. IMRT verification by three-dimensional dose reconstruction from portal beam measurements. *Med. Phys.*, 29:1847–1858, 2001.

[26] Wendling M, Louwe R J W, McDermott L N, Sonke J-J, van Herk M, and Mijnheer J. Accurate two-dimensional IMRT verification using a back-projection EPID dosimetry method. *Med. Phys.*, 33:259–273, 2006.

[27] Steciw S, Warkentin B, Rathee S, and Fallone B G. Three-dimensional IMRT verification with a flat-panel EPID. *Med. Phys.*, 32:600–612, 2005.

[28] van Elmpt W J, Nijsten S M J J G, Schiffeleers R F H, Dekker A L A J, Mijnheer B J, Lambin P, and Minken A W H. A Monte Carlo based three-dimensional dose reconstruction method derived from portal dose images. *Med. Phys.*, 33:2426–2434, 2006.

[29] Louwe R J W, Damen E M F, van Herk M, Minken A W H, Torzsok O, and Mijnheer B J. Three-dimensional dose reconstruction of breast cancer treatment using portal imaging. *Med. Phys.*, 30:2376–2389, 2003.

[30] Jarry G and Verhaegen F. Electron beam treatment verification using measured and Monte Carlo predicted portal images. *Phys. Med. Biol.*, 50:4977–4994, 2005.

[31] Li W, Siebers J, and Kawrakow I. Fast Monte Carlo computation of aSi-EPID dose images for IMRT treatment field through phantom. *Med. Phys.*, 33:2168, 2006.

[32] Bissonnette J-P, Munro P, and Cunningham I A. Monte Carlo simulation of the image formation process in portal imaging. *Med. Phys.*, 30:3243–3250, 2003.

[33] Heath E and Seuntjens J. Development and validation of a BEAMnrc component module for accurate Monte Carlo modeling of the Varian dynamic Millenium multileaf collimator. *Phys. Med. Biol.*, 48:4045–4063, 2003.

[34] Walters B, Kawrakow I, and Rogers D W O. DOSXYZnrc users manual. PIRS 794revB, NRCC, 2004.

[35] Jarry G, Graham S A, Moseley D J, Jaffray D A, Siewerdsen J H, and Verhaegen F. Characterization of scattered radiation in kV CBCT images using Monte Carlo simulations. *Med. Phys.*, 33:4320–4329, 2006.

[36] Munro P and Bouius D C. X-ray quantum limited portal imaging using amorphous silicon flat-panel arrays. *Med. Phys.*, 25:689–702, 1998.

[37] Antonuk L E, El-Mohri Y, Huang W, Jee K W, Siewerdsen J H, Maolinbay V E, Scarpine V E, Sandler H, and Yorkstone J. Initial performance evaluation of an indirect-detection, active matrix flat panel imager (AMFPI) prototype for megavoltage imaging. *Int. J. Radiat. Oncol. Biol. Phys.*, 42:437–454, 1998.

[38] Chaney E L, Culip T J, and Gabriel T A. A Monte Carlo study of accelerator head scatter. *Med. Phys.*, 21:1383–1390, 1994.

[39] Kahn H. Application of Monte Carlo. AECU 3259, Rand Corporation, 1954.

[40] Attix F H. *Introduction to radiological physics and radiation dosimetry.* Wiley, New York, 1986.

[41] Low D A, Harms W B, Mutic, and Purdy J A. A technique for the quantitative evaluation of dose distribution. *Med. Phys.*, 25:656–661, 1998.

[42] Van Dyk J, Barnett R B, Cygler J E, and Shragge P C. Commissioning and quality assurance of treatment planning computers. *Int. J. Radiat. Oncol. Biol. Phys.*, 26:261–273, 1993.

[43] Low D A and Dempsey J F. Evaluation of the gamma dose distribution comparison method. *Med. Phys.*, 30:2455–2464, 2003.

[44] Swindell W and Evans P M. Scattered radiation in portal images: a Monte Carlo simulation and a simple physical model. *Med. Phys.*, 23:63–73, 1996.

[45] Zhu X R, Jursinic P A, Grimm D F, Lopez F, Rownd J J, and Gillin M T. Evaluation of Kodak EDR2 film for dose verification of intensity modulated radiation therapy by a static multileaf collimator. *Med. Phys.*, 29:1687–1692, 2002.

[46] Winkler P, Zurl B, Guss H, Kindl P, and Stuecklschweiger G. Performance analysis of a film dosimetric quality assurance procedure for IMRT with regard to the employment of quantitative evaluation methods. *Phys. Med. Biol.*, 50:643–654, 2005.

[47] Siebers J V, Keall P J, Kim J O, and Mohan R. A method for photon beam Monte Carlo multileaf collimator particle transport. *Phys. Med. Biol.*, 47:3225–3249, 2002.

[48] Alexander A, DeBlois F, and Seuntjens J. MMCTP a radiotherapy research environment for Monte Carlo and patient-specific treatment planning. *Med. Phys.*, 33:2293, 2006.

CHAPTER 7
KV CBCT Scatter Correction using MC Simulations

The standard technique for verification imaging prior and during treatment uses megavoltage (MV) imaging which produces images of poor quality in which only bony anatomy is clearly distinguishable. In order to improve patient positioning verification, it is essential to obtain images of better quality. One way of doing this is to use kilovoltage (kV) cone beam computed tomography (CBCT). This technology allows the acquisition of 3-dimensional images of patients, these images can be used to position the patient but also to do dose verification by using the CBCT scan instead of the planning CT scan. However, kV CBCT suffers from image degradation due to the important contribution of scattered particles. The scattered radiation reduces the contrast and produces artifacts but more importantly it introduces errors in the reconstruction pixel values which are no longer reliable for dose calculations. In this chapter, we present two papers which describe a technique based on Monte Carlo (MC) simulations to characterize the scattered radiation and to correct for scatter in the reconstructed images.

The first paper is pending publication in *Medical Physics*. It describes how MC simulations can be used to predict scatter and discusses how scatter varies under different conditions. It also briefly describes the scatter correction technique.

Title: Characterization of scattered radiation in kV CBCT images using Monte Carlo simulations

Authors: G Jarry, S A Graham, D J Moseley, D A Jaffray, J H Siewerdsen and F Verhaegen

Published in Medical Physics, vol.33 p.4320-4329 (2006),

Abstract

Kilovoltage (kV) cone beam computed tomography (CBCT) images suffer from a substantial scatter contribution. In this study, Monte Carlo (MC) simulations are used to evaluate the scattered radiation present in projection images. These predicted scatter distributions are also used as a scatter correction technique. Images were acquired using a kV CBCT bench top system. The EGSnrc MC code was used to model the flat panel imager, the phantoms and the x-ray source. The x-ray source model was validated using first and second half value layers (HVL) and profile measurements. The HVLs and the profile were found to agree within 3% and 6%, respectively. MC simulated and measured projection images for a cylindrical water phantom and for an anthropomorphic head phantom agreed within 8% and 10%. A modified version of the DOSXYZnrc MC code was used to score phase space files with identified scattered and primary particles behind the phantoms. The cone-angle, the source-to-detector distance, the phantom geometry and the energy were varied to determine their effect on the scattered radiation distribution. A scatter correction technique was developed in which the MC predicted scatter distribution is subtracted from the projections prior to reconstruction. Preliminary testing of the procedure was done with an anthropomorphic head phantom and a contrast phantom. Contrast

and profile measurements were obtained for the scatter corrected and non-corrected images. An improvement of 3% for contrast between solid water and a liver insert and 11% between solid water and a Teflon insert were obtained and a significant reduction in cupping and streaking artifacts was observed.

7.1 Introduction

In recent years, kilovoltage (kV) cone beam computed tomography (CBCT) has shown potential for image-guided radiotherapy [1] and three-dimensional breast imaging [2]. However, this technology still has some important limitations. kV CBCT images are subject to a substantial contribution from scattered x-rays originating in the patient and reaching the detector. This effect is more important in CBCT than in fan-beam CT due to the larger cone angle employed and the lack of post-patient collimation in the 2D detectors used to acquire the images. This scatter contribution degrades the image quality by degrading the contrast, by increasing the noise and by introducing shading artifacts [3]. Shading artifacts can be divided into (1) cupping artifacts where attenuation coefficients in the reconstructed image of a uniform water cylinder are non-uniform and reduced forming a "cup" and (2) streaking artifacts where similar effects occur between two dense objects, forming a "streak" [4]. Techniques to reduce the scatter contribution rely on knowing how the scatter varies under different conditions. These techniques include increasing the air gap between the object and the detector and using anti-scatter grids [3, 5]. Other correction techniques based on analytical prediction of scatter [6] and empirical methods [5, 7, 8] such as beam stop array techniques, can be further validated

by understanding better the scattered radiation distribution and its dependence on imaging system parameters.

The magnitude and the effects of x-ray scatter in CBCT kV imaging have been studied using empirical techniques such as beam stop arrays [9] and blocks [3, 10]. Analytical models have also been used to study the scatter contribution in diagnostic radiology [11, 12]. However, these models are limited when complex geometries or heterogeneous media are involved.

Monte Carlo (MC) simulations have previously been used to study the scattered radiation distribution in diagnostic radiology and they have been shown to be the most successful method for the investigation of the production of scattered particles in a medium. MC simulations were used to study how the scatter fraction varies with different imaging parameters [13] and to study the angular, spectral and spatial distribution of the scattered particles [14] for mono-energetic point sources in the diagnostic energy range. Boone and Seibert [12] used MC techniques to evaluate the point spread function of scattered radiation in diagnostic radiology. Recently Malusek *et al* [15] used MC simulations to predict the scattered radiation in CBCT projection images. They used a simplified CT scanner geometry which consisted of a point source emitting mono-energetic photons or a spectrum of photons, different phantoms and a cylindrical detector array. Ay and Zaidi [16] used the MCNP4C [17] MC code to model fan and cone beam systems. They studied the effect of bow-tie filters, phantom sizes and grid septa length on the scatter distribution.

Advances in MC simulations and in computer power now allow for more complete models of the x-ray source, the scattering material and the detector. In this study

we fully model a kV CBCT system using the EGSnrc MC code. This model is validated against bench-top measurements and is used to investigate the scatter distribution under various imaging conditions. Preliminary testing shows that MC scatter predictions can be used to correct for scatter in measured CBCT images.

7.2 Materials and Methods

7.2.1 Measurements

A CBCT bench-top system [18] was used to acquire all measured images. The bench-top system consists of an x-ray tube and a flat panel detector which can be translated in three dimensions and a rotating platform (figure 7–1(a)). The x-ray tube is a Rad-94 (manufacturer Varian) with Sapphire housing. It has a 14° tungsten-rhenium-molybdenum-graphite target. To simplify the modeling of the x-ray tube, the mirror and the cross hair were removed and replaced by an equivalent aluminum thickness for both the measurements and the simulations. The total added filtration consists of 3.711 mm aluminum and 0.122 mm copper. The fan and cone-angle collimation is provided by two sets of tungsten shutters (~2 mm thick). The imaging detector employed is a Paxscan 4030A amorphous silicon (aSi) digital x-ray detector (manufacturer Varian) [19] with an active area of (40 × 30) cm^2 . It consists of a carbon fiber sheet overlying a 0.06 cm scintillating layer of CsI:Tl and a (2048 × 1536) pixels aSi light sensor photodiode array. In this study, both projection image sets and CBCT image sets were collected. Typical projection images were averaged over 100 images to minimize noise. The CBCT acquisitions for the reconstructions consisted of 320 projections taken at 1.125° intervals. All projections were corrected for variations in gain and offset according to equation 7.1. The calibrated images were multiplied

by a factor of 10^4. This factor is arbitrary and does not affect image quality or HU accuracy. It is used to stretch detector pixel values reasonably across the digitization range.

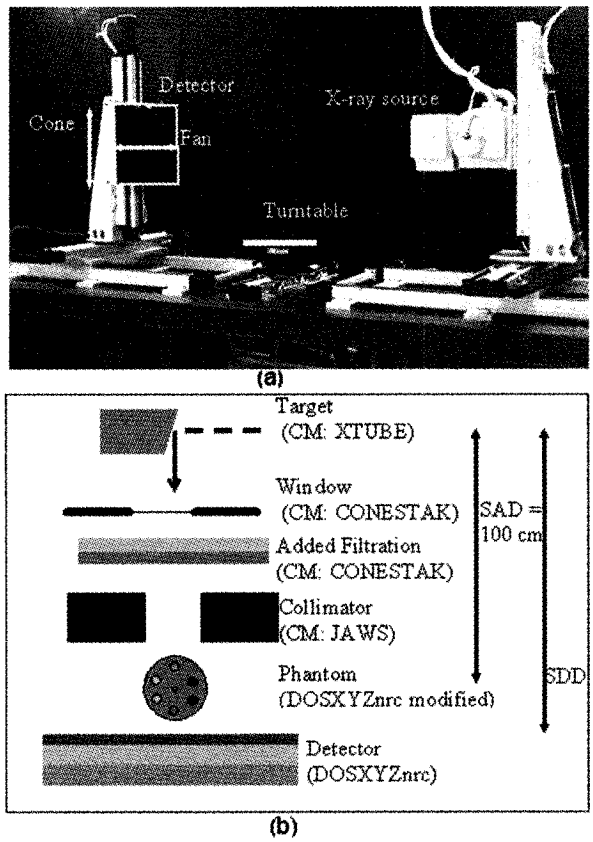

Figure 7–1: (a) Photograph of the kV-CBCT bench with the x-ray source, the turn table and the detector identified and (b) a schematic illustration of the Monte Carlo model for the CBCT bench with the component modules (CM) that were used.

$$\text{Calibrated Image}(i,j) = \frac{\text{Image}(i,j) - \text{Dark Image}(i,j)}{\text{Flood Image}(i,j) - \text{Dark Image}(i,j)} \times 10,000 \qquad (7.1)$$

7.2.2 Simulations

The BEAMnrc MC code system [20] was used to build a model for the Rad-94 x-ray tube according to the manufacturer's specifications. A schematic diagram of the x-ray tube model is shown in figure 7–1. The model includes the target simplified as tungsten only, the exit window, the added filtration and the collimation. Various collimation settings and beam energies of 80, 100 and 120 kVp were modeled. The energy of the primary electrons hitting the target was set to the potential across the tube. The photon transport cut-off energy was set to 10 keV while the electron transport cut-off total energy was set to 531 keV in all component modules. A total of 40×10^9 primary electrons impinged on the target to generate the phase space files [20] which contains information on the particles energy, position (x and y coordinates) and direction of motion. The phase space file is scored at a plane just below the added filtration. Particles sampled from the phase space file were each transported once through the different collimated fields and a second phase space file was obtained after the collimators. The number of particles in the phase space files varied from 18,000 to 25,000 particles/cm^2 for 80 kVp to 120 kVp, respectively.

The phase space file particles were transported through different voxelized geometries using a modified version of the DOSXYZnrc program [21]. This modified version tags the particles when they undergo scatter interactions hence identifying the scattered and primary particles. Phase space files were collected around the phantom, in planes corresponding to the detector position. These phase space files can include all particles, only the scattered particles or only the primary particles.

Electron transport was not simulated given the limited range of the electrons produced at keV energies.

The DOSXYZnrc program was used to develop a model of the PaxScan 4030A imaging panel. Veiling glare effects, believed to be negligible [22], were not included in the MC simulations. The detector response was obtained by scoring the energy absorbed in the CsI layer of the detector since the response of the photodiodes is proportional to the energy deposition in the CsI layer [23]. The CsI layer was modeled as a mixture of Cesium and Iodine with a 4.51 g/cm^3 density. The MC model of the detector was used to obtain the energy absorbed in the CsI layer for various monoenergetic pencil beams. This information was used to create a look-up table containing various energies and the corresponding energy absorbed in phosphor. In order to reduce the simulation time an analytical program was developed to produce detector images. The program uses the information stored in the phase space file to determine the energy deposited in the phosphor layer. The particle energy is used to obtain the energy deposited in the active layer of the imager by using the abovementioned look-up table. The photon direction is used to scale the energy deposited with the particle path length in the phosphor. Each photon deposits its energy in only one pixel, this was found to be a valid assumption given the thickness of the phosphor. The analytical program was used to obtain all simulated images. The size of the detector pixel can be varied to reduce the noise by binning the pixels; in this case the measured images are binned to match the simulated pixel size. The simulated images were calibrated according to equation 7.2; where 10,000 is the same arbitrary factor mentioned in equation 7.1.

$$\text{Simulated Calibrated Image}(i,j) = \frac{\text{Simulated Image}(i,j)}{\text{Simulated Flood Image}(i,j)} \times 10,000 \quad (7.2)$$

7.2.3 Monte Carlo Model Validation

Various tests were conducted to validate the MC model. The incident electron beam energy as well as the inherent and added filtrations were verified by measuring first and second half-value layer (HVL) for three beam energies 80, 100, and 120 kVp. The measured HVLs were obtained using a Barracuda kV meter (RTI Electronics AB, S/N: BC1-03050023) with R100 silicon diode detector (S/N: 03114). The Barracuda system was placed 155 cm from the source and the collimators were closed to a very small field size (2×2) cm^2 at 100 cm from the source. The simulated HVLs were obtained under the same conditions. A simulated spectrum was obtained at isocenter for a very small field size and the first and second HVL were derived from that spectrum [24]. An in-air kerma profile at 100 cm from the source, along the anode-cathode direction, was also measured using the Barracuda system and simulated using the phase space file for the 120 kVp beam.

The imaging detector model and the analytical program were tested by examining the detector response for various field sizes and thicknesses of solid water attenuating the radiation beam. Four field sizes were used ranging from (5×5) cm^2 to (40×40) cm^2 at 100 cm from the source and solid water slabs (0 to 24 cm) were placed in the beam, in front of the detector. Regions of interest (ROI) of (1.56×1.56) cm^2 were identified at the center of both the measured and simulated images and the signal was averaged over this region.

The complete CBCT geometry model was validated by comparing measured and simulated projection images for two phantoms: a cylindrical water phantom of 20 cm outer radius and 19 cm inner radius with acrylic walls, and the head of an anthropomorphic phantom. A field with the collimators fully open (43×43) cm^2 at 100 cm from the source) and a small field size (7×7) cm^2 at 100 cm from the source were used with the 120 kVp beam. The measured and simulated signals in the shadow of the collimator for the small field size were compared. This signal is produced by scattered particles, primary particles leaking through the collimator and extra-focal radiation. A comparison of this signal validates the model further by ensuring that the sum of scattered, leakage and extra-focal radiation is modeled properly. Profiles were obtained through the center of the water phantom images, the detector pixels were grouped 32×32, resulting in a pixel size of (0.62×0.62) cm^2 in both the measurements and the simulations.

7.2.4 Scatter Study

The impact of different imaging parameters on the amplitude and spatial distribution of the scattered radiation signal was studied using the MC model of the kV CBCT system. The particles stored in the phase space file scored after the collimators were transported through cylindrical water phantoms. Each particle was used 8 times to ensure an uncertainty on the scatter distribution below 15%. In all tests the distance between the source and the center of the phantom was fixed to 100 cm. The fan size (field size in the lateral direction) was fixed to 40 cm at 100 cm from the source. The cone size was varied from 5 cm to 40 cm at isocenter and the source-to-detector distance (SDD) was varied from 112 cm to 175 cm. Phantom diameters

ranging from 5 cm to 32 cm were considered. The detector was either centered or offset for larger phantoms. Projection images of the scattered radiation were calculated using the analytical program. Lateral and longitudinal profiles through the center of the images were extracted. The detector pixels were grouped 64 × 64, for a pixel size of (1.25 × 1.25) cm^2 to reduce the statistical uncertainty in the signal. The scatter-to-primary ratio (SPR) in a (1.25 × 1.25) cm^2 ROI was calculated and plotted against cone size, SDD and phantom diameter.

7.2.5 Scatter Correction Using Monte Carlo Technique

The MC scatter correction technique consists of the following steps described in figure 7–2. First a set of n ($n = 320$) measured kV CBCT projections $I_n(i,j)$ are acquired. These images are reconstructed and a set of reconstructed slices $R_z(x,y)$ is obtained. The reconstructed 3-dimentional (3D) image is transformed into a voxelized phantom for MC calculation by assigning a material and a density to every pixel according to their intensity. The second step consists in simulating the transport of photons through the voxelized phantom using the modified DOSXYZnrc program. The analytical program is used to obtain the scattered particle distribution in the detector for all projections, n. The energy deposited in the phosphor by the scattered particles is transformed to detector signal $S_n(i,j)$ using equation 2. The simulated scatter projections $S_n(i,j)$ are then subtracted from the original measured projections $I_n(i,j)$, to obtain scatter corrected projections $I_{cn}(i,j)$. These are then reconstructed to obtain the scatter corrected reconstruction $R_c(x,y)$. The 3D images are reconstructed using a Feldkamp filtered back projection algorithm on a plane with 512 × 512 pixels of a (0.05 × 0.05) cm^2 size and a 0.08 cm slice thickness.

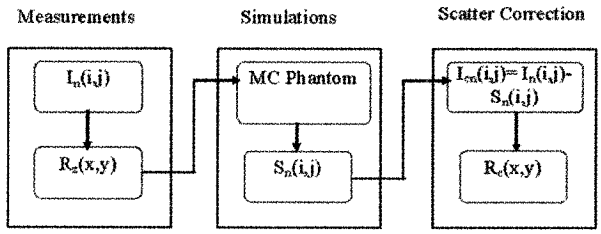

Figure 7–2: Schematic of the scatter corrected reconstruction process where I_n(i,j), S_n(i,j) and I_{cn}(i,j) are the n measured non-corrected, scatter simulated and scatter corrected projection images. R_z(x,y) and R_c(x,y) are the original and scatter corrected 3D reconstructions.

Preliminary testing of the procedure was done using a solid water phantom containing various contrast inserts and an anthropomorphic head phantom. The contrast phantom (figure 7–3) consists of a 16 cm diameter solid water phantom with 3 cm diameter cylindrical inserts made of simulated adipose tissue, breast tissue, liver tissue, brain tissue and Teflon mimicking cortical bone. The inserts are in the superior section of the phantom; the inferior section is made of uniform solid water. The contrast materials can be found in Table 7–1. The phantoms were centered at 100 cm from the source and the measured image sets were obtained with a 120 kVp beam, an open fan (12°) and cone beam (12°) and a 155 cm source to detector distance. This geometry closely approximates that of a system for CBCT guided radiotherapy (Synergy, Elekta). The MC simulations were run for 3×10^6 particles for each projection angle, for a total of 1.2×10^6 scattered particles in the phase space file scored at the detector. For the contrast phantom, contrast between the different material inserts and the surrounding solid water were computed before and after scatter correction and compared with theoretical values computed from the

nominal CT numbers of the inserts. The contrast is defined as the difference in the mean intensity of a (0.8×0.8) cm^2 ROI for water and a given material divided by the mean intensity found for solid water multiplied by 100. Profiles were also extracted from the reconstruction in the region of uniform water to investigate the influence of the correction on scatter-induced shading artifacts.

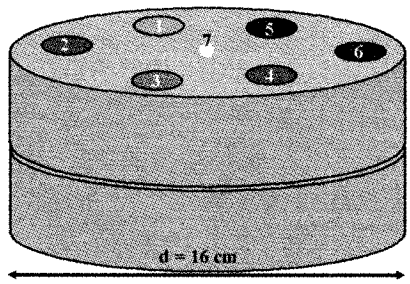

Figure 7–3: Schematic of the solid water contrast phantom of 16 cm diameter (d); the materials are identified using their label number in table 7–1.

Table 7–1: Contrast between different materials and solid water for the reconstruction of a contrast phantom, obtained with and without scatter correction. The theoretical values are obtained from the nominal CT numbers of the inserts.

Materials	Contrast (%)		
	Theoretical	Without scatter correction	With scatter correction
1- Adipose tissue	10	9	11
2- Breast	5	4	4
3- Brain	1	1	2
4- Liver	9	5	8
5,6- Teflon	100	71	82
7-Air	100	77	86

7.3 Results and Discussion

7.3.1 Validation of the Monte Carlo Model

Table 7–2 gives the measured and simulated, first and second HVL for the CBCT bench-top system for the three beam energies examined in this study: 80, 100, and 120 kVp. The measured and simulated first HVL agree within 2% for all beam energies while the second HVL agree within 3%. The agreement of the first and second HVL demonstrates the adequate modeling of the added and inherent filtration and correct incident electron energy. Profiles in the anode-cathode direction as well as the local percent difference obtained are found in figure 7–4; 90% of the profile points agree within 4%. The pixels within the field all agree within 4% . The heel effect is predicted correctly by the MC model which suggests that the target angle and composition are modeled properly.

Table 7–2: Measured and simulated first and second HVL in mm of Aluminum for three energies of the CBCT bench.

Energy (kVp)	1^{st} HVL Measurements (mm of Al)	1^{st} HVL Simulations (mm of Al)	1^{st} HVL Percent Difference (%)	2^{nd} HVL Measurements (mm of Al)	2^{nd} HVL Simulations (mm of Al)	2^{nd} HVL Percent Difference (%)
80	5.8	5.7	2	12.5	12.1	3
100	6.5	6.6	-2	14.7	14.6	1
120	7.7	7.6	1	17.0	16.8	1

The results of the validation tests for the MC imaging detector model and for the analytical program are presented in figure 7–5. The statistical uncertainties in the measurements are within 0.5%. The statistical uncertainties in the MC simulations and in the analytical program are within 1%. The measurements and the MC model agree within 2% and 5% for the variation in field size and in solid water thicknesses,

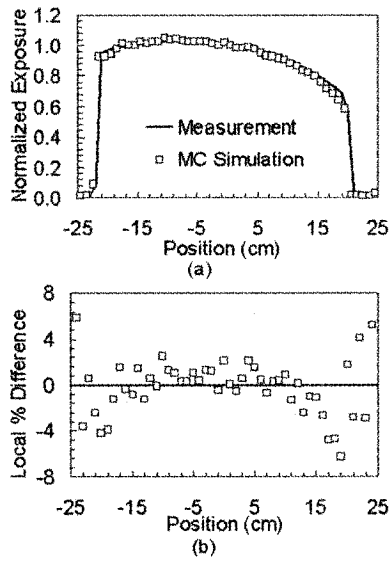

Figure 7–4: (a) Measured and simulated normalized exposure profiles along the anode-cathode direction for an open (43 × 43) cm^2 field, 120 kVp beam at 100 cm from the source and (b) the local percent difference between the simulated and the measured profiles. The local percent difference is defined as the difference between measurement and simulation divided by the measurement for a given position.

respectively. The same agreement is obtained between the measurements and the analytical program.

A comparison of measured and simulated profiles (from now on the simulations refer to the images obtained with the analytical program) for the projection image of a 20 cm diameter water cylinder is found in figure 7–6. Simulations and measurements agree within 8% as shown by the profiles comparison. The slight asymmetry in the profile is most likely due to the heel effect. Figure 7–7(a) and 7–7(b) show the simulated and measured images of the head of an anthropomorphic phantom. The uncertainties on the measurements are within 0.5% while the statistical uncertainties

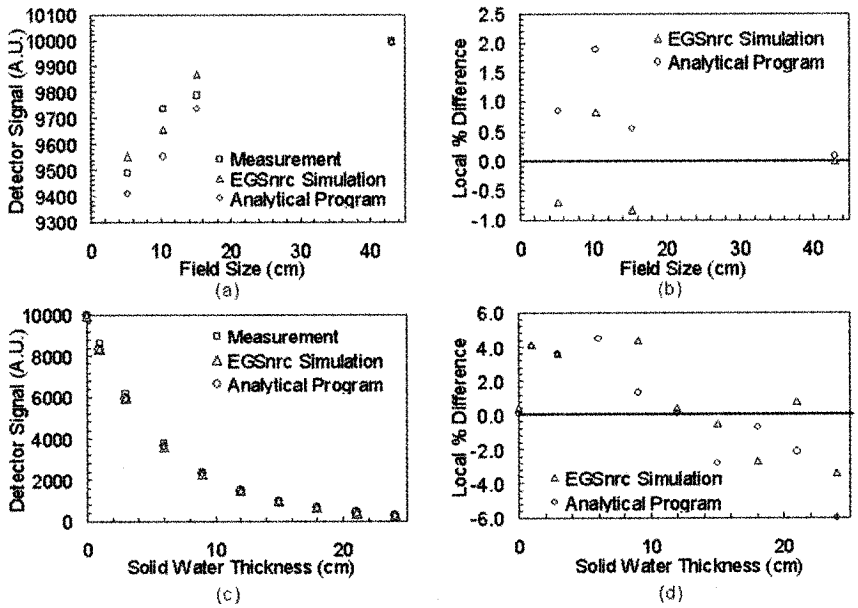

Figure 7–5: (a) Field size response of the detector and (c) its response for various thicknesses of solid water using a 120 kVp beam and a 155 cm source-to-detector distance, detector signal expressed in arbitrary units (A.U.); the percent difference between the simulations and the measurements for (b) the field size response and (d) the solid water attenuation.

on the simulations are within 5% for both the water cylinder and the anthropomorphic phantom. Figure 7–7(c) shows the spatial distribution of the percent difference between measurements and simulations for the anthropomorphic head phantom. The larger discrepancies occur in the phantom where bony anatomy is present. The percent difference distribution is shown in figure 7–7(d). Over 85% of the simulated and measured image pixels agree within 10%.

Further testing was conducted to ensure that the scattered particle transport and image formation is simulated properly. This was done by comparing the image

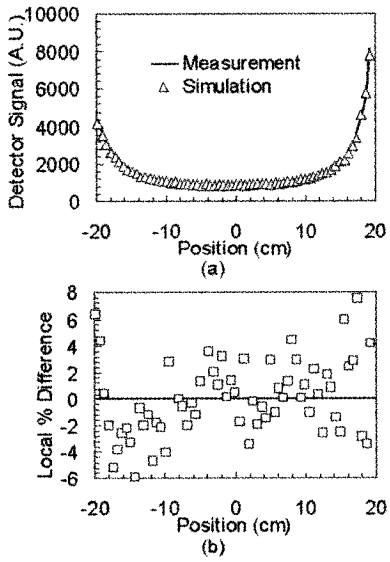

Figure 7–6: (a) Measured and simulated profiles of the projection image of a water cylinder (diameter = 20.6 cm) obtained using a 120 kVp beam and a (40 × 40) cm^2 field size at 100 cm from the source and (b) the local percent difference between the measured and simulated profiles.

production under the collimator for a (7 × 7) cm^2 field size with a 20 cm water cylinder. In this case, the particles reaching the detector in the collimator shadow are either scattered particles or particles that leaked through the collimator. Figure 7–8(a) shows a profile of the signal obtained under the collimator using measurements and simulations. The simulated signal was split into signal due to primary particles and due to scattered particles. Agreement between the measured and the total simulated signal is within 15% for 66% of the pixels. Although this is a large percentage difference it can be explained by the large uncertainties on the measurement and the simulations which are respectively within 12% and 10% for the detector signal scored under the collimator. The large uncertainty is due to the small number of

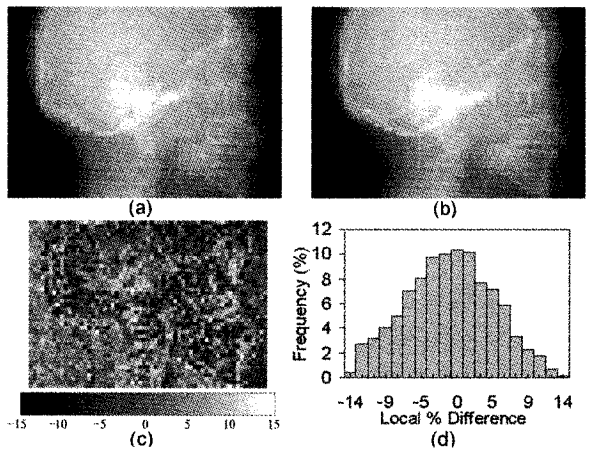

Figure 7–7: (a) Measured and (b) simulated images of the head of an anthropomorphic phantom obtained with a 120 kVp beam, (43 × 43) cm^2 field size, 100 cm source to phantom distance and 155 cm source-to-detector distance. (c) Spatial distribution of the local percent difference and (d) histogram of the local percent difference. The local percent difference is defined as the difference between measurement and simulation divided by the measurement for a given position.

particles reaching the detector under the collimator. Figure 7–8(a) also shows that the signal under the collimator is due to leaked, extra-focal and particles scattered by the phantom. The scattered particles contribute to 60% of the signal while 40% of the signal is due to leaked or extra-focal radiation. For a larger phantom (32 cm diameter) the contribution of scattered radiation increases to 88%. If the field size is increased to (10 × 40) cm^2 the contribution is 92%. Hence for a large phantom and large field sizes using the signal under the collimator to estimate the scatter is a good approximation. As the phantom diameter and the field size decreases this approximation becomes less accurate.

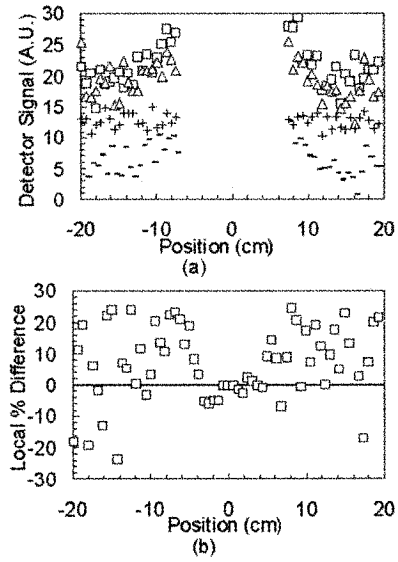

Figure 7–8: (a) Measured (□) and simulated (△) profiles of the projection image of a water cylinder (diameter = 20 cm) in the collimator shadow obtained using a 120 kVp beam and a (10.9 × 10.9) cm^2 field size for a 155 cm from source-to-detector distance. The simulated signal is divided in signal produced by the leaked and extra-focal particles (-) and by the scattered particles (+). (b) The local percent difference between the measured and simulated profiles.

7.3.2 Scatter Distribution

Figure 7–9 shows the effect of varying the cone size on the amplitude and the spatial distribution of the simulated scattered radiation. The SDD was fixed to 155 cm and a 20 cm diameter cylindrical water phantom was used. As shown in figure 7–9(a) and 7–9(b), the magnitude of the scatter signal does not vary with position in either the fan or the cone directions. These results are similar to the simulations by Malusek *et al* [15] and measurements by Siewerdsen and Jaffray [3]. Figure 7–9(c) shows the effect of varying the cone size and energy on the SPR.

As previous studies have shown using measurements [10] and simulations [12] that varying the energy does not impact on the SPR. However, when looking at the scatter signal only, it was found that the scatter signal increases by 40% for an energy variation of 80 kVp to 120 kVp. The SPR varies linearly with cone size for small cone sizes. A similar relationship was observed by previous investigators [3, 10, 12, 15].

Figure 7–10(a) shows the effect of the distance between the phantom and the detector on the scattered radiation spatial distribution. This distribution was obtained with a 10 cm cone size, a 120 kVp beam and a 20 cm diameter water cylinder. As the distance between the phantom and the detector decreases, the scattered radiation profile develops more shape, going from a constant across the detector to a distribution with elevated scatter signal near the central axis. Particles are more likely to scatter when they go through more attenuating material, hence less scattered particles are produced at the sides of the cylindrical phantom. MC simulations tracking of the positions where interactions occur in the phantom showed that 70% of the interactions happen in a 10 cm wide central portion of the beam intersecting a 20 cm diameter cylindrical phantom. These simulations also showed that of the particles that reach the detector and undergo a scatter event 60% have only one interaction and only 20% of the particles have three or more interactions. Particles undergoing many interactions either never reach the detector or are absorbed in the phantom. As shown in figure 7–10(b), the SPR decreases rapidly with increasing SDD. The SPR was found to decrease from 0.5 to 0.38 when the air gap between the phantom and the detector was increased from 25 cm to 35 cm. Other investigators have observed [3, 10, 12, 13, 15, 25] and predicted [26] the air gap effect. For example,

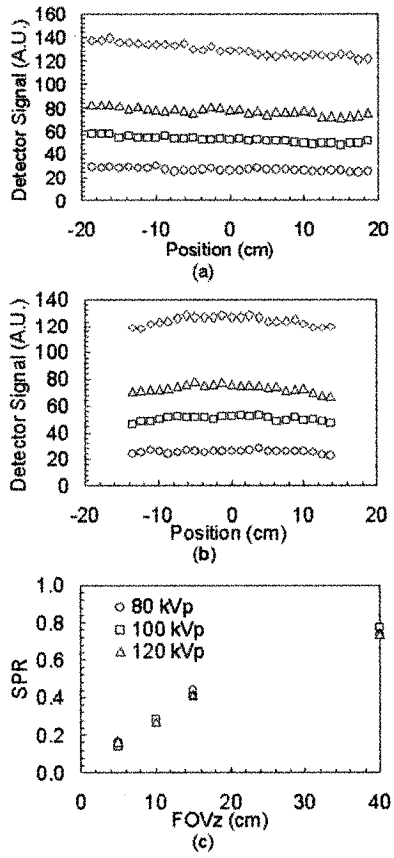

Figure 7–9: (a) Longitudinal and (b) lateral profiles taken at the central position of the simulated scattered particle spatial distribution for various cone sizes (represented by 5 cm - ○, 10 cm - □, 15 cm - △, 40 cm - ◇) , a 120 kVp beam, 155 cm source-to-detector distance and 20 cm diameter cylindrical water phantom. (c) Scatter-to-primary ratio (SPR) of a ROI at the center of the detector for different cone sizes (field of view (FOVz)) and beam energies.

Kwan *et al* [10] showed that for a 14 cm cylindrical breast phantom the SPR goes from 0.49 to 0.42 for air gaps of 27.5 cm and 37.5 cm.

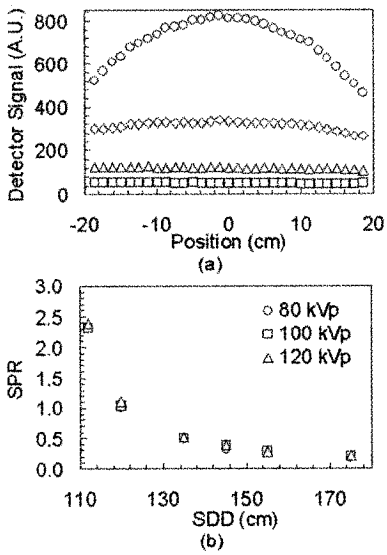

Figure 7–10: (a) Longitudinal profiles taken at the central position of the simulated scattered particle spatial distribution for various source-to-detector distances (SDD) (represented by 112 cm - ○, 120 cm - ◇, 135 cm - △, 155 cm - □), a 120 kVp beam, 10 cm cone size and 20 cm diameter cylindrical water phantom. (b) Scatter-to-primary ratio (SPR) of a ROI at the center of the detector for different SDD and beam energies.

Figure 7–11(a) and (b) show profiles of the scatter distribution for cylindrical water phantoms of different diameters for a 120 kVp beam and a 10 cm cone size. The profiles in figure 7–11(a) were obtained with a large SDD of 155 cm while the profiles in figure 7–11(b) were obtained with a small SDD of 112 cm. Increasing the diameter of the phantom first increases the amount of scatter produced in the phantom, eventually a maximum is reached beyond which point the amount of scatter absorbed by the thick phantom becomes more important and hence the amount of scatter signal decreases. The maximum amount of scatter was found for a phantom

diameter of 15 cm. This effect was observed for all energies and for different SDD. It was found that the scattered particle profiles obtained with the large SDD do not reflect the structure of the phantom other than a change in amplitude. On the other hand, when using a smaller SDD the smaller diameter phantoms have a narrower peaked profile. Previous studies [15, 16] have shown that for large SDD the scatter distribution does not reflect the phantom geometries even when inhomogeneities are present. Figure 7–11(c) shows the effect of offsetting the detector on the scatter distribution. Instead of being constant across the detector, the amount of scatter now increases as we go toward the portion of the detector covered by the phantom. Figure 7–11(d) shows that the SPR increases with cylinder size, as observed by previous investigators [10, 12, 15]. The varying air gap is also responsible for the different curves obtained for the 112 cm SDD and the 155 cm SDD.

7.3.3 Scatter Correction Using Monte Carlo Technique

Figure 7–12 shows the reconstructed central slice of the contrast phantom with and without MC scatter correction as well as profiles through the water portion of the contrast phantom. The non-corrected slice shows a streaking artifact between the two Teflon inserts. Although the streaking artifact is still present when the image is corrected for scatter, it is more subtle. The streaking may also be due to photon starvation or to beam hardening and hence cannot be completely corrected. When looking at the uniform solid water portion of the non-corrected slice (figure 7–12), it is obvious that the gray levels are non-uniform and that the center appears darker. As shown in the profiles, the cupping artifact is less pronounced in the scatter corrected reconstruction. The relative deviations between voxel values in the

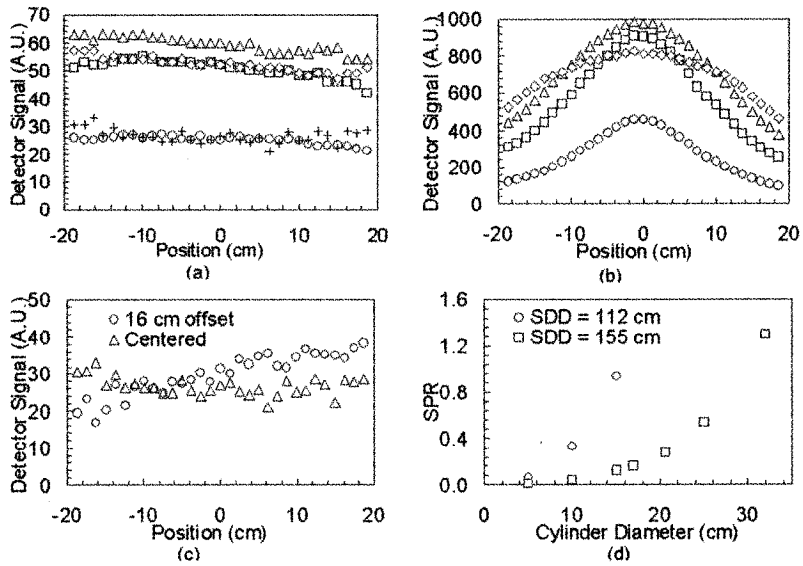

Figure 7–11: Longitudinal profiles taken at the central position of a simulated scattered particles spatial distribution for various cylindrical phantom diameters (D) (represented by 5 cm - ○, 10 cm - □, 15 cm - △, 20 cm - ◇, 32 cm, plus signs) , for a 120 kVp beam and for (a) a 155 cm source-to-detector distance (SDD) or (b) a 112 cm SDD. (c) Longitudinal profiles taken at the central position of a simulated scattered particles spatial distribution for a 32 cm cylindrical phantom centered and offset by +16 cm. (d) Scatter-to-primary ratio of a ROI at the center of the detector for different cylindrical phantom diameters and SDD for a 120 kVp beam.

center of the reconstruction compared to those at the edge were found to be 10% for the non-corrected image and 1% for the corrected image. The contrast is also slightly improved when the scatter correction is applied as shown in Table 7–1, and the contrast values are closer to the theoretical values.

Figure 7–13 shows a reconstructed slice of the anthropomorphic head phantom. In the case of a small phantom such as this one the SPR is around 30% for a 155 cm SDD and an open field. Hence the scatter contribution to the image is fairly small,

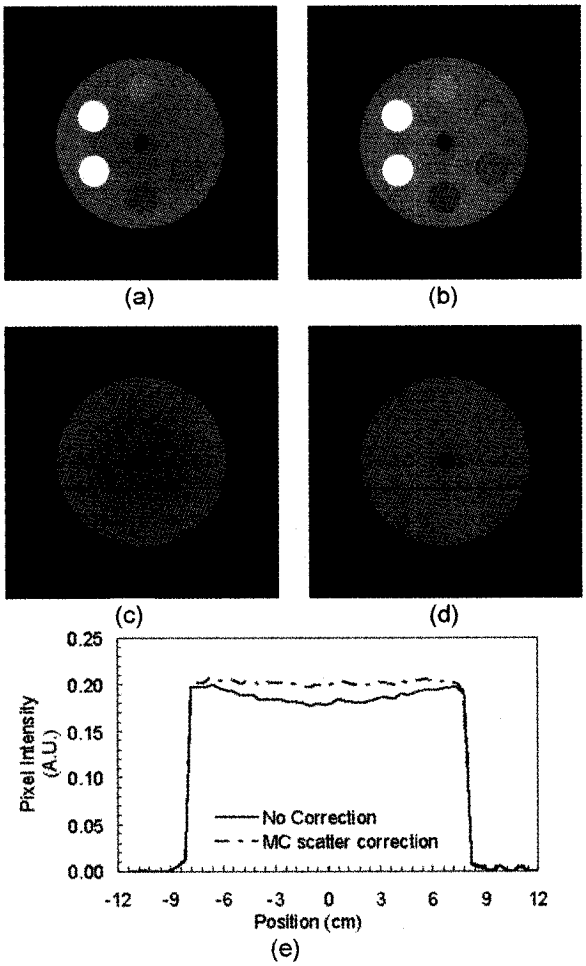

Figure 7–12: Central slice of the contrast phantom reconstructed using (a) no scatter correction and (b) MC scatter correction. Slice in the uniform solid water portion of the contrast phantom reconstructed using (c) no scatter correction and (d) MC scatter correction. (e) Profile through the uniform water portion of the contrast phantom for the non-corrected and the corrected reconstruction, the profile position is indicated by the dark line in (c and d).

however correcting for scatter still leads to image quality improvements. In figure 7–13, the corrected reconstruction exhibits a more uniform brain tissue portion.

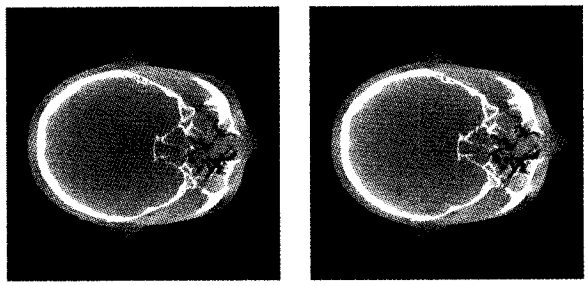

Figure 7–13: Slice of the anthropomorphic head phantom reconstructed using (a) no scatter correction and (b) MC scatter correction.

The simulations for scatter correction were run on a Pentium 4 Xeon processor 2.8 GHz for 430 hours. On a 20 computers cluster, which can now be readily available at acceptable costs, the simulation time can be reduced to 21.5 hours. This is still a significant amount of time; however, it is possible to reduce the simulation time by a factor of up to 200 by reducing the number of projections that are simulated, by increasing the phantom voxel size or by reducing the detector resolution at the cost of a lesser image quality. This was recently reported elsewhere [27].

7.4 Conclusion

In this paper MC simulations have been used to investigate the scatter contribution in kV-CBCT projection images. Findings from previous studies on the effect of varying the fan size and the source to detector distance on the amplitude of scattered radiation were confirmed. Moreover, it was found that for small distances between the phantom and the detector the scatter distribution is dependent on the phantom geometry; this is not the case for larger distances. Previous studies have shown that

when large inhomogeneities are present in a phantom, such as lung in a chest phantom, the scatter distribution is geometry dependent [28]. The scatter distribution will also be affected by the detector position e.g. if the detector is offset. In such cases, MC simulations become a useful tool to predict the scatter distribution.

The MC scatter predictions were used to correct projection images. Preliminary testing of this procedure included a contrast phantom and to an anthropomorphic head phantom. It was found that the scatter correction improves the contrast slightly and reduces significantly the cupping and streaking artifacts. The computation time necessary for this correction procedure is still significant. However, we believe that with further improvements in computer power this technique may eventually be clinically viable. Future testing on larger phantoms where the scatter contribution is more important will be necessary to show a significant improvement in contrast. Future work will also include correction of scatter for kV CBCT patient scans in anatomical region such as the chest where MC simulations are the most useful.

In the previous paper, a MC model of the kV CBCT bench-top was developed. This model was used to characterize the scattered radiation produced under different condition. The model was also used to develop a scatter correction technique which was shown to improve contrast and reduce artifacts. However, the required computation time is still significant; 21.5 hours on a 20 computers cluster.

In this second paper, published in the *Proceedings SPIE Physics of Medical Imaging*, we show how it is possible to reduce the scatter correction technique calculation time so that it is possible to use it in a clinical setting.

Title: Scatter correction for kilovoltage cone-beam computed tomography (CBCT) images using Monte Carlo simulations

Authors: G Jarry, S A Graham, D A Jaffray, D J Moseley, F Verhaegen

Published in the SPIE proceedings on Medical Imaging, 6142, 1634-1643 (2006)

Abstract

In this work, Monte Carlo (MC) simulations are used to correct kilovoltage (kV) cone beam computed tomography (CBCT) images for scattered radiation. All images were acquired using a kV CBCT bench-top system composed of an x-ray tube, a rotation stage and a flat-panel imager. The EGSnrc MC code was used to model the system. BEAMnrc was used to model the x-ray tube while a modified version of the DOSXYZnrc program was used to transport the particles through various phantoms and score phase space files with identified scattered and primary particles. An analytical program was used to read the phase space files and produce image files. The scatter correction was implemented by subtracting Monte Carlo predicted

scatter distribution from measured projection images; these projection images were then reconstructed. Corrected reconstructions showed an important improvement in image quality. Several approaches to reduce the simulation time were tested. To reduce the number of simulated scatter projections, the effect of varying the projection angle on the scatter distribution was evaluated for different geometries. It was found that the scatter distribution does not vary significantly over a 30-degree interval for the geometries tested. It was also established that increasing the size of the voxels in the voxelized phantom does not affect the scatter distribution but reduces the simulation time. Different techniques to smooth the scatter distribution were also investigated.

7.5 Introduction

Kilovoltage (kV) cone beam computed tomography (CBCT) images are subject to an important contribution from scattered radiation. This effect is more important in CBCT than in fan-beam CT due to the larger cone angle and to the 2D detector used to acquire the images. This scatter contribution has for effect to degrade the image quality by degrading the contrast, increasing the noise and introducing shading artifacts [3]. The shading artifacts are similar to the one caused by beam hardening and can be divided in two categories: (1) cupping artifacts where the voxel values in the image of a uniform phantom are reduced in the center of the phantom and non-uniform and (2) streaking artifact in which the voxel values between two dense objects are reduced forming a streak. Techniques to reduce the scatter contributions include optimization of the imaging geometry such as increasing the air gap between the object and the detector and using anti-scatter grids [5, 29]. Other scatter correction

techniques are based on analytical prediction of scatter [6] and empirical methods [5, 7, 8] such as beam stop array techniques.

Monte Carlo (MC) simulations have previously been used to study the scattered radiation distribution in diagnostic radiology and they have shown to be the most successful method for the investigation of the production of scattered particles in a medium [12–16]. Recently Malusek *et al* [15] used MC simulations to predict the scattered radiation in CBCT projection images. They used a simplified CT scanner geometry which consisted of a point source emitting mono-energetic photons or a spectrum of photons, different phantoms and a cylindrical detector array. Ay and Zaidi [16] used the MCNP4C MC code to model fan and cone beam systems. They studied the effect of bow-tie filters, phantom sizes and septa length on the scatter distribution. Advances in MC simulations and in computer power now allow for more complete models of the x-ray source, scattering material and detector. However MC simulations are still costly in terms of computation time especially in the case of tomographic geometry where many projections must be simulated. In this study, it is shown that MC predictions of scatter distribution can be used to correct for scatter in kV CBCT images, and that different techniques can be used to reduce the simulation time. The scatter correction improves contrast and reduces the scatter induced artifacts.

7.6 Materials and Methods

7.6.1 Measurements

A kV-CBCT bench top system was used to acquire all measured images. The bench-top system consists of an x-ray tube, a rotating platform and a flat panel

detector (figure 7–14(a)). All three components are mounted on an optical bench and can be translated in three dimensions. The x-ray tube is a Varian Rad-94 with a sapphire housing. It has a 14° tungsten-rhenium-molybdenum-graphite target. To simplify the modeling of the x-ray tube, the mirror and the cross air were removed and replaced by an equivalent aluminum thickness. The total added filtration consists of 3.711 mm aluminum and 0.122 mm copper. The collimation is provided by two ~2 mm thick tungsten shutters. The detector is a Varian Paxscan 4030A amorphous silicon digital x-ray detector with an active area of (40×30) cm^2. It consists of a carbon fiber section overlying a scintillating layer of CsI:Tl and a (2048×1536) pixels^2 aSi light sensor photodiode array. The acquisitions for the reconstructed images consisted of 320 projections taken 1.125 apart, with a 120 kVp beam. The distance between the source and the center of the phantom was set to 100 cm and the source-to-detector distance was set to 155 cm. The field size was set to (40×40) cm^2 The measured projections are calibrated according to equation 7.3.

$$\text{Calibrated Image}(i,j) = \frac{\text{Image}(i,j) - \text{Dark Image}(i,j)}{\text{Flood Image}(i,j) - \text{Dark Image}(i,j)} \times 10000 \qquad (7.3)$$

7.6.2 Monte Carlo Model

The BEAMnrc MC code system [20] was used to build an x-ray tube model for the Rad-94 x-ray tube according to the manufacturer's specifications. A schematic diagram of the x-ray tube model is shown in figure 7–14(b). The model includes the target modeled as tungsten only, the exit window, the added filtration and the collimation. Various collimation settings were modeled. The energy of the primary

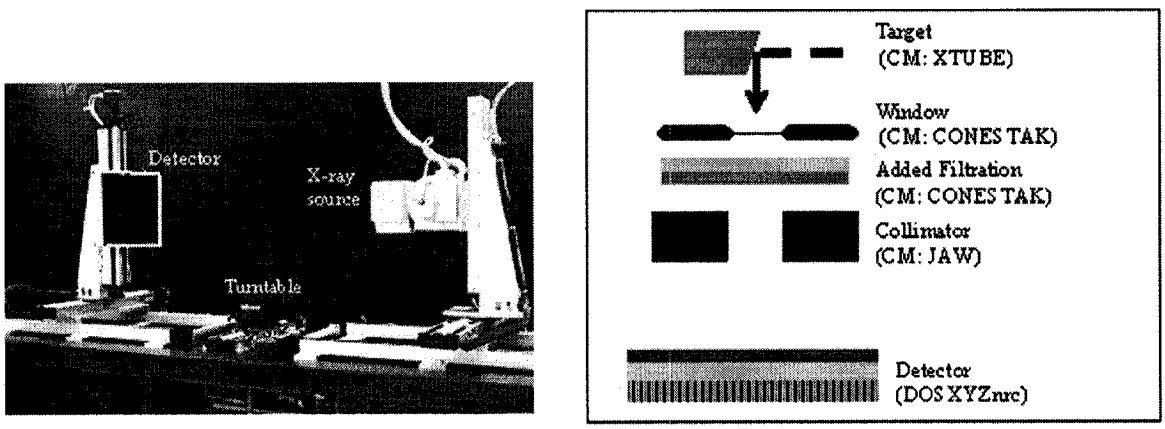

(a) (b)

Figure 7–14: Photograph of the CBCT bench with different components identified and a schematic illustration of the Monte Carlo model for the CBCT bench with the component modules (CM) that were used. Source-to-axis distance (SAD) and source-to-detector distance (SDD) are identified.

electrons hitting the target was set to the nominal energy of the beam. The photon transport cut-off was set to 0.01 MeV while the electron transport cut-off was set to 0.531 MeV in all component modules. 40 billion primary electrons were incident on the target. Phase space files, in which the position, direction and energy of the particles are stored, were obtained just below the added filtration and were transported without any recycling through the different collimator settings where a second phase space file was obtained. The phase space file contained 25,000 particles/cm^2 for a 120 kVp beam. The model was validated against measurements [30]. The incident electron beam energy as well as the inherent and added filtrations were verified by measuring first and second half-value layers (HVL). The measured and simulated HVL values agree within 3%. Measured and simulated in-air profiles along the anode-cathode direction agree within 6%.

The phase space file particles were transported through different voxelized geometries using a modified version of the DOSXYZnrc program. This modified version tags the particles when they undergo scatter interactions hence identifying the scattered and primary particles. A phase space file is collected around the phantom; this phase space file can include all particles, only the scattered particles or only the primary particles. Electron transport was not simulated since in the keV energy range, it can be assumed that electrons deposit their energy locally. This contributes to reduce the simulation time.

The DOSXYZnrc [21] program was used to develop a model of the PaxScan 4030A imaging panel. The simulation time for the particle transport through the imaging detector can be reduced by using an analytical program to obtain the image instead of a full MC simulation through the detector layers. The analytical program reads the phase space file scored at the detector position, from which it gets each particle energy, position and direction. The dose deposited in the active layer of the imager is obtained by reading the dose corresponding to the particle energy in a dose response file and scaling it with the particle path length. The analytical program was used to obtain all simulated images. In order to minimize the statistical uncertainty, the default pixel size was set to (0.62×0.62) cm^2. The simulated images were calibrated according to equation 7.4.

$$\text{Simulated Calibrated Image}(i,j) = \frac{\text{Simulated Image}(i,j)}{\text{Simulated Flood Image}(i,j)} \times 10000 \quad (7.4)$$

The detector model and the analytical program were tested by looking at the detector response to various field sizes and thicknesses of solid water on top of the detector [30]. The measurements and the MC model agree within 6% for both the field size and solid water response; the same agreement was obtained between the measurements and the analytical program predictions.

The complete CBCT model was validated by comparing measured and simulated projection images. Images of two phantoms were simulated and measured: a cylindrical water phantom and the head of an anthropomorphic phantom. The water cylinder projections agreed within 8% while the anthropomorphic head phantom projections agreed within 10% for more than 85% of the pixels.

7.6.3 Scatter Correction Technique

The MC scatter correction technique consists of the following steps as described in figure 7–15. First a set of n kV CBCT projections $I_n(x,z)$ are acquired. These images are reconstructed and a set of reconstructed slices R(x,y) is obtained. These reconstructions are transformed in a MC voxelized phantom by assigning a material and a density to every voxel according to their intensity. The next step consists in simulating the transport of photons through the voxelized phantom using the modified DOSXYZnrc program. The analytical program is used to obtain the scatter particle distribution ($S_n(x,z)$) at the imager for all projections n. The simulated scattered projections are then subtracted from the original measured projections, to obtain scatter corrected projections ($I_{cn}(x,z)$). These are then reconstructed to obtain the scatter corrected reconstruction ($R_c(x,y)$). The slices are reconstructed

using a Feldkamp's filtered back projection algorithm on a 512 × 512 plane with (0.05 × 0.05) cm^2 pixels and a slice thickness of 0.08 cm.

This procedure was applied to a contrast phantom and the head of an anthropomorphic phantom. The contrast phantom consists of a 16 cm diameter solid water phantom with 3 cm diameter cylindrical inserts made of material equivalent to adipose tissue, breast tissue, liver tissue, brain tissue and Teflon. A schematic diagram of the phantom can be found in figure 7–16 and a list of the corresponding materials in table 7–3.

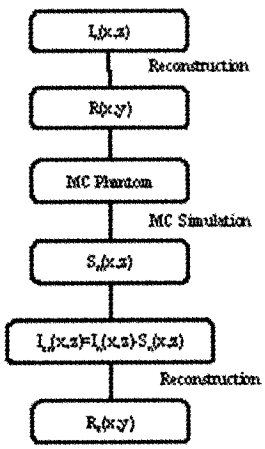

Figure 7–15: Schematic of the scatter corrected reconstruction process where $I_n(x,z)$, $S_n(x,z)$ and $I_{cn}(x,z)$ are the n measured non-corrected, scatter simulated and scatter corrected projection images. R(x,y) and $R_c(x,y)$ are the original and scatter corrected reconstructions.

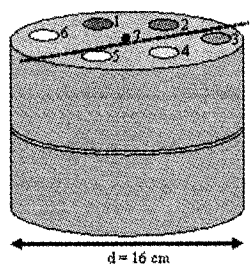

Figure 7–16: Schematic representation of the solid water contrast phantom, the dotted line indicates the position of the profile taken in the uniform portion of the phantom; the materials are identified in table 7–3.

7.6.4 Simulation Time Reduction Techniques

Three methods were investigated to reduce the simulation time. The first method consists in reducing the number of simulated projections. Given that the scatter distribution is similar for neighboring projection angles, it is possible to group these projections together. The scatter prediction for the median angle of the group can then be used to correct all projections that are part of that group. The number of simulated scatter projections can be reduced significantly in that way.

The second technique consists in reducing the number of voxels in the MC phantom. Decreasing the number of voxels decreases the simulation time by reducing the number of boundary crossings for photons. Increasing the voxel size will also decrease phantom resolution; however, good phantom resolution may not be essential in predicting scatter distribution.

The last group of techniques consists in smoothing the detector signal. Although this does not directly reduce the simulation time, it reduces the uncertainty in the simulated detector response and therefore the simulations can be run for a smaller number of particles. The smoothing methods consisted of an averaging method and a surface fitting method. The averaging method was implemented by increasing the size of the detector pixels. The surface fitting method consisted in fitting a second order polynomial to the scatter distribution. Noise can be removed by using the fitted function instead of the actual scatter distribution.

These techniques were tested on both the anthropomorphic head phantom and the contrast phantom. The effect of the simulation time reduction technique on the image quality of the contrast phantom reconstructed slice were evaluated using

contrast, contrast-to-noise ratio (CNR), signal-to-noise ratio (SNR), pixel by pixel comparison as well as a qualitative and quantitative evaluation of the artifacts. The contrast and the CNR were evaluated by looking at the difference in average intensity value in a (0.8×0.8) cm^2 region of interest between the insert material and the surrounding solid water relative to the surrounding solid water average intensity. The theoretical value for the contrast was obtained by using the nominal CT numbers of the inserts. The noise was determined using the standard deviation in pixel intensity for a (0.8×0.8) cm^2 region of interest in the solid water region. The cupping artifact was evaluated using Tcup, the relative deviations between voxel values in the center of the reconstruction compared to those at the edge.

7.7 Results and Discussion

7.7.1 Correction of Scattered Radiation

Figure 7–17 shows the central reconstructed slice of the contrast phantom and the anthropomorphic phantom obtained with and without scattered correction. The scattered projections were acquired for all projection angles with the phantom voxel size set to (0.16×0.16) cm^2 and no smoothing was applied. A reduction in the streaking artifact between the two Teflon inserts at the left side of the contrast phantom is observed when the image is corrected for scatter. A quantitative evaluation of the contrast (table 7–3) shows an improvement in contrast. The contrast is improved by up to 10% when looking at the contrast between air and solid water. For material with non-negligible contrast values, the contrast values are closer to the theoretical contrast values when applying the scatter correction. However as shown in table 7–3, the CNR and the SNR both decrease, this is due to the noise in the predicted

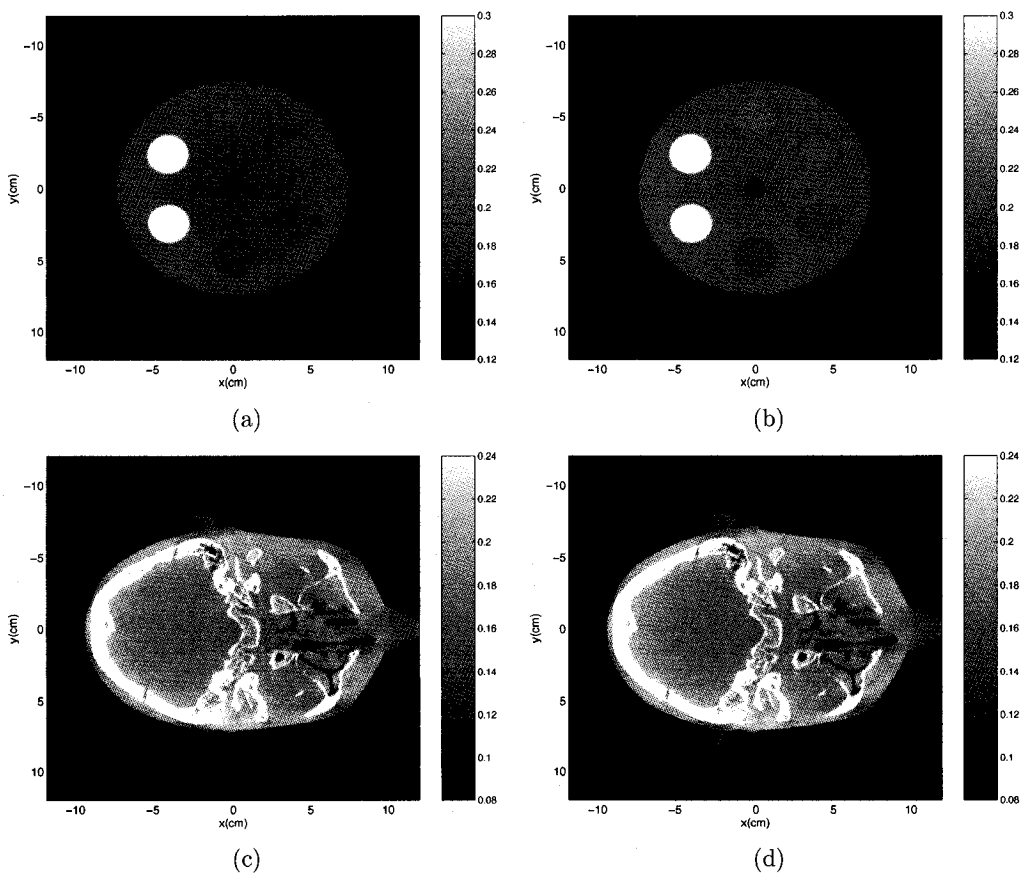

Figure 7–17: Reconstructed slice of the (a,b) contrast phantom and (c,d) anthropomorphic phantom with (a,c) no scatter correction and (b,d) with scatter correction.

scatter distribution which has for effect to amplify the noise in the reconstruction. This increase in noise is visible both in the contrast phantom reconstruction and in the anthropomorphic head reconstruction. Figure 7–18 shows profiles through the uniform solid water portion of the contrast phantom; a reduction in the cupping artifact when the image is corrected for scattered radiation is observed. Tcup values were found to be 12% for the non corrected data and ~0% for the corrected data.

Table 7–3: Contrast and contrast-to-noise ratio between different material inserts and solid water for the reconstruction of a solid water phantom without scatter correction (original) and with scatter correction using different simulation time reduction techniques. Signal-to-noise ratio (SNR) obtained in the solid water region and Tcup the relative difference between intensities at the center and at the edge of the uniform solid water portion of the phantom.

Material	Theoretical	Original		Corrected (320 projections)		Corrected (20 Projections)		Corrected (1.25 cm voxel size)		Corrected (Smoothed by averaging)		Corrected (Smoothed by fitting)	
	C (%)	C (%)	CNR	C (%)	CNR	C (%)	CNR	C (%)	CNR	C (%)	CNR	C (%)	CNR
1-Adipose	10	9	6	11	3	11	2	8	4	8	5	8	6
2-Breast	5	4	3	4	0	4	1	0	0	1	0	1	3
3-Brain	1	1	0	2	1	1	0	2	1	1	1	2	1
4-Liver	9	5	3	8	4	7	1	10	5	10	6	9	5
5,6-Teflon	100	71	47	82	34	82	16	76	42	77	45	77	48
7-Air	100	77	52	86	39	86	17	87	47	86	51	87	50
SNR	-	67		45		20		55		59		58	
Tcup	-	12		0		3		1		1		2	

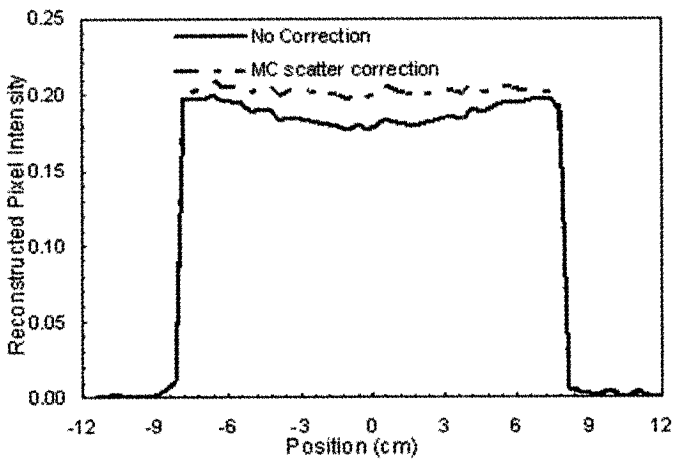

Figure 7–18: Profile through the uniform water portion of the contrast phantom from the non-corrected and the corrected reconstruction (320 projections).

7.7.2 Methods to Reduce the Computation Time

The effect of changing the projection angle on the scatter distribution is shown in figure 7–19. In the case of symmetric geometry such as the contrast phantom the scatter distribution does not change significantly with projection angle. For the anthropomorphic head, which is not a symmetric geometry, similar scatter distributions are obtained for intervals up to 40 degrees. The number of projections that can be grouped together is geometry dependent but can be estimated for patients by simulating the scatter distribution for anthropomorphic phantoms of different sizes. Given that it is not necessary to generate a scatter distribution for every projection angle, the simulation time can be reduced as shown in table 7–4.

Figure 7–20 shows how the scatter distribution varies when the size of the phantom voxels is increased. The voxel size can be increased up to 1.2 cm on each of the three voxel sides without changing the scatter distribution, both in the case of a simple geometry such as the contrast phantom and in the case of a more complex geometry such as the anthropomorphic head. Increasing the voxel size will reduce the simulation time as shown in table 7–4.

Both smoothing techniques, the averaging and the fitting, were found to produce similar results, but the polynomial fit reduces the noise more efficiently than the averaging technique but requires more computation time.

Figure 7–21 shows the reconstructed central slice of the contrast phantom using different computation time reduction techniques, a pixel by pixel ratio map and a histogram of the ratio distribution. The histogram represents the ratio obtained for the pixels inside the phantom reconstruction only. The reconstructions obtained

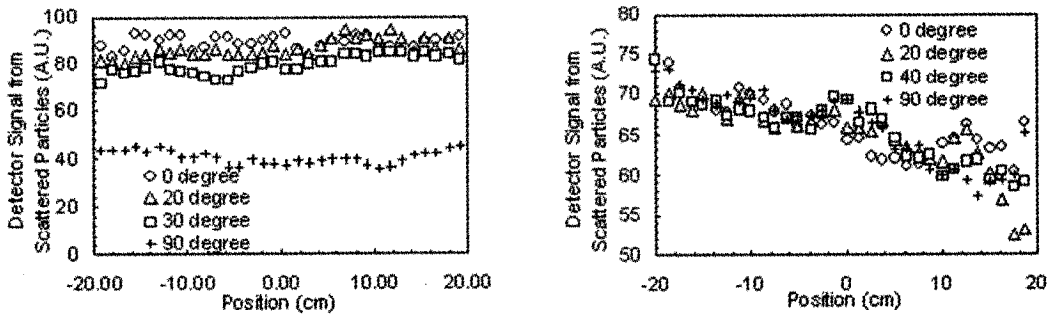

(a) (b)

Figure 7–19: Profiles of the scatter distribution for different projection angles for (a) the anthropomorphic head phantom, field size used is (10 × 40) cm^2 and (b) for the contrast phantom, field size used is (40 × 40) cm^2.

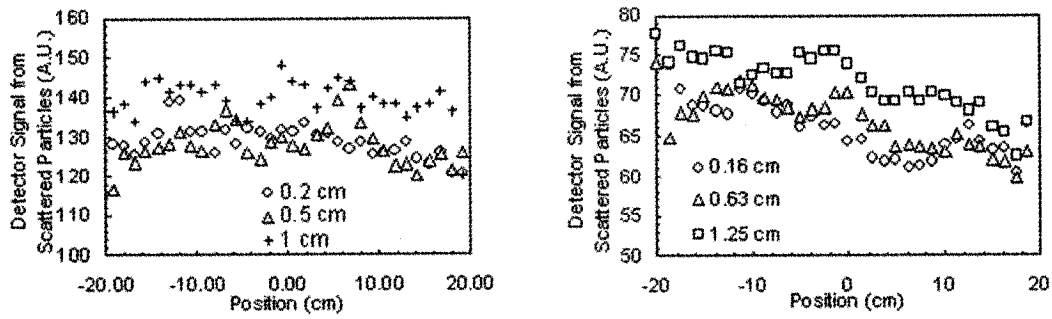

(a) (b)

Figure 7–20: Profiles of the scatter distribution for different phantom voxel sizes for (a) the anthropomorphic head phantom and (b) for the contrast phantom, the field size used is (40 × 40) cm^2 for both phantoms.

with and without the time reduction techniques are very similar; in all cases the pixel intensities agree within 5% for pixels inside the phantom. Pixels outside the phantom do not agree as well. As shown in table 7–3, the improvements in contrast and in Tcup are preserved for all time reduction techniques. However, when decreasing

the number of scatter projections, the SNR and the CNR are reduced by a factor of almost 2 compared to when all projections are used. This effect is not observed when increasing the phantom voxel size. The smoothing techniques preserve the improvement in contrast and Tcup. Moreover, the SNR and the CNR are improved by a factor of 1.3 compare to the original reconstruction. In fact the SNR is now almost back to what it was before the scatter correction. By combining these techniques it is possible to reduce the simulation time by a factor of more than 200 while at the same time reducing the noise in the image.

Table 7–4: Factor indicating the reduction in simulation time when obtaining the scatter distributions using different number of projections and different voxel sizes.

	Number of Projections		
Voxel Size	320	40	20
(0.16 × 0.16 × 5.00) cm^3	1.000	0.125	0.063
(0.63 × 0.63 × 5.00) cm^3	0.160	0.020	0.010
(1.25 × 1.25 × 5.00) cm^3	0.078	0.010	0.005

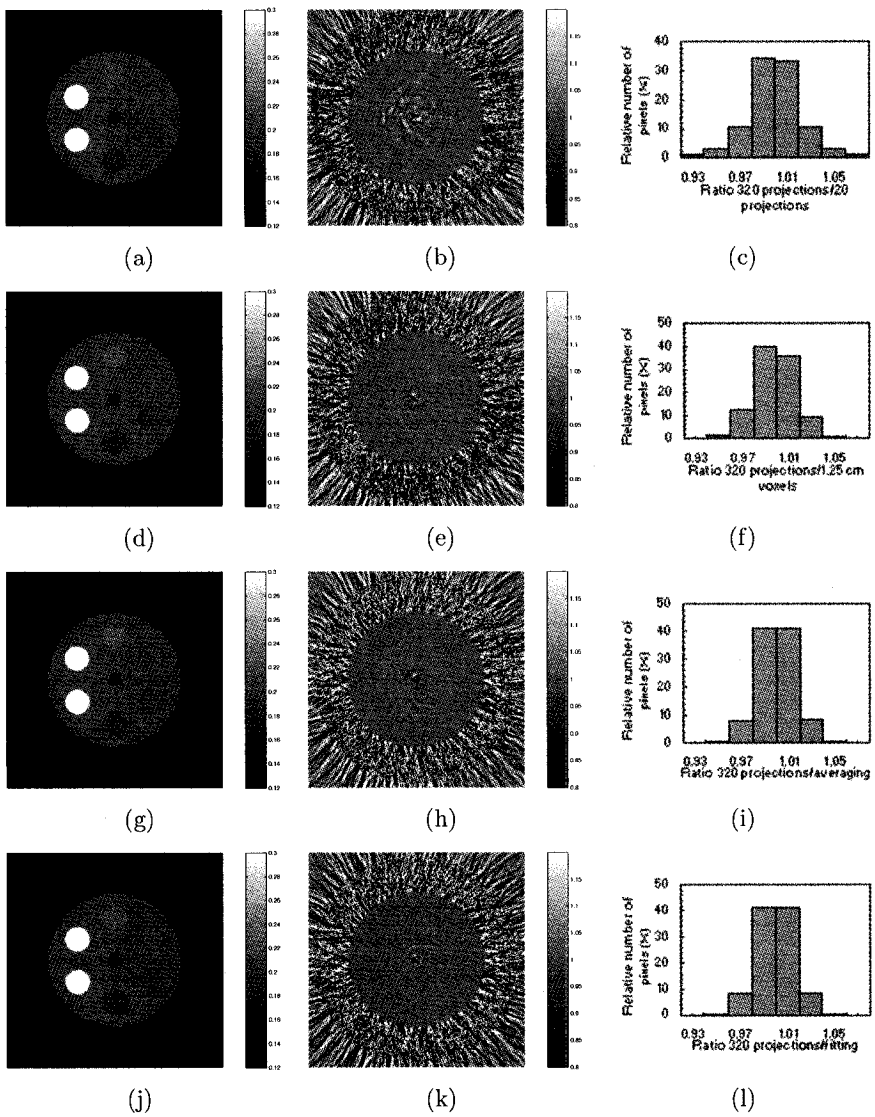

Figure 7–21: Reconstructed central slice of the contrast phantom using different time reduction techniques: (a) using only 20 scatter projections, (d) using (1.25 × 1.25) cm^2 phantom voxels, (g) using the averaging smoothing technique and (j) using the second order polynomial fitting smoothing techniques. (b)(e)(h)(k) Pixel by pixel ratio of the reconstructed slice using no time reduction technique to the reconstructed slice using time reduction technique and the (c)(f)(i)(l) corresponding histogram of the ratio for the pixels within the contrast phantom.

7.8 Conclusion

MC simulations were used to develop a method to correct kV CBCT images for scatter contribution. An improvement in contrast and a reduction in streaking and cupping artifacts were observed once the correction was applied; however CNR and SNR were reduced. Different methods were investigated to reduce the simulation time; these methods consist in decreasing the number of simulated projections, increasing the size of the phantom voxels and smoothing the scatter distributions. These techniques were found to reduce the simulation time by a factor of 200 if applied in conjunction without significantly affecting the results obtained with the scatter correction technique.

In this chapter, we have shown that it is possible to improve the quality of kV CBCT images by correcting for the scattered radiation using MC simulations. We have shown that the scattered particles distributions are not highly dependent on the imaging geometry, making it possible to simplify the Monte Carlo models. The simplifications can reduce the simulation time. Eventually, a database of pre-simulated scattered distributions for various patient sizes and anatomical regions could be produced and used for instantaneous scatter correction.

Improving the image quality of kV CBCT is an essential part of treatment verification. A better soft tissue contrast will improve patient positioning by allowing alignment based on soft tissue structures. Moreover correcting for scatter reduces shading artifacts and improves the accuracy of the reconstructed CT numbers. CT number accuracy is essential if one wants to use the CBCT scan for dose calculation or dose reconstruction.

References

[1] Jaffray D A, Siewerdsen J H, Wong J W, and Martinez A A. Flat-panel cone-beam computed tomography for image-guided radiation therapy. *Int. J. Oncol. Biol. Phys.*, 53:1337–1349, 2002.

[2] Boone J M, Nelson T R, Lindfors K K, and Seibert J A. Dedicated breast CT: radiation dose and image quality evaluation. *Radiology*, 221:657–667, 2001.

[3] Siewerdsen J H and Jaffray D A. Cone-beam computed tomography with a flat-panel imager: Magnitude and effects of x-ray scatter. *Med. Phys.*, 28:220–231, 2000.

[4] Glover G H. Compton scatter effects in CT reconstructions. *Med. Phys.*, 9:860–867, 1982.

[5] Ning R, Tang X, and Conover D. X-ray scatter correction algorithm for cone beam CT imaging. *Med. Phys.*, 31:1195–1202, 2004.

[6] Hopkins F, Du Y, Lasiuk B, Abraham A, and Basu S. Analytical corrections for beam-hardening and object scatter in volumetric computed tomography systems. In *16th world conference on nondestructive testing*, Montreal, Canada, 2004.

[7] Siewerdsen J H, Daly M J, Bakhtiar B, Moseley D J, Richard S, Keller H, and Jaffray D A. A simple, direct method for x-ray scatter estimation and correction in digital radiography and cone beam CT. *Med. Phys.*, 33:187–197, 2006.

[8] Liu X, Shaw C, Altunbas M, and Wang T. A scanning sampled measurement (SSM) technique for scatter measurement and correction in cone beam breast CT (abstract). *Med. Phys.*, 32:2093, 2005.

[9] Ning R, Chen B, Yu R, Conover D, Tang X, and Nong Y. Flat panel detector-based cone-beam volume CT angiography imaging: system evaluation. *IEEE Transactions on Medical Imaging*, 19:949–963, 2000.

[10] Kwan A L C, Boone J M, and Shah N. Evaluation of x-ray scatter properties in a dedicated cone-beam breast CT scanner. *Med. Phys.*, 32:2967–2975, 2005.

[11] Johns P C and Yaffe M. Scattered radiation in fan beam imaging systems. *Med. Phys.*, 9:231–239, 1982.

[12] Boone J M and Seibert J A. Monte Carlo simulation of the scattered radiation distribution in diagnostic radiology. *Med. Phys.*, 15:713–720, 1988.

[13] Kalender W. Monte Carlo calculations of x-ray scatter data for diagnostic radiology. *Phys. Med. Biol.*, 26:835–849, 1981.

[14] Chan H P and Doi K. Physical characteristics of scattered radiation in diagnostic radiology: Monte Carlo simulation studies. *Med. Phys.*, 12:152–165, 1984.

[15] Malusek A, Sandborg M, and Carlsson G A. Simulation of scatter in cone beam CT- effect on projection image quality. *Proc. SPIE*, 5030:740–751, 2003.

[16] Reza Ay M and Zaidi H. Development and validation of MCNP4C-based Monte Carlo simulator for fan- and cone-beam x-ray CT. *Phys. Med. Biol.*, 50:4863–4885, 2005.

[17] Briesmeister J F. MCNP - a general Monte Carlo N-particle transport code version 4C. Technical Report LA-12625-M, Los Alamos Natl. Lab., 2000.

[18] Siewerdsen J H and Jaffray D A. Three-dimensional transfer characteristics of volume ct using direct and indirect flat-panel imagers. *Proc. SPIE Physics of Medical Imaging*, 5030:92–102, 2003.

[19] Colbeth R E, Boyce S J, Fong R, Gray K W, Harris R A, Job I D, Mollow I P, Nepo B, Pavkovich J M, Taie-Nobarie N, Seppi E J, Shapiro E G, Wright M D, Webb C, and Yu J M. 40 × 30 cm flat-panel imager for angiography, R&F , and cone-beam CT applications. *Proc. SPIE Physics of Medical Imaging*, 4320:94–102, 2001.

[20] Rogers D W O, Faddegon B A, Ding G X, Ma C M, Wei J, and Mackie T R. BEAM: A Monte Carlo code to simulate radiotherapy treatment units. *Med. Phys.*, 22:503–524, 1995.

[21] Walters B, Kawrakow I, and Rogers D W O. DOSXYZnrc users manual. PIRS 794revB, NRCC, 2004.

[22] Yorkston J, Antonuk L E, El-Mohri Y, Huang W, Jee K W, Sarpine V E, and Siewerdsen J H. Measurements of flare with an a-Si:H imaging array. *Med. Phys.*, 23:1076, 1996.

[23] Moy J P. Recent developments in X-ray imaging detectors. *Nucl. Instr. and Meth. A*, 442:26–37, 2000.

[24] Verhaegen F, Nahum A E, Van de Putte S, and Namito Y. Monte Carlo modeling of radiotherapy kV x-ray units. *Phys. Med. Biol.*, 44:1767–1789, 1999.

[25] Persliden J and Carlsson G A. Scatter rejection by air gaps in diagnostic radiology. calculations using Monte Carlo collision density method and consideration of molecular interference in coherent scattering. *Phys. Med. Biol.*, 42:155–175, 1997.

[26] Neitzel U. Grids or air gap for scatter reduction in digital radiography: a model calculation. *Med. Phys.*, 19:475–481, 1992.

[27] Jarry G, Graham S A, Jaffray D A, Moseley D J, and Verhaegen F. Techniques to improve the efficiency of scatter correction for kilovoltage cone beam computed tomographic (cbct) images using monte carlo simulations. *Proc. SPIE Physics of Medical Imaging*, 6142:1634–1643, 2006.

[28] Nikalson L T, Sorenson J A, and Nelson J A. Scattered radiation in chest radiography. *Med. Phys.*, 8:677–681, 1981.

[29] Siewerdsen J H and Jaffray D A. Optimization of x-ray imaging geometry with specific application to flat panel cone-beam computed tomography. *Med. Phys.*, 27:1903–1914, 2000.

[30] Jarry G, Graham S A, Moseley D J, Jaffray D A, Siewerdsen J H, and Verhaegen F. Characterization of scattered radiation in kV CBCT images using Monte Carlo simulations. *Med. Phys.*, 33:4320–4329, 2006.

CHAPTER 8
Conclusion

8.1 Summary

The development of new technologies such as intensity modulated radiation therapy (IMRT), electron modulated therapy (EMT) and Monte Carlo (MC) treatment planning leads to new requirements for treatment verification. In this thesis, we have investigated how treatment verification can be improved by acquiring portal images during electron beam treatments, by implementing a new patient dose verification method based on portal imaging and MC simulations, and by increasing the image quality of kV CBCT by correcting for scattered radiation.

In chapter 3, we described and validated the MC models of the linear accelerator and the portal imager used throughout the thesis. In chapter 4, the dosimetric characteristics of the aS500 portal imager were evaluated. It was established that this type of EPID is well suited for dosimetric verification of IMRT treatments.

In chapter 5, it was shown that portal images of adequate quality can be obtained by using the bremsstrahlung portion of an electron beam. MC simulations were used to investigate the production of bremsstrahlung photons in clinical electron beams. The image quality was characterized using signal-to-noise ratio, contrast-to-noise ratio, contrast, and MTF measurements; it was shown to be comparable to portal images acquired with photon beams. A preliminary study also showed that it is possible to predict portal images using MC simulations. The imaging technique was

applied to a head and neck patient and compared to portal images acquired with a photon beam.

In chapter 6, a new method to reconstruct the dose delivered to patients using MC simulations and portal images obtained during the treatment was described. The method was validated against MC dose recalculations of treatment plans and against film measurements. The method was found to offer the following advantages: 1) it takes into account patient inhomogeneities because it uses MC simulations, 2) it can be used as a daily dose verification tool, and 3) it includes a verification of patient movement. The new method was applied to a lung IMRT treatment for the chest of an anthropomorphic phantom. It was shown that even in such complex cases, involving inhomogeneities and modulated intensities, the dose reconstruction algorithm performs well.

In chapter 7 the scatter contribution to CBCT projection images was characterized using MC simulations. The MC simulations were also used to develop a technique to correct for scattered radiation in projection images. The scatter correction technique was found to improve the image quality mostly by reducing the cupping and streaking artifacts. Some simplifications and modifications to the MC model were suggested to render the scatter correction technique usable in a clinical setting.

8.2 Future Work

Verification of the patient set-up and of the dose delivered are essential steps of radiation therapy treatments. An adequate verification can improve drastically the quality of the treatment by ensuring that the radiation dose is delivered to the

tumor volume and that the organs at risk are spared. This thesis only considered certain aspects of treatment verification, considerable work still remains to be done. In the case of electron beam treatment verification the technique described in this thesis still needs to be implemented clinically. A large scale study of head and neck patient set-up could reveal the impact of mis-positioning for such treatment. New technologies such as the EMT will also increase the need for positioning verification and dosimetric verification.

Dosimetric treatment verification for photon beams is still in its experimental stage. Very little clinical studies have been performed to compare the planned dose to the dose actually delivered. Such studies should indicate how accurately it is possible to deliver dose and eventually offer the possibility to correlate the delivered dose to the treatment outcome.

In the area of patient positioning new modalities are being introduced such as ultrasound, MRI and CBCT. A fair amount of research is still required to improve the image quality of these modalities, to integrate them with the linear accelerator and/or to render the image usable for treatment planning. The technique described in this thesis to improve the image quality of kV CBCT still needs to be applied on patients. It would be interesting to compare it to other scatter reduction techniques in cases where the patient is shifted or when large inhomogeneities are present. The new imaging modalities will eventually allow on-line dosimetric verification taking into account positioning of the patient during the treatment as well as organ motion. It will then be possible to reconstruct the dose delivered to the patient and to re-plan the treatment taking into account the dose that was actually delivered to the patient.

This step will require further research into faster dose computational algorithms which ideally should include automatic segmentation of the organs and tumor.

Appendix A - Publisher Waivers

List of Abbreviations

2D: Two-dimensional

3D: Three-dimensional

A.U.: Arbitrary Units

AAPM: American Association of Physicists in Medicine

AP: Anterior-posterior

aSi: Amorphous silicon

CBCT: Cone beam computed tomography

CM: Component module

CNR: Contrast-to-noise ratio

CPU: Central processing unit

CSDA: Continuously slowing down approximation

CT: Computed tomography

DF: Dark field

dpi: Dots per inch

DQE: Detective quantum efficiency

EGS: Electron-Gamma-Shower

EPID: Electronic portal imaging detector

FF: Flood field

FOV: Field of view

FS: Field size

HVL: Half value layer

ICRU: International Commission on Radiation Units and Measurements

IGRT: Image guided radiation therapy

IMRT: Intensity-modulated radiation therapy

kV: Kilovoltage

Linac: Linear Accelerator

lp: Line pair

LS: Leaf speed

MC: Monte Carlo

MCDC: Monte Carlo dose calculation

MGH: Montreal General Hospital

MLC: Multileaf collimator

MOSFET: metal-oxide-semiconductor field-effect transistor

MRI: Magnetic resonance imaging

MTF: Modulated transfer function

MU: Monitor unit

MV: Megavoltage

NACP: Nordic Association of Clinical Physicists

NIST: National Institute of Standards and Technology

PDD: Percent depth dose

psf: Phase space file

QA: Quality assurance

Rp: Electron practical range

ROI: Region of interest

SDD: Source-to-detector distance

SNR: Signal-to-noise ratio

SPR: Scatter-to-primary ratio

SSD: Source-to-surface distance

TFT: Thin film transistor

TLD: Thermoluminescent dosimeter